Proceeding
Of
2nd International Conference on Computer Science and Information Technology (ICCIT 2015),

2nd International Conference on Progress in Production, Mechanical and Automobile Engineering (ICPMAE-2015)
&
2nd International Conference on Biotechnology, Civil and Chemical Engineering (ICBCCE 2015)

Date: 4th January 2015
Goa

Editor-in-Chief

Dr. Hansa Jeswani
Asso. Professor.,
Sardar Patel College of Engineering, Mumbai

Organized by:

TECHNICAL RESEARCH ORGANISATION INDIA
Website: www.troindia.in

ISBN: 978-81-930280-7-0

About Conference

Technical Research Organisation India (TROI) is pleased to organize the 2nd International Conference on Computer Science and Information Technology (ICCIT 2015), 2nd International Conference on Progress in Production, Mechanical and Automobile Engineering (ICPMAE-2015) & 2nd International Conference on Biotechnology, Civil and Chemical Engineering (ICBCCE 2015).

ICCIT & ICPMAE is a comprehensive conference covering the various topics of Engineering & Technology such as Computer Science, Mechanical and IT. The aim of the conference is to gather scholars from all over the world to present advances in the aforementioned fields and to foster an environment conducive to exchanging ideas and information. This conference will also provide a golden opportunity to develop new collaborations and meet experts on the fundamentals, applications, and products of Computer science, IT and Mechanical. We believe inclusive and wide-ranging conferences such as ICCIT can have significant impacts by bringing together experts from the different and often separated fields of Computer & IT. It creating unique opportunities for collaborations and shaping new ideas for experts and researchers. This conference provide an opportunity for delegates to exchange new ideas and application experiences, we also publish their research achievements. ICPMAE & ICBCCE shall provide a plat form to present the strong methodological approach and application focus on Mechanical, civil & chemical engineering that will concentrate on various techniques and applications. The conference cover all new theoretical and experimental findings in the fields of Electrical, Civil, Chemical and Biotechnology engineering or any closely related fields.

Topics of interest for submission include, but are not limited to:

Computer Science & Engineering
Information Technology
Electrical Engineering
Electronics Engineering
Chemical Engineering
Aeronautical Engineering
Environmental Engineering
Nano-Technology,
Genetic Engineering
Materials and Metallurgical Engineering
Soft computing
Aeronautical Engineering
Agricultural engineering
Civil engineering
Engineering Science
Network Engineering
Software Engineering
Structural Engineering
System Engineering
Telecommunication Engineering
And many more....

Organizing Committee

Editor-in-Chief:
Dr. Hansa Jeswani
Asso. Professor.,
Sardar Patel College of Engineering, Mumbai

Programme Committee Members:

Dr. Dariusz Jacek Jakóbczak
Assistant Professor , Computer Science & Management .
Technical University of Koszalin, Poland

Prof. (Dr.) Arjun P. Ghatule
Director, Sinhgad Institute of Computer Sciences (MCA),Solapur(MS)

Dr. S.P.ANANDARAJ.,
M.Tech(Hon's),Ph.D.,
Sr.Assistant Professor In Cse Dept,
Srec, Warangal

Prof O. V. Krishnaiah Chetty
Dean, Mechanical Engineering
Sri Venkateswara College of Engineering and Technology
Chittoor- Tirupati

Dr. D.J. Ravi
Professor & HOD, Department of ECE
Vidyavardhaka College of Engineering, Mysore

Prof. Roshan Lal
PEC University of Technology/Civil Engineering Department,
Chandigarh, India
rlal_pec@yahoo.co.in

Dr. Bhasker Gupta
Assistant Professor. Jaypee University of Information Technology, Himachal Pradesh

Dr. A. Lakshmi Devi,
Professor, department of electrical engineering,
SVU college of Engineering, Sri Venkateswara university, Tirupati

Prof. Shravani Badiganchala

Assistant professor, Shiridi sai institute of science and engineering

Prof. Surjan Balwinder Singh
Associate Professor in the Electrical Engineering Department,
PEC University of Technology, Chandigarh.

Dr. Shilpa Jindal ,
PEC University of Technology (Deemed University), Chandigarh
ji_shilpa@yahoo.co.in

Prof. S. V. Viraktamath
Dept. of E&CE S.D.M. College of Engg. & Technology Dhavalagiri, Dharwad

Subzar Ahmad Bhat
Assistant Professor, Gla University
Dr. G.Suresh Babu
Professor,Dept. of EEE,CBIT, Hyderabad

Prof .Ramesh
Associate Professor in Mechanical Engineering,
St.Joseph's Institute of Technology

Prof.Amit R. Wasnik
Sinhgad Institute of Technology, Pune, Maharashtra

IIT KHARAGPUR
Prof. Rajakumar R. V.
DEAN Acadedemic, rkumar @ ece.iitkgp.ernet.in
Prof. Datta D., ddatta @ ece.iitkgp.ernet.in
Prof. Pathak S S,r,ssp @ ece.iitkgp.ernet.in

XIMB,BHUBANESWAR
Prof Dr. Subhajyoti Ray.M-Stat, (ISI); Fellow, IIM(A),
Dean academic,XIMB-subhajyoti@ximb.ac.in ,
Prof.Andrew Dutta

Prof. Saveeta Mohanty

Dr. S. Peppin

Prof. Dipak Misra

Dr. W.S. William

Prof. Sunil agrawal

TABLE OF CONTENTS

Editorial

The conference is designed to stimulate the young minds including Research Scholars, Academicians, and Practitioners to contribute their ideas, thoughts and nobility in these two integrated disciplines. Even a fraction of active participation deeply influences the magnanimity of this international event. I must acknowledge your response to this conference. I ought to convey that this conference is only a little step towards knowledge, network and relationship.

The conference is first of its kind and gets granted with lot of blessings. I wish all success to the paper presenters.

I congratulate the participants for getting selected at this conference. I extend heart full thanks to members of faculty from different institutions, research scholars, delegates, TROI Family members, members of the technical and organizing committee. Above all I note the salutation towards the almighty.

Editor-in-Chief:
Dr. Hansa Jeswani
Asso. Professor.,
Sardar Patel College of Engineering, Mumbai

PRODUCTION OF BIOACTIVE COMPOUNDS USING MARINE ISOLATES IN CO-CULTURING SYSTEMS

[1]Panjwani R, [2]Deshpande A, [3]Mahajani S, [4]Joshi K
[1,2,3,4] Sinhgad College of Engineering, Pune
Email: [1]richapanjwani@gmail.com, [2]adabhishek260@gmail.com,
[3]smahajani.scoe@sinhgad.edu, [4]joshikalpana@gmail.com

Abstract— Co-culture is the simultaneous cultivation of two or more species of microorganisms in the same medium. Routine laboratory procedures practice culture of a single microorganism wherein only a fraction of the total genes are expressed. Co-cultivation of two or more different microbes tries to resemble the natural environment in which these organisms originally grow. Competition between microbes is induced deliberately and stressful conditions arise leading to enhanced production of compounds produced in pure cultures or production of novel compounds that are not detected in pure cultures. Present study deals with the production of bioactive compounds in co-culture of marine microorganisms. These compounds were purified and further screened for antimicrobial activity against multiple drug-resistant micro-organisms.

***Index Terms*—Bioactive compounds, co-culture, marine, multiple drug-resistant micro-organisms.**

I. INTRODUCTION

The marine environment covers almost 70% of the earth surface. Marine water bodies are a rich source of microorganisms which include a variety of fungus, bacteria, actinomycetes, etc. and these organisms represent a novel source of new bioactive compounds. Marine organisms are a potent source for new biologically active secondary metabolites. Marine-derived fungi and bacteria from various coasts have been isolated, characterised and exploited for the production of various drugs.

Co-culture systems have been used to study the interactions between cell populations and are fundamental to cell–cell interaction studies of any kind. A co-culture is a cell cultivation set-up, in which two or more different populations of cells are grown with some degree of contact between them. These techniques find myriad applications in biology for studying natural or synthetic interactions between cell populations. The main reason for conducting co-culture experiments and motivation for using such a set-up include: (1) studying natural interactions between populations, (2) improving cultivation success for certain populations, (3) establishing synthetic interactions between populations [4]. The importance of this study is to compare the rate of antibiotic production by the bacteria solely and when it is co-inoculated with another bacterium. Quorum sensing forms the basis for cell induced antibiotic production. Bacterial cells have the ability to show cell to cell communication in presence of another bacteria with their autoinducers. This allows the bacteria to sense a critical cell mass and in response activate or repress target genes [5].

Marine microorganisms are a major source for Marine Microbial Natural Products (MMNP) discovery [3]. Co-cultivation is also one of the techniques used for activation of the silent genes for the production of new compounds. Growing or cultivating of two or more microorganisms in the same broth is called co-cultivation, also referred to as “mixed fermentation”. The present study deals with co-cultivation of marine microbial isolates. The extraction of bioactive compounds and further screening for antimicrobial activity was attempted against multiple drug-resistant micro-organisms isolated from clinical samples resistant against commonly used antibiotics.

II. MATERIALS AND METHODS

Marine microbial strains and media

The marine microbial strains used in this study are as follows: *Aspergillus fumigatus* (NCIM902), *Bacillus pumilus* (NCIM2327), *Candida albicans* (NCIM3100) and *Rhodococcus* sp. (NCIM5452). Strains were obtained from National Collection of Industrial Microorganisms (NCIM). *Bacillus* and *Rhodococcus* strains were cultured in nutrient broth (as suggested by NCIM) at 37°C while *Aspergillus* and *Candida* strains were cultured in yeast-malt extract broth at 37°C.

Test organisms

To test the antibiotic activity, clinical cultures of drug resistant strains, Methicillin resistant *Staphylococcus aureus* (MRSA), *Pseudomonas aeroginosa* (resistant to commonly used antibiotics) and MDR *E. coli,* isolated from clinical samples were used.

Pre-tests for microbial inhibition

To test the inhibition of one organism due to the bioactive compounds produced by another, cross streak method was used. Nutrient agar plates and yeast-malt extract agar plates were prepared. On these plates, one microorganism was streaked horizontally, while the other was streaked from the edge of the plate perpendicular to the first streak.

Combinations of organisms used for co-culture:

1. *Aspergillus fumigatus – Rhodococcus* sp. on nutrient broth agar plate
2. *Bacillus pumilus - Rhodococcus* sp. on nutrient broth agar plate
3. *Aspergillus fumigatus - Candida albicans* on yeast malt extract broth agar plate

Inhibition zones were observed at the intersection of two streaks.

Co-culture

The above mentioned combinations of microorganisms were grown in a medium to find out the production of antibiotic compound. Totally, three set of cultures of each combination were maintained as follows:

A. Live cells of 1st and 2nd strains

In this, 10ml of 24 hours old broth cultures of both strains were added to the 100 ml of respective broths.

B. Live cells of 2nd strain alone (control)

In culture system B, 10ml of 24 hours old culture of 1st strain alone was inoculated.

C. Live cells of 1st strain alone (control)

In culture system C, 10ml of 24 hours old 2nd strain alone was inoculated.

All the cultures were incubated at 37°C for 5 days. After the incubation period, the cultures were centrifuged at 2500 rpm for 20 minutes. The supernatant was collected and subjected to antibacterial assay with multiple drug resistant test strains.

Screening for antibiotic activity

Antibiotic activity was assayed using a standard agar well diffusion method [2]. Nine test tubes were prepared each containing 1ml of LB. After autoclaving, the pathogenic strains were inoculated in it. Nutrient agar plates were flooded with test strains. Wells were created using a cork borer on plates and the supernatants of co-culture experiments were introduced into the wells. The plates were then incubated for 24 hours and the inhibition zones were observed.

Totally, three sets of plates were maintained for each combination. Each plate in a set was flooded with different test strains. All plates contained three wells which included two supernatants from control flasks and one supernatant from co-culture flask.

Agar Well Diffusion:

Following groups were made and each group was tested against the test organisms:

Group I: In yeast-malt extract broth

1. *Aspergillus fumigatus* (control)
2. *Candida albicans* (control)
3. *Aspergillus* + *Rhodococcus* (Co-culture supernatant)

Group II: In nutrient broth

1. *Aspergillus fumigatus* (control)
2. *Candida albicans* (control)
3. *Aspergillus* + *Rhodococcus* (Co-culture supernatant)

Group III: In nutrient broth

1. *Bacillus pumilus* (control)
2. *Rhodococcus sp.* (control)
3. *Bacillus* + *Rhodococcus* (Co-culture supernatant)

These three groups were tested on the following organisms:

1. MDR *E. coli*
2. Methicillin resistant *Staphylococcus aureus* (MRSA)
3. *Pseudomonas aeroginosa* (resistant to commonly used antibiotics)

III. RESULTS

Pre-tests for microbial inhibition- Cross streak method

The tests showed that *C. albicans* completely inhibits *A. fumigatus* (Fig. 1{a}). Cross streak analysis for *B. pumilus* – *Rhodococcus* sp. combination showed that both organisms can grow together (Fig. 1{b}) while in *A. fumigatus* – *Rhodococcus* sp. combination, *Rhodococcus* sp. strongly (but not completely) inhibits *A. fumigatus* (Fig. 1{c}). Hence, the latter two combinations were selected for co-culture studies.

Screening for antibiotic activity

Antibiotic activity was studied using agar well diffusion method. In all cases, supernatants sfrom co-culture showed higher antibiotic activity than those from individual controls which proved that co culturing would help bring out higher antibiotic activity (Fig. 2). Supernatant from *A. fumigatus* – *Rhodococcus* sp. co-culture maximally inhibited MDR *E.coli* while supernatant from *B. pumilus* – *Rhodococcus* sp. co-culture maximally inhibited MDR *E.coli* and methicillin resistant *Staphylococcus aureus* (Fig. 3).

IV. CONCLUSION

Co-cultivation is one of the techniques used for activation of the silent genes for the production of new compounds [1].

An effort was made to co-cultivate marine derived fungi and bacteria and isolation of crude bioactive compounds capable of acting on clinically resistant strains of infectious organisms.

Co-cultivation (also called mixed fermentation) of two or more different microorganisms tries to mimic the ecological situation where microorganisms always co-exist within complex microbial communities. The competition or antagonism experienced during co-cultivation is shown to lead to an enhanced production of constitutively present compounds and/or to an accumulation of cryptic compounds.

The present study provides a platform for further studies of interaction between marine bacteria and the exploration of their antibiotic property towards MDR bacteria.

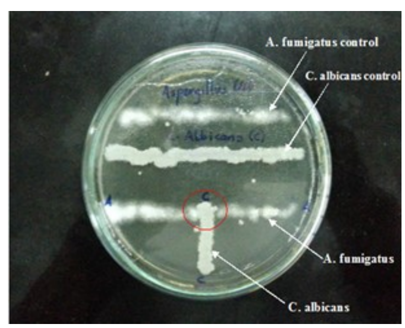

(a) *A.fumigatus* - *C.albicans*

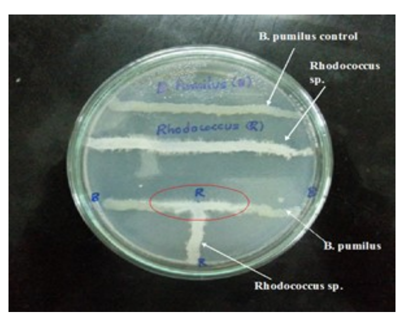

(b) *B.pumilus* – *Rhodococcus* sp.

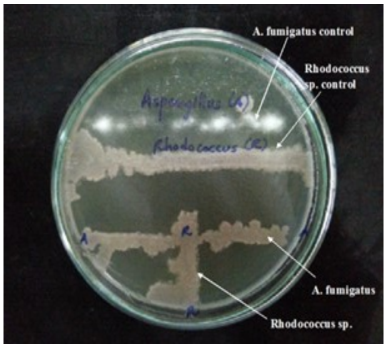

(c) *A.fumigatus – Rhodococcus* sp.

Fig. 1: Inhibition tests by cross streak method

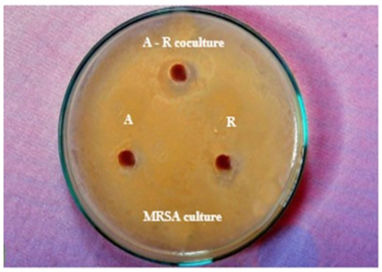

(a) A= 9 mm, R=8 mm, A-R co-culture= 14 mm

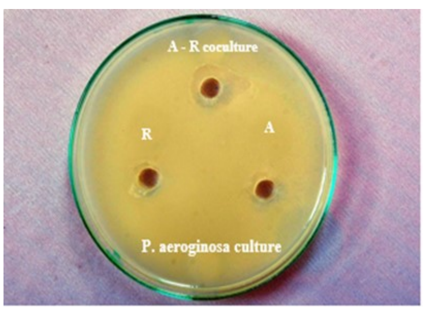

(b) A= 10 mm, R=9 mm, A-R co-culture= 14 mm

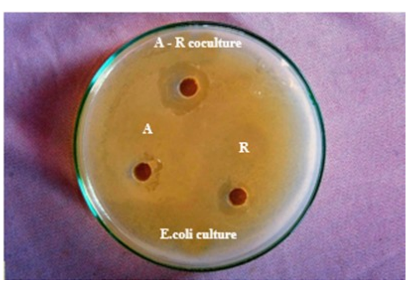

(c) A= 8 mm, R=13 mm, A-R co-culture= 20 mm

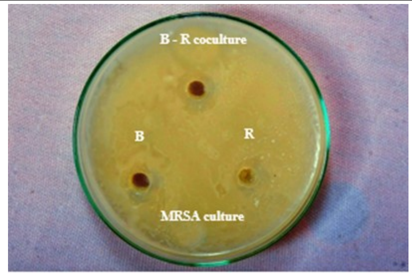

(d) B= 11 mm, R=8 mm, B-R co-culture= 15 mm

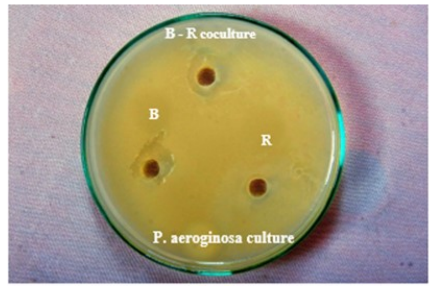

(e) B= 12 mm, R=8 mm, B-R co-culture= 14 mm

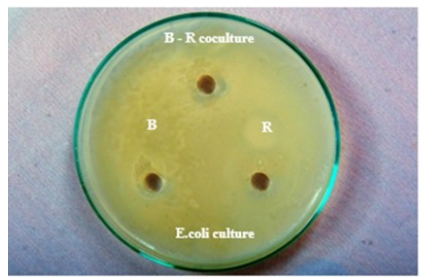

(f) B= 10 mm, R=0 mm, B-R co-culture= 15 mm

Fig. 2: Screening for antimicrobial activity using agar well diffusion method and the inhibition diameters (A- *A.fumigatus*, B- *B.pumilus,* R- *Rhodococcus* sp.)

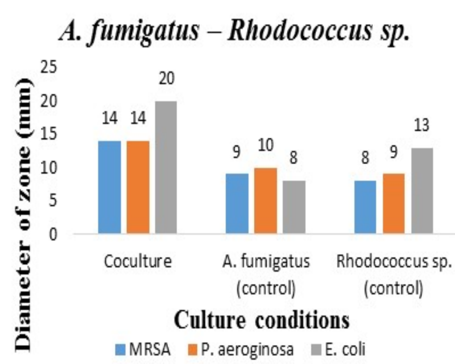

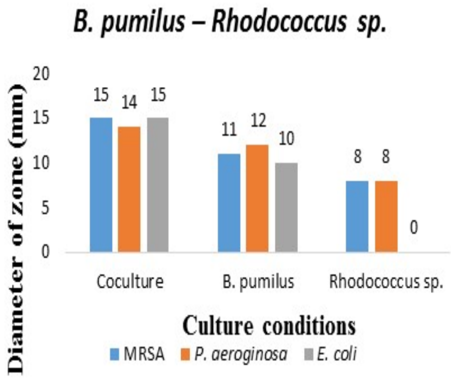

Fig. 3: Effect of culture conditions on production of antibiotic activity and tested against multiple drug resistant organisms.

REFERENCES:

[1] Andreas Marmann, Amal H. Aly, Wenhan Lin, Bingui Wang and Peter Proksch, "Co-Cultivation—A Powerful Emerging Tool for Enhancing the Chemical Diversity of Microorganisms", Mar. Drugs 2014, 12, 1043-1065.

[2] Cleidson Valgas, Simone Machado de Souza, Elza F A Smânia, Artur Smânia Jr, "Screening methods to determine antibacterial activity of natural products", Brazilian Journal of Microbiology, 2007, 38:369-380.

[3] Delbarre-Ladrat C, Sinquin C, Lebellenger L, Zykwinska A, Colliec-Jouault S, "Exopolysaccharides produced by marine bacteria and their applications as glycosaminoglycan-like molecules", Frontiers in Chemistry 2014, 2.

[4] Rateb ME, Hallyburton I, Houssen W, Bull A, Goodfellow M, Santhanam R, "Induction of diverse secondary metabolites in *Aspergillus fumigatus* by microbial co-culture", RSC Adv 2013, 3: 14444-50.

[5] Vasil ML, "NA Microarrays in Analysis of Quorum sensing*:* Strengths and Limitations", J Bacteriol, 2003, 185:2061–5

OPTIMIZATION OF INITIAL PH AND INITIAL GLUCOSE CONCENTRATION FOR MAXIMUM ETHANOL PRODUCTION WITH RESPECT TO DIFFERENT FERMENTATION KINETIC PARAMETERS BY USING *S.CEREVISAE* AND CHEMICALLY DEFINED MEDIUM.

[1]Ram Chavan, [2]Kunjan Saxena, [3]Manoj Kumar, [4]Sharad Gangawane
BITS Pilani KK Birla Goa campus, LPU Punjab, LPU Punjab, RS college, Latur (MH)
Email:[1]rams.ren22@gmail.com,[2]kunjan.16374@gmail.com,[3]manoj.kumar872@gmail.com,[4]sharadbiotech1986@rediffmail.com

Abstract—**This study presents the work regarding optimization of initial pH and initial Glucose concentration (% W/V) for maximum Ethanol production with respect to different fermentation kinetic parameters by using S.cerevisae and chemically defined medium. Ethanol is growth associated by-product synthesized by S.cerevisae and its yield (g/g) is very sensitive to the changes in the initial pH and initial Glucose concentration (g/L).Hence batch experiments were designed to optimize initial pH and initial Glucose concentration mainly with respect to maximum Ethanol yield (g/g), maximum glucose utilization rate (%) and specific growth rate (hr^{-1}).Other kinetic parameters like Biomass productivity (g/L-hr),Biomass yield (g/g),Ethanol productivity (g/L-hr) and fermentation efficiency (%) are also studied. Random experiments were designed to optimize one parameter at a time with different values. The initial pH values selected were 4.0,4.5,4.75 and 5.0.The initial Glucose concentration (% W/V) selected were 5,10,15 and 20.The optimum pH for maximum ethanol yield (0.453g/g), fermentation efficiency (88.63 %) and maximum ethanol production(39.73 g) was found to be 4.5 and it is used for the optimization of initial glucose concentration in later studies. The optimum initial glucose conc.(% (W/V)) for maximum ethanol yield (0.487g/g), fermentation efficiency (43.42 %) and maximum ethanol production(39.73 g) was found to be 10 % (W/V) .Glucose concentration is monitored with DNS assay, yeast biomass was analysed by absorbance at 525 nm and ethanol production is monitored by alcoholmeter after applying temperature correction factors.**

***Index Terms*—S.*cerevisae*, Ethanol, yield, alcoholmeter and kinetic parameters.**

INTRODUCTION

Bio-ethanol is an eco-friendly fuel that can be used in unmodified petrol engines. Combustion of ethanol results in relatively low emission of volatile organic compounds, carbon monoxide and nitrogen oxides. The emission and toxicity of ethanol are lower than those of fossil fuels such as petroleum, diesel etc. *Saccharomyces cerevisiae* is the cheapest strain used for bio-ethanol production from sugar molasses. *S.cerevisae* is capable of very rapid rates of ethanol production under optimal conditions.[1] The largest single use of ethanol is as a motor fuel and fuel additive.[2]

S.cerevisae is highly sensitive to initial pH and initial sugar concentration. At higher pH and sugar concentration it favours acid production and decrease in ethanol production respectively.[1] Ethanol production by *S.cerevisae* is influenced by various factors like initial pH, aeration rate, and temperature and sugar concentration. [3] The use of bioethanol as gasoline oxygenate is beneficial in terms of higher oxygen content, octane number and reduction of CO emission.[4] Fed batch system for fermentation has advantages over batch processes like higher productivity, higher dissolved oxygen in the medium, decreased fermentation time and reduced toxic effects of the medium components, which are present at high concentrations.[5] Wild type *S. cerevisiae* has limitation being unable to ferment pentoses and hard efforts have been made to design a suitable engineered *S. Cerevisiae.*[6]

Ethanol production by *S.cerevisae* is very sensitive to initial pH and sugar concentration. This research aims at finding optimum pH and sugar concentration with respect to high ethanol yield, fermentation efficiency, sugar utilization rate, biomass yield and productivity etc.

MATERIALS AND METHODS

Revival of dry Baker's yeast powder:

0.5 % (W/V) of dry Baker's yeast powder is suspended in 50 ml of sterile distilled water in 100 ml sterile conical flasks and kept in orbital shaker incubator at 30°C and at 150 rpm for 15 minutes.

Maintenance of Baker's yeast culture:

1 ml of revived yeast culture is transferred to sterile YEPD broth(yeastextract-10g/L,Peptone-20g/L,Glucose-100g/L,pH-4.5) and kept for incubation for 3 days. After sufficient growth, the broths were preserved in refrigerator for further use. One loop full culture is streaked on YEPD agar slants and incubated at 30 °C for 3 days. After sufficient growth, the broths were preserved in refrigerator for further use. Aseptic conditions were maintained.

Determination of Glucose Concentration:

Glucose concentration is determined by DNS assay. Glucose standard stock (1 g/L) is prepared in distilled water and is used to prepare glucose solutions with different concentrations .Optical density is determined by using Spectrophotometer Elico SL-159 adjusted at 550 nm. Standard graph is obtained by plotting Concentration of Glucose (g/L) on X axis and corresponding optical density at 550 nm on Y axis. The Glucose concentration of suitably diluted fermented broth samples was estimated by using this curve. 1 ml of previously centrifuged (without Biomass) fermented broth sample is suitably diluted to obtain OD within calibration of standard glucose curve.3 ml of this diluted broth sample is mixed with 3 ml of DNS reagent (Dinitrosalicyli acid-10 g,Phenol-2 ml,Sodium sulfite-0.5 g and Sodium hydroxide (0.4 M)-10 ml,make up the volume to 1000 ml with distilled water.) and heated in boiling water bath for 15 minutes till red brick colour developed.1 ml of Rochelle salt was added and allowed to cool. OD is recorded at 550 nm. The residual sugar concentration is then determined by standard glucose curve .Distilled water and DNS is taken as blank. [7]

Determination of Biomass Concentration:

50 ml of fermented broth samples were periodically and aseptically removed. The fermented broth sample is centrifuged at 7000 rpm for 10 minutes . The pellet is separated from supernatant and dried in incubator till constant weight is obtained. The supernatant is stored and analyzed for determination of sugar concentration and ethanol production. The dry yeast biomass weight is then diluted to with distilled water and OD is recorded at 525 nm. By using standard yeast dry weight graph, actual biomass concentration was determined and is then expressed in g/L. [7]

Determination of Ethanol Concentrations:

Approximately 40 ml of fermented broth is centrifuged at 7000 rpm and supernatant is taken in 50 ml measuring cylinder and the room temperature is noted down. The Alcoholmeter was allowed to dip freely without touching the inner walls of measuring cylinder. The readings on Alcoholmeter were noted down and the correction factor was applied to measure % (V/V) alcohol content of broth. The corrected % (V/V) alcohol content value is then multiplied with density of ethanol (at temperature at which the readings were taken) to give % (W/V) of ethanol. This value is then expressed in terms of ethanol concentration (g/L).Ethanol content of final samples was confirmed by distillation at 76^0C estimated by using alcoholmeter.

Ethanol is estimated by Gay Lussac Alcoholmeter. [7]

Determination of fermentation kinetic parameters:
The values of fermentation kinetic parameters can be determined by using following formulas or Method,
Biomass productivity (g/L-hr**):** Slope of the graph obtained by plotting Biomass concentration (g/L) against time (hr).

Biomass yield (g/g) = Biomass dry weight/Mass of Glucose utilized

Determination specific growth rate μ (hr^{-1}): Slope of curve obtained by plotting lnX (g/L) against time (hr).

Determination of Ethanol productivity (g/L-hr):
Ethanol productivity (g/L-hr): Slope of the graph obtained by plotting Ethanol concentration
(g/L) against time (hr).

Ethanol yield (g/g): Weight of ethanol produced/ Mass of Glucose utilized.

% sugar Conversion: [(Initial sugar Conc. – Final sugar Conc.) / Initial Sugar Conc.] * 100.

Sugar Utilization rate (g/hr): Slope of graph obtained by plotting sugar utilized (g) against time (hr).

Fermentation Efficiency (%): (Ethanol yield/Max. possible true yield for Ethanol) * 100.

Maximum Biomass Conc. (g/L**):** Highest value of Biomass Conc. (g/L).

Maximum Ethanol Conc. (g/L): Highest value of Ethanol Conc. (g/L).

Optimization of initial pH value:

Initial pH optimization is carried out by using defined medium-Normal strength working nutrient medium with composition ($MgCL_2.6H_2O$- 0.52 g/L, $(NH4)_2SO_4$- 12.0 g/L, $H3PO_4$ (85%)-1.6 mL/L,KCl-0.12 g/L,$CaCl_2.2H_2O$-0.2 g/L, NaCl-0.06 g/L,$MnSO_4.H_2O$-0.024 g/L,$CaSO_4.5H_2O$-0.0005 g/L,H_3BO_3-0.0005g/L,$Na_2MoO_4.2H_2O$-0.002g/L,NiCl-0.0025mg/L,ZnSO4.$7H_2O$-0.012g/L,Co$SO_4.7H_2O$-0.0023mg/L,KI-0.0001g/L,$FeSO_4$(N$H4)_2SO_4.6H_2O$-0.035g/L,Myo-Inositol-0.125 g/L,Pyridoxine-HCL (Vit- B6)-0.00625 g/L,Ca-n-Pantothenate-0.00625 g/L, Thiamine-HCL (Vitamin B1)-0.005 g/L, Nicotinic Acid-0.005 g/L,D-Biotin (Vitamin H0-0.000125 g/L,EDTA- 0.1 g/L,Glucose-50 g/L).2 L of Normal strength working nutrient medium is prepared out of which 400 ml is distributed in 4 separate 500 ml sterile flaks and pH is adjusted accordingly (pH-4.0,4.5,4.75,5.0) and were labelled carefully. The media were autoclaved at 15 psi for 15 min and allowed to cool at room temperature. Meanwhile the preserved Baker's yeast culture flask was removed and kept in room temperature.20 ml inoculums from this is transferred aseptically to each of above flasks. The flasks were incubated at 30°C in an orbital shaker incubator for 72 hr. The samples were aseptically removed from the fermentation flasks and analyzed for yeast biomass dry weight (g/L), Glucose concentration and for estimation of Ethanol produced (g/L).The initial pH value which gives better ethanol production is selected for further experimentation.

Optimization of Sugar Concentration:

Sugar concentration optimization is carried out by using defined medium-Normal strength Working nutrient medium at pH 4.5 and different sugar concentrations.2 L of Normal strength working nutrient medium is prepared and pH was adjusted to 4.5, out of which 400 ml is distributed in 4 separate 500 ml sterile flaks and Sugar conc. is adjusted accordingly (sugar concentrations % (W/V):5,10,15,20) and were labelled carefully. The media were autoclaved at 15 psi for 15 min and allowed to cool at room temperature. Meanwhile the preserved Baker's yeast flask was removed and kept in room temperature. 20 ml (inoculum) from this is transferred aseptically to each of above flasks. The flasks were incubated at 30°C in an orbital shaker incubator for 72 hr. The samples were aseptically removed from the fermentation flasks and analyzed for yeast biomass dry weight (g/L), Glucose concentration and for estimation of Ethanol produced (g/L).The initial sugar concentration value which gives better ethanol production is selected for further experimentation.

OBSERVATIONS

Observations For initial pH:

Table 1:
Biomass concentration (g/L) against time (hr) at different initial pH values. [Temperature 30°C, fermentation time 72 hr, Glucose Concentration 10% (W/V)].

Time (hr)	pH-4.0	pH-4.5	pH-4.75	pH- 5.0
0	0.4	0.4	0.4	0.4
6	0.6	0.8	0.44	0.62
24	2.6	0.9	0.84	2.04
30	4	4.6	1.04	3.8
48	5.8	7	3.8	5
54	8.6	9.8	5.98	5.8
72	10.02	11	10.2	8.2

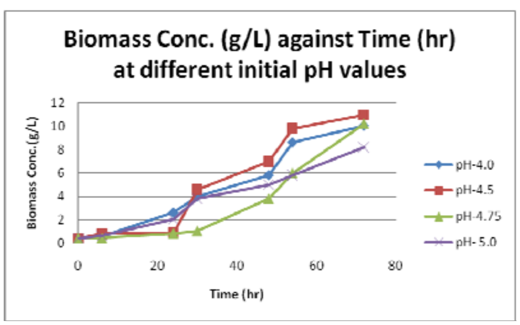

Fig.1 Biomass concentration (g/L) against time (hr) at different initial pH values.

Table 2
Residual Glucose concentration present in fermentation broth (g/L) against time (hr) at different initial pH values. [Temperature 30°C, fermentation time 72 hr, Glucose Concentration 10% (W/V)].

Time (hr)	pH-4.0	pH-4.5	pH-4.75	pH- 5.0
0	100	100	100	100
6	95	89	93	97
24	72	65	76	79
30	65	59	69	73
48	51	30	31	52
54	45	23	22	51
72	20	13	15	32

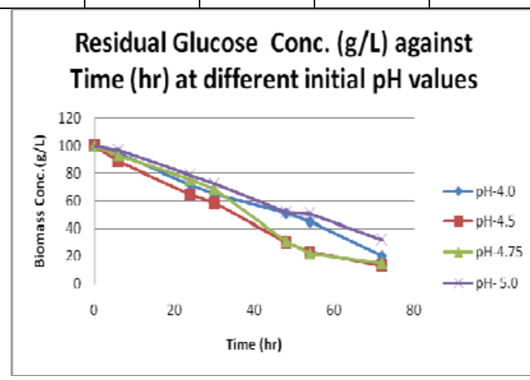

Fig.2 Residual Glucose concentration present in fermentation broth (g/L) against time (hr) at different initial pH values.

Table 3. Ethanol produced (g/L) against time (hr) at different initial pH values. [Temperature 30°C, fermentation time 72 hr, Glucose Concentration 10% (W/V)].

Time (hr)	pH-4.0	pH-4.5	pH-4.75	pH- 5.0
0	0	0	0	0
6	0	0	0	0
24	0	0	0	0
30	0	19.736	0	0
48	15.789	27.631	22.894	19.736
54	23.684	35.525	27.631	23.684
72	27.631	39.473	35.525	27.631

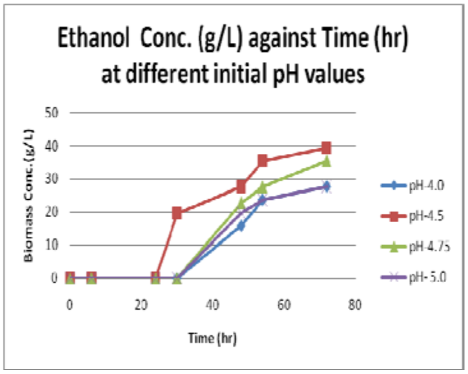

Fig.3 Ethanol produced (g/L) against time (hr) at different initial pH values.

Observations For initial Glucose conc.:

Table 4.

Biomass concentration (g/L) against time (hr) at different initial Glucose concentration (%W/V). [Temperature 30°C, fermentation time 72 hr, pH 4.5]

Time (hr)	Glucose 5%	Glucose 10 %	Glucose 15 %	Glucose 20 %
0	0.4	0.4	0.4	0.4
6	0.6	0.9	0.44	0.67
24	2.8	2.5	2.73	1.7
30	3	3.9	2.98	2.2
48	4.5	5.2	3.97	3.9
54	5.2	5.9	4.5	4.2
72	5.8	11.5	8.5	4.9

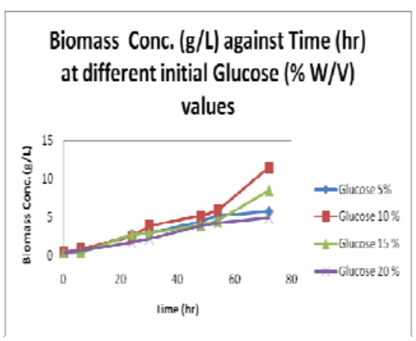

Fig.4 Biomass concentration (g/L) against time (hr) at different initial Glucose concentration(%W/V).

Table 5. Residual Glucose concentration present in fermentation broth (g/L) against time (hr) at different initial Glucose concentration. [Temperature 30°C, fermentation time 72 hr, pH 4.5].

Time (hr)	Glucose 5%	Glucose 10 %	Glucose 15 %	Glucose 20 %
0	50	100	150	200
6	48	85	142.5	196
24	40.5	63	130.5	178
30	34	55	91.5	154
48	22	31	70.5	126
54	14	22	79.5	118
72	7	11	61.5	110

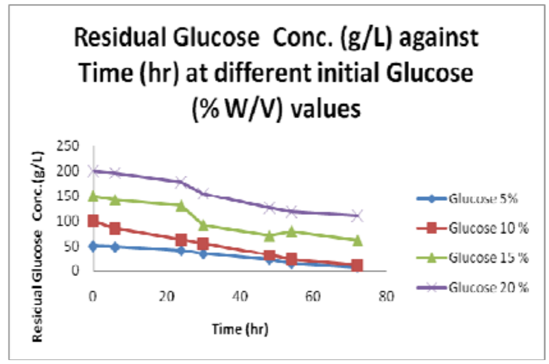

Fig. 5 .Residual Glucose concentration present in fermentation broth (g/L) against time (hr) at different initial sugar concentration.

Table 6.Ethanol produced (g/L) against time (hr) at different initial Glucose concentration. [Temperature 30°C, fermentation time 72 hr, pH 4.5].

Time (hr)	Glucose 5%	Glucose 10 %	Glucose 15 %	Glucose 20 %
0	0	0	0	0
6	0	0	0	0
24	0	0	0	0
30	0	23.648	0	0
48	0	27.631	0	0
54	0	35.525	27.631	23.648
72	15.789	43.42	35.525	31.578

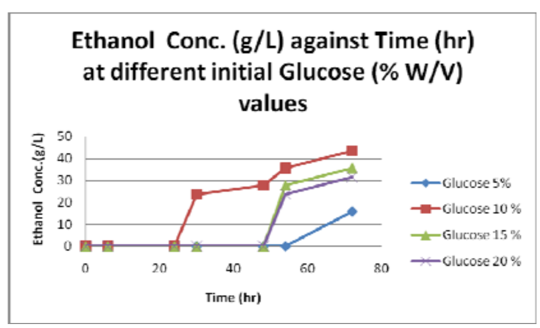

Fig.6. Ethanol produced (g/L) against time (hr) at different initial Glucose concentration.

RESULTS AND DISCUSSION:

Table 7. comparison of different kinetic parameters at different initial pH values Glucose conc.-100g/L,Temp.-30 ^{0}C, at different initial pH values):

Sr. No.	Parameter	pH-4.0	pH-4.5	pH-4.75	pH-5.0
1	Biomass Productivity (g/L-hr)	0.141	0.163	0.13	0.108
2	Biomass yield (g/g)	0.125	0.126	0.12	0.12
3	Specific growth Rate (hr^{-1})	0.046	0.048	0.049	0.042
4	Ethanol productivity (g/L-hr)	0.435	0.632	0.555	0.449
5	Ethanol yield (g/g)	0.345	0.453	0.417	0.406
6	Maximum Ethanol Conc. (g/L)	27.631	39.473	35.525	27.631
7	% Glucose utilized	80	87	85	68
8	Glucose Utilization rate (g/hr)	1.077	1.267	1.31	0.966
9	% Fermentation Efficiency	67.5	88.63	81.6	79.49
10	Maximum Biomass Conc. (g/L)	10.02	11	10.2	8.2

Maximum Biomass productivity is observed at initial pH of 4.5 which corresponds to 0.163 g/L-hr. Maximum Biomass yield is observed at initial pH of 4.5 which corresponds to 0.126 g/g. Maximum Specific growth rate is observed at initial pH of 4.75 which corresponds to 0.049 hr^{-1}.Maximum Ethanol productivity is observed at initial pH of 4.5 which corresponds to 0.632 g/L-hr. Maximum Ethanol yield is observed at initial pH of 4.5 which corresponds to 0.453 g/g. Maximum Ethanol Conc. is observed at initial pH of 4.5 which corresponds to 39.473 g/L. Maximum % Glucose utilization is observed at initial pH of 4.5 which corresponds to 87 %. Maximum Glucose utilization rate is observed at initial pH of 4.5 which corresponds to 1.267 g/hr. Maximum fermentation efficiency is observed at initial pH of 4.5 which correspond to 88.63 %. Maximum Biomass Conc. is observed at initial pH of 4.5 which corresponds to 11 g/L.

Table 8 Comparison of different kinetic parameters at different initial Glucose concentration:

Sr.No.	Parameter	Glucose 5%	Glucose 10 %	Glucose 15 %	Glucose 20 %
1	Biomass Productivity (g/L-hr)	0.08	0.138	0.101	0.067
2	Biomass yield (g/g)	0.135	0.129	0.096	0.054
3	Specific growth Rate (hr^{-1})	0.037	0.042	0.042	0.035
4	Ethanol productivity (g/L-hr)	0.148	0.666	0.473	0.416
5	Ethanol yield (g/g)	0.367	0.487	0.401	0.35
6	Maximum Ethanol Conc. (g/L)	15.789	43.42	35.525	31.578
7	% Glucose utilized	86	89	59	45
8	Glucose Utilization rate (g/hr)	0.637	1.252	1.326	1.407
9	% Fermentation Efficiency	71.8	95.3	78.47	68.49
10	Maximum Biomass Conc. (g/L)	5.8	11.5	8.5	4.9

Maximum Biomass productivity is observed at initial Glucose Conc. Of 10 % W/V which corresponds to 0.138 g/L-hr. Maximum Biomass yield is observed at initial Glucose Conc. Of 10 % W/V which corresponds to 0.129 g/g. Maximum Specific growth rate is observed at initial Glucose Conc. Of 10 % and 15 % W/V which corresponds to 0.042 hr^{-1}.Maximum Ethanol productivity is observed at initial Glucose Conc. Of 10 % W/V which corresponds to 0.666 g/L-hr. Maximum Ethanol yield is observed at initial Glucose Conc. Of 10 % W/V which corresponds to 0.487 g/g. Maximum Ethanol Conc. is observed at initial Glucose Conc. Of 10 % W/V which corresponds to 43.42 g/L. Maximum % Glucose utilization is observed at initial Glucose Conc. Of 10 % W/V which corresponds to 89 %. Maximum Glucose utilization rate is observed at initial Glucose Conc. Of 20 % W/V which corresponds to 1.407 g/hr. Maximum fermentation efficiency is observed at initial

Glucose Conc. Of 10 % W/V which correspond to 95.3 %.Maximum Biomass Conc. is observed at initial Glucose Conc. Of 10 % W/V which corresponds to 11.5 g/L.

CONCLUSION

The fermentation kinetic parameters are very sensitive to initial pH and Sugar concentration. We need to select the experimental conditions depending on the product we are interested in. No single experimental condition is ideal to get all the kinetic parameters at optimum value.

REFERENCES

[1] Arifa T., Madiha A. & Tasnim F.," Effect of cultural conditions on ethanol production by locally isolated *saccharomyces cerevisae* BIO-07," J App Pharm,Vol 3,(2),pp 72-78 ,2010.

[2] Janani K., Ketzi M., Megavathi S., Dr.Vinothkumar D., Dr. Ramesh Babu N.G.," I J of Inno. Res. in Sci., J. Engg. and Tech.," Vol. 2, Issue 12, December 2013.

[3] Yan L.,Wei Z.,Chunjie l.,Kei S.,Shuzo T.,Hainan K.," Factors affecting ethanol fermentation using *Saccharomyces cerevisiae* hBY4742," Biomass and Bioenergy,vol xxx ,1,7,September 2012.

[4] Farah A., Ahmad J., Mohd K. and Maizirwan M., Study of growth kinetic and modeling of ethanol production by *Saccharomyces cerevisae"* African Journal of Biotechnology Vol. 16(81), pp. 18842-18846, 16 December, 2011.

[5] Zarifa R., Dr. Babar S., Md. Enayetul, Akbor Md. A.," Process Optimization for Batch Culture of *Saccharomyces cerevisiae*," Sch. Acad. J. Biosci., 1(7):363-373,2013.

[6] Udhayaraja P. and Narayanan S.," Optimization for production of bioethanol using sorghum stovar by *Saccharomyces cerevisiae,"* Int. J. of Res. in Pure and App. Microbiology,vol 2,4,pp 64-67,October 2012.

[7] Chavan Ram.,Saxena K.,Manoj K.,"Comparison of biomass and ethanol production kinetics of commercial baker's yeast (*S.cerevisae*) in a chemically defined medium against cane molasses,waste banana pulp and waste potato flour," International J. of App. Engg. Research,vol 8,15, pp 1853 – 1860,2013.

WIND INDUCED INTERFERENCE EFFECTS ON NATURAL DRAUGHT COOLING TOWER

[1]Chiranjit Mishra, [2]A. Ranjith, [3]Sanjith J, [4]Dr. B. M. Kiran
[1,2,3]Student, Department of Civil Engineering, Adichunchanagiri Institute of Technology, Chikmagalur
[4]Assistant Professor, Department of Civil Engineering, Adichunchanagiri Institute of Technology, Chikmagalur

Abstract— **The wind load is always the dominant load in the design of the cooling tower due to its large size, complex geometry and thin wall. In a series of wind tunnel tests, the wind-induced stresses in cooling towers situated in an arrangement of typical power plant buildings, are investigated and compared to the stresses in an isolated tower. Interference factors are developed to quantify the stress increase due to the group effect. The design wind pressure at various level of tower measured from gust factor method and peak wind method. The variation of the flow-induced forces produced on each tower by the other one is referred to as interference. Using the registered pressures, numerical linear and nonlinear analyses were performed to calculate the structural responses of the isolated and grouped towers. The net coefficient of pressure distribution was plotted for various angle of wind incidence. From the study, it was found that Meridional stress is 8.86% more and circumferential stress is about 9.43% more in present study compared to existing NDCT model. Also, the highest net pressure coefficient is obtained as 1.436, when the wind incidence angle is about 0°. The value approaches to a minimum value of about -0.934, when the wind incidence angle is about 330° and occurring at about 105° angle. The results of present study are in close agreement with the existing structure. Thus, the numerical model is validated.**

Index Terms— Wind interference, Aero-elastic wind tunnel tests, Stress responses, cooling tower.

I. INTRODUCTION

Natural Draught Cooling Towers are Hyperbolic Reinforced Concrete (RC) shell structures used in thermal and nuclear power plants as cooling devices. In the last decade, Natural Draught Cooling Towers became even more inevitable means for the economic generation of electricity under environmental aspects.

The hyperboloid of revolution can be generated by rotating a hyperbola about its directrix. Shells of this type are built throughout the world as cooling towers to lower the temperature of coolants (water) used in electricity generating plants and chemical plants. This type of shell has proven to be efficient for use in Reinforced Concrete Natural Draught Cooling Towers for the conservation and reuse of the coolant.

In the present study, the sizing of cooling tower is taken based on the thermal design report and capacity of cooling tower. In this study 500MW capacity of Natural Draught Cooling Tower for Thermal Power Plant is taken. The tower is analyzed using the commercially available Staad Pro v8i software.

The wind load is calculated as per IS 11504 and IS 875 for the analysis of isolated case of cooling tower. For Interference case of cooling tower based on the wind tunnel study report pressure co-efficient is considered and it is multiplied with the dynamic wind pressure and corresponding surface area. Modal analysis is done for dynamic seismic load as per IS 1893:2002. In this study the cooling tower is analyzed for both wind and seismic loads.

DESCRIPTION OF THE COOLING TOWER

General Arrangement

Cooling tower consists of RCC shell, which is hyperbolic, shaped except for the portion at bottom, which is conical. The shell is supported on 44 pairs of diagonal columns in RCC, which are raked tangential to the Meridional profile of the shell at its bottom; the open system of columns also provides the air inlet opening. The diagonal columns rest on RCC pedestals, which are in the same inclined plane. The RCC pedestals are an integral part of the pond wall in RCC, which retains the re-cooled water. Pond wall spanning between the pedestals will be considered. At bottom, a ring shaped horizontal RCC ring foundation below the pond wall and pedestal is provided. The soil bearing capacity for ring foundation is considered 50t/m2 at depth of 5.0m from FGL.

RCC platform 1.2m wide all around the tower at top shall be provided, which is accessed by two M.S. cage ladders. These ladders spring from the top of an RCC staircase. The ladders are on outside up to throat level and then on the inside up to the top, with inter connection through a landing platform and access door at the throat level. The RCC staircase leads from ground level up to the level of water distribution system. Internal walkways in RCC are provided on periphery of tower cantilevering from the shell at the hot water distribution level and on the hot water distribution duct inside the tower.

Functional Requirements of the Cooling Tower

Duty and Capacity

a. Quantity of circulating water per tower : 60000 cum/hr
b. Type of tower : Natural draught (hyperbolic)
c. Period of operation : 24 hrs continuous
d. Hot water inlet temperature : 43.0 degree C
e. Re-cooled water outlet temperature : 32.5 degree C
f. Design relative humidity : 50%
g. Design ambient wet bulb temperature : 27 degree C
h. Design wind speed : 39 m/sec

Important Dimensions

a) **Elevations (in meters)**

i) Pond sill +0.00
ii) Ground level -0.30
iii) Basin floor at periphery -2.30
iv) Working level of water -0.30
v) Top of the tower +160.00
vi) Throat of the tower +129.00
vii) Bottom of ring beam +8.00
viii) Top of fill +14.00
ix) Bottom of fill +8.00
x) Bottom of drift eliminators +15.55

Table 5.1 Elevation details of Natural Draught Cooling Tower

b) Internal Diameters of the Tower (in metres)

i) Diameter at sill level +122.00
ii) Diameter at throat level +67.10
iii) Diameter at top of tower +68.50

Accordingly, the profiles of the towers are as shown in fig. 1 all the details i.e. height of tower above ground level, height from throat to top of the tower, height of air vent, Diameter at sill level, Diameter at throat level, Diameter at top of tower indicated in the following fig.1, are in meters.

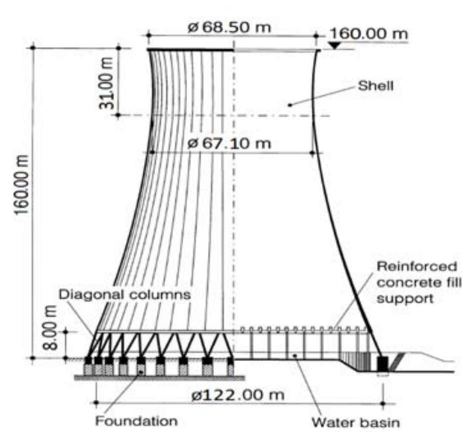

Fig: 1. Profile of the cooling tower

In this case, wind load is calculated by the following two methods and the results are tabulated in table 1.

a. Gust factor method
b. Peak wind method

Table 1 Design wind pressure at various levels of cooling tower

	Peak Wind Method				Gust Factor Method			
Level	K2 Table 2	Vz	PzN/m^2	Pz KN/m^2	K2 Table33	Vz	Pz $=0.6Vz^2$	Pz G*Coeff.
8.836	0.9300	52.452	2360.54	2.361	0.6700	37.7	2140.0	2.140
10	0.93	52.452	2360.54	2.361	0.67	37.7	2140.0	2.140
11.589	0.9427	53.168	2425.50	2.425	0.6859	38.6	2242.7	2.243
15	0.97	54.708	2567.96	2.568	0.72	40.6	2471.3	2.471
15.575	0.9734	54.902	2586.25	2.586	0.7234	40.8	2495.1	2.495
19.715	0.9983	56.303	2719.92	2.720	0.7483	42.2	2669.3	2.669
20	1	56.4	2729.26	2.729	0.75	42.3	2681.6	2.682
23.858	1.0154	57.270	2814.14	2.814	0.7654	43.1	2793.0	2.793
28.004	1.0320	58.2057	2906.82	2.907	0.7820	44.1	2915.4	2.915
30	1.04	58.656	2951.97	2.952	0.79	44.5	2975.2	2.975
32.154	1.0465	59.0204	2988.77	2.989	0.7965	44.9	3024.1	3.024
36.308	1.0589	59.7233	3060.37	3.060	0.8089	45.6	3119.5	3.120
40.4658	1.0714	60.4268	3132.90	3.133	0.8214	46.3	3216.4	3.216
44.6285	1.0839	61.1311	3206.36	3.206	0.8339	47.0	3315.0	3.315
48.7962	1.0964	61.8363	3280.76	3.281	0.8464	47.7	3415.1	3.415
50	1.1	62.04	3302.41	3.302	0.85	47.9	3444.3	3.444
52.9693	1.1042	62.2745	3327.42	3.327	0.8542	48.1	3478.1	3.478
57.1484	1.1100	62.6044	3362.77	3.363	0.8600	48.5	3525.9	3.526
61.3338	1.1159	62.9349	3398.37	3.398	0.8659	48.8	3574.1	3.574
65.5262	1.1217	63.2660	3434.21	3.434	0.8717	49.1	3622.8	3.623
69.7261	1.1276	63.5976	3470.31	3.470	0.8776	49.4	3671.8	3.672
73.9341	1.1335	63.9298	3506.67	3.507	0.8835	49.8	3721.3	3.721
78.1507	1.1394	64.2628	3543.29	3.543	0.8894	50.1	3771.2	3.771
82.3765	1.1453	64.5965	3580.18	3.580	0.8953	50.4	3821.5	3.822
86.6120	1.1513	64.9309	3617.35	3.617	0.9013	50.8	3872.3	3.872
90.8577	1.1572	65.2661	3654.79	3.655	0.9072	51.1	3923.5	3.924
95.1139	1.1632	65.6022	3692.53	3.693	0.9132	51.5	3975.2	3.975
99.3806	1.1691	65.9391	3730.55	3.731	0.9191	51.8	4027.4	4.027
100	1.17	65.988	3736.09	3.736	0.92	51.8	4035.0	4.035
103.658	1.1729	66.1530	3754.80	3.755	0.9229	52.0	4060.7	4.061
107.945	1.1764	66.3465	3776.79	3.777	0.9264	52.2	4091.0	4.091
112.241	1.1798	66.5403	3798.89	3.799	0.9298	52.4	4121.4	4.121
116.546	1.1832	66.7345	3821.10	3.821	0.9332	52.6	4152.0	4.152
120.856	1.1867	66.9290	3843.41	3.843	0.9367	52.8	4182.7	4.183
125.171	1.1901	67.1237	3865.80	3.866	0.9401	53.0	4213.6	4.214
129.269	1.1934	67.3086	3887.13	3.887	0.9434	53.2	4243.0	4.243
133.370	1.1967	67.4936	3908.53	3.909	0.9467	53.3	4272.6	4.273
137.690	1.2002	67.6886	3931.14	3.931	0.9502	53.5	4303.8	4.304
142.009	1.2036	67.8834	3953.80	3.954	0.9536	53.7	4335.2	4.335
146.328	1.2071	68.0783	3976.53	3.977	0.9571	53.9	4366.7	4.367
150	1.21	68.244	3995.91	3.996	0.96	54.1	4393.5	4.394
150.646	1.2104	68.2658	3998.48	3.998	0.9605	54.1	4398.2	4.398
154.965	1.2130	68.4120	4015.61	4.016	0.9639	54.3	4429.9	4.430
158.565	1.2151	68.5338	4029.93	4.030	0.9668	54.5	4456.5	4.457
160	1.24	69.936	4196.52	4.197	1	56.4	4767.3	4.767

Wind interference case:

a. Surrounding Structures

The plan view of the proposed Bellary thermal power station is shown in figure 3 and 4, the figure shows the two cooling tower, two chimneys, and other structures such as ESP, Boilers, and power house. For simulation of vicinity terrain around the proposed cooling towers, all the adjoining structures as mentioned above are to be included.

b. Site Location

The site of Bellary thermal power plant stage – II expansion is located at Bellary district in the State of Karnataka, India. The general terrain around the TPS location is in category 2 with open terrain with well scattered obstructions having heights generally between 1.5 to 10m

c. Wind Speed

The basic wind speed (Vb), from figure 1 of IS: 875 (Part 3) – 1987, is 39m/sec at Bellary. Basic wind speed is based on peak gust velocity averaged over a short time interval of about 3 seconds and corresponds to mean heights 10 m above ground level in an open terrain (Category 2) for a 50 year return period. The basic wind speed is modified to include the following effects to get design wind velocity at a height (Vz) for the structure:

Fig.2 Picture of instrumented NDCT along with other nearby plant structures for interference study in the wind tunnel (typical orientation).

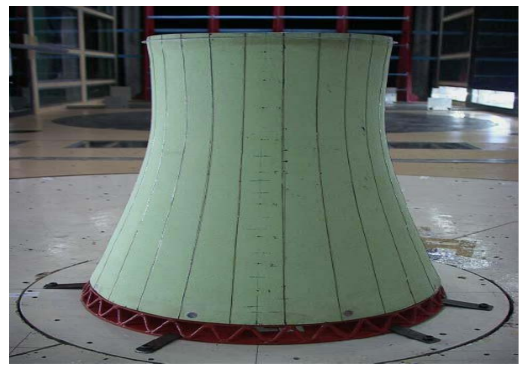

Fig 3 Isolated case of cooling tower

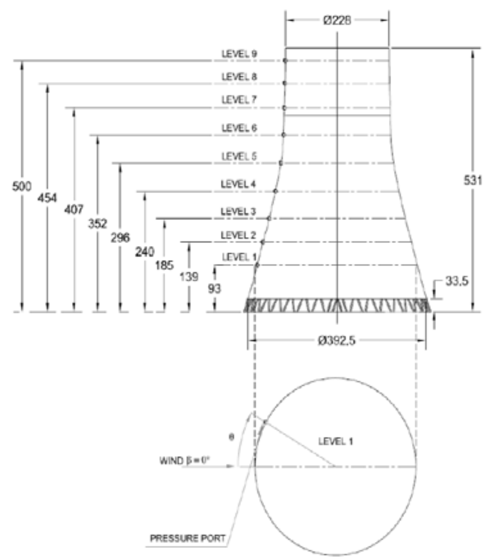

Fig.4 Sectional elevation of the pressure model of NDCT

A NDCT model of 1:300 scales was tested under simulated flow conditions for interference configurations. The mean pressure data has been obtained at nine different heights all around the periphery of the model in 15o interval.

The highest net pressure coefficient is obtained as 1.436, when the wind incidence angle is about 0°.

The minimum value of Cp is about -0.934, when the wind incidence angle is about 330° and occurring at about 105° angle in azimuth with respect to wind.

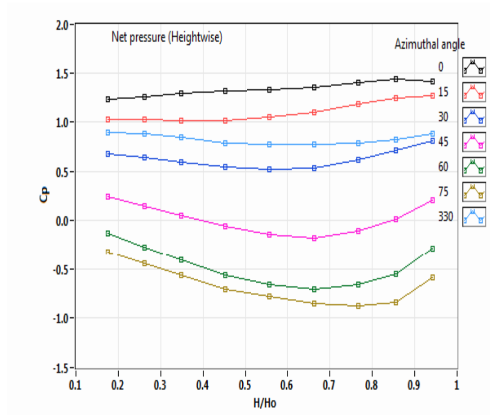

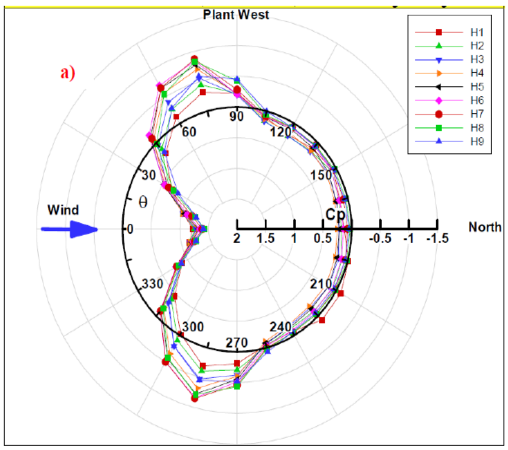

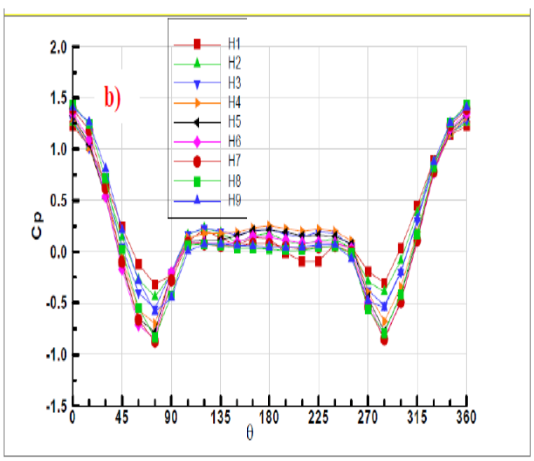

Fig.5 Interference case, wind incidence angle = 0 degree

a) Cp distribution along the periphery in polar plot

b) Cp distribution along the periphery in X-Y plot

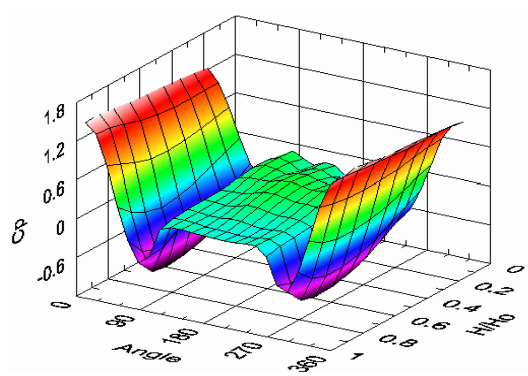

Fig.6Net pressure coefficient distribution on the NDCT for interference case, wind incidence angle = 0 degree

c) Cp distribution along the height

d) Cp distribution in 3D plot

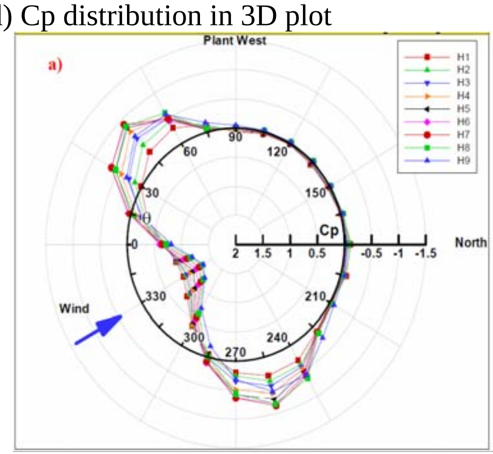

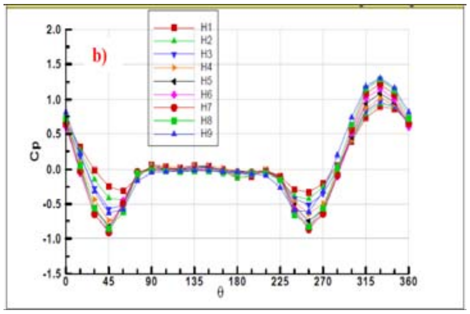

Fig.7 Interference case, wind incidence angle = 30 degree

a) Cp distribution along the periphery in polar plot

b) Cp distribution along the periphery in X-Y plot

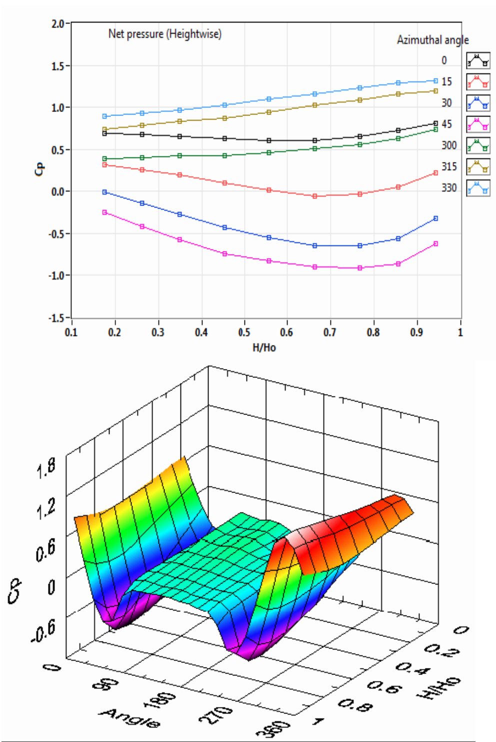

Fig.8 Net pressure coefficient distribution on the NDCT for interference case, wind incidence angle = 30 degree

c) Cp distribution along the height

d) Cp distribution in 3D plot

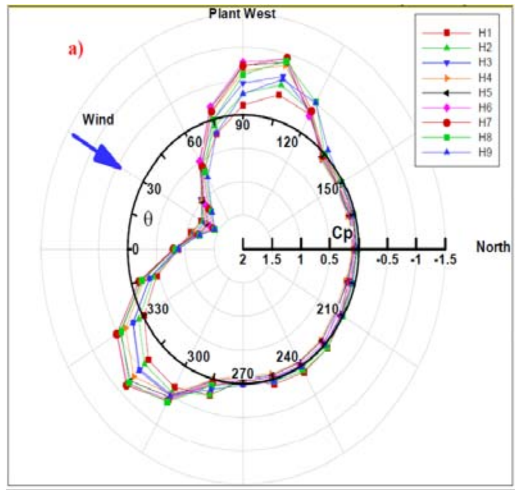

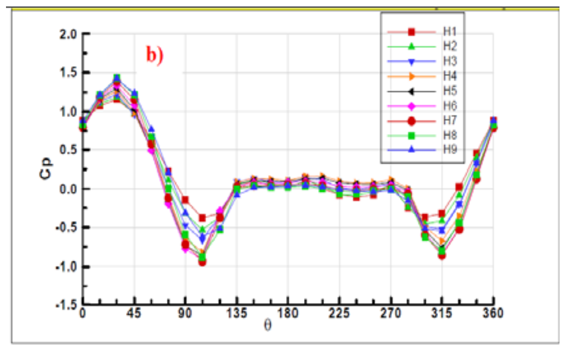

Fig.9 Interference case, wind incidence angle = 330 degree

a) Cp distribution along the periphery in polar plot

b) Cp distribution along the periphery in X-Y plot

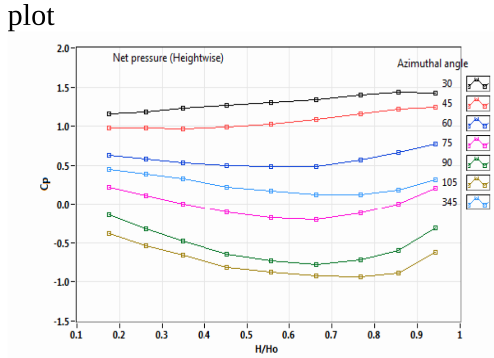

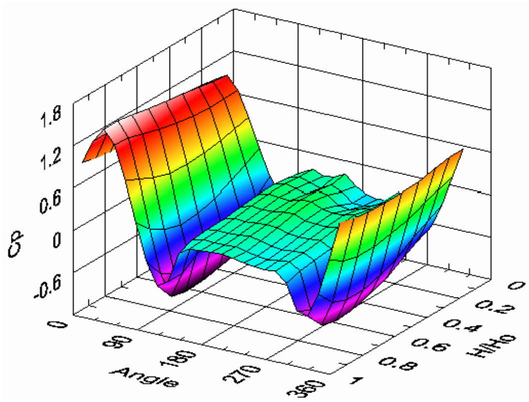

Fig. 10 Net pressure coefficient distribution on the NDCT for interference case, wind incidence angle = 330 degree

c) Cp distribution along the height
d) Cp distribution in 3D plot

Modeling and Meshing

The structure is modeled using beam and plate elements available in Staad Pro. v8i. The shells are meshed using quadratic 4 node plate element, raker column is modeled using 3D beam element and pedestal, pond wall is modeled by 4 node quadrilateral elements. The ring beam at the the base of the shell which is modeled by using 3 nodded triangular elements. The cooling tower shell is supported by diagonal columns called raker columns which are fixed at the base.

Finite element model of the problem generated using Staad Pro is shown in Fig. 11. Therefore the total number of the nodes and elements used in the entire model is 2948 and 2684 respectively. Node to node connection is used to join the elements and 88 numbers of 3D beam members are used to model the raker columns.

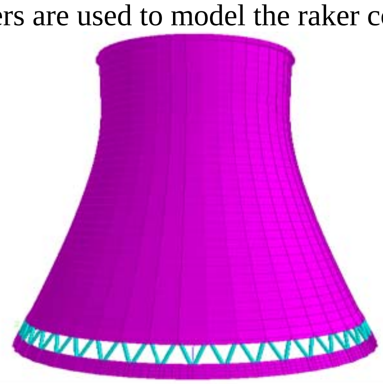

Fig. 11 Finite Element Model of cooling tower

Validation of the Model

Results of the numerical simulation are compared with that obtained by the existing cooling tower is given in Table 2. It can be seen that the deflection of the shell and Raker column predicted by present study is more by about 19.4% and 24% respectively.

The Meridional Stress distribution along the length and circumferential stress distribution at the ring beam level are shown in Fig. 12 & 13. It is observed that stresses obtained by the present study are more compared to the existing Natural Draught Cooling Tower. It can be observed that 8.86% more Meridional stress in present study compared to existing structure and in circumferential stress is about 9.43% more compared to existing structure.

It can be observed that the results of present study are in close agreement with the existing structure. Thus, the numerical model is validated.

Table 2 Validation Of The Numerical Model By Considering Displacement Due To Wind

Displacement in m due to wind load at extreme top level	Present study	Existing NDCT
shell	0.048	0.042
Raker column	0.0031	0.0025

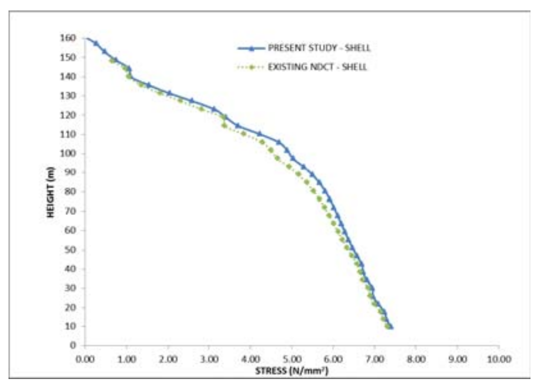

Fig.12 Meridional stress distribution

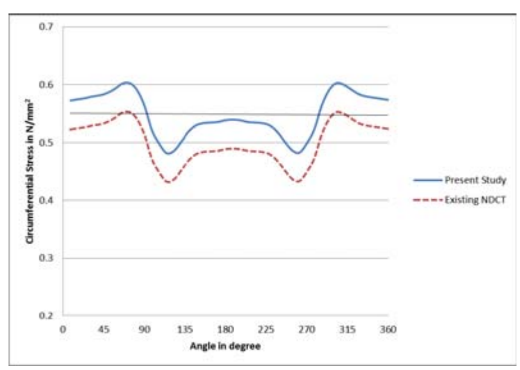

Fig.13 Circumferential stress distribution at ring beam level

Conclusions

Based on the present numerical investigation which includes circumferential pressure variation along the periphery as well as deflection control along the height of the tower for various wind incidence angle, the following conclusions are drawn:

The highest net pressure coefficient is obtained as 1.436, when the wind incidence angle is about 0°. The value approaches to a minimum value of about -0.934, when the wind incidence angle is about 330° and occurring at about 105° angle.

The deflection of the shell and Raker column predicted by present study is more by about 19.4% and 24% respectively compared to existing structure.

It can be observed that, Meridional stress is 8.86% more in present study compared to existing structure and circumferential stress is about 9.43% more compared to existing structure.

The results of present study are in close agreement with the existing NDCT. Thus, the numerical model is validated.

REFERENCES

[1] IS: 11504 1985, "Criteria for structural design of reinforced concrete natural draught cooling towers", Indian Standard Institution, BDC 38.

[2] IS: 875 (Part 3) Draft Revision "Indian Standard Code of Practice for Design Loads (Other than Earthquake) for Buildings and Structures, Part 3, Wind Loads", Bureau of Indian Standards, New Delhi.

[3] Selvi Rajan, S., G. Ramesh Babu, S. Arunachalam and N. Lakshmanan, "Interference factors for natural draught cooling towers based on wind tunnel experiments", Report No.10, MLP 140 41, CSIR-SERC, November 2010

[4] Selvi Rajan. S., S. Arunachalam, G. Ramesh Babu, P. Harikrishna, A. Abraham, S. Chitra Ganapathi, S. Sankar, Nagesh R.Iyer, "Wind tunnel experimental investigations on natural draught cooling towers including interference effects - Pressure Measurement", M/s. Nuclear Power Corporation of India Limited, Mumbai, Report No. SSP 075 41, March 2010.

[5] Dieter Busch., Reinhard Harte., Hans-Jurgen Niemann., (1998), "Study of proposed 200 m high natural draught cooloing tower at power plant Frimmerdorf / Germany", Engineering Structures, Vol. 20, 10, 920-927

[6] Poddar, K. *Proceedings of the National Conference on Wind Tunnel Testing, IIT Kanpur, July 2007*.

[7] G. Murali, C. M. Vivek Vardhan and B. V. Prasanth Kumar Reddy "*Response of Natural Draught Cooling Towers to wind loads", ARPN Journal of Engineering and Applied Sciences Vol. 7, No. 1, (January 2012).*

[8] N. Krishna Raju. *Adavanced Reinforced Concrete design of structures,chapter-12 Hyperbolic Cooling Towers (2010) Page 228*-233.

[9] Boseman, P.B., Strickland, I.G., and Prukl, R.P., "Strengthening of natural draught cooling tower shells with stiffening rings", Engineering Structures, Vol.20, No.10, 1998, pp.909-914.

[10] Busch, D., Harte, R., and Neimann, H.J., " Study of proposed 200m high natural draught cooling tower at power plant Frimmersdorf/Germany", Engineering Structures Vol.20, No.10, 1998, pp.920-927.

[11] Orlando, M., "Wind-induced interference effects on two adjacent cooling towers", Engineering Structures Vol.23, 2001, pp.979-992.

Advances in Milling Machine Using CAD/CAM: A Review

Ms.Prajakta H. Dahake[1], Ms.Nikita R. Sahakar[2], Mr.P.A.Gadge[3]

[1] Assit Professor, Mechanical Engineering Department, DBACER, Nagpur

[2] Student, M.Tech. CADMA, Mechanical Engineering Department, DBACER, Nagpur

[3] Assit Professor, Mechanical Engineering Department, VMIT, Nagpur

[1] E-Mail ID: praju_dahake1@yahoo.co.in

ABSTRACT

The development of unmanned machining systems has been a recent focus of manufacturing research. The conventional milling machine removes metal with a revolving cutting tool called a milling cutter. For this, CNC machines are in use. CNC machine operates on part program. This program includes several G-codes and M-codes. This program is generated by skilled operators. This may cause error in geometry. Also increases labor cost. Thus new technology of milling operation is conceptualized to reduce these problems using CAD/CAM. In this, firstly part design is created in CAD software like CATIA, ProE etc. This part design is fed in CAM software. Accordingly, coordinates forms. Also program is generated. According to that program, cutting tool operates to produce required part.

1. INTRODUCTION

1.1 Milling Machine

Milling machines were first invented and developed by Eli Whitney to mass produce interchangeable musket parts. The milling machine removes metal with a revolving cutting tool called a milling cutter. With various attachments, milling machines can be used for boring, slotting, circular milling dividing, and drilling. This machine can also be used for cutting keyways, racks and gears and for fluting taps and reamers. Milling machines are basically classified as being horizontal or vertical to indicate the axis of the milling machine spindle. These machines are also classified as knee-type, ram-type, manufacturing or bed type, and planer-type milling machines. Most machines have self-contained electric drive motors, coolant systems, variable spindle speeds, and power operated table feeds.

1.2 CNC milling machine

Computer Numerical Control (CNC) Milling is the most common form of CNC. CNC mills can perform the functions of drilling and often turning. CNC Mills are classified according to the number of axes that they possess. Axes are labeled as x and y for horizontal movement, and z for vertical movement. CNC milling machines are traditionally programmed using a set of commands known as G-codes and M-codes. G-codes and M-codes represent specific CNC functions in alphanumeric format.

1.3 New technology

A table top mini milling machine is produced. This milling machine is interfaced with the CNC machine. Use of traditional manufacturing system using CNC requires part program to be fed by skilled operators. But sometimes there may be error and inaccuracy in manual part program. So as to reduce this error, new technology is conceptualized. In this technology, firstly part is designed in CAD tool. This part is transferred to the CAM tool. From geometry coordinates are generated and using these coordinates program is generated. According to program, cutting tool and workpiece moves to produce required part.

2. LITERATURE REVIEW

2.1 C. Doukas et al has given multisensory data for milling operations on the estimation of tool- wear**.** A cutting depth of 0.5mm has been used along with a feedrate of 1000mm/min. The experiment has been repeated at the spindle speed of 1350rpm and 2700rpm, to investigate the effect of cutting speed on the wear level. Every 15 min the process is paused and the inserts are removed and inspected under an optical microscope for the easurement of the tool wear level. This paper shows the results of a preliminary experimental investigation on tool-wear in end milling. Spindle torque and vibration signals were recorded during the process. A correlation between measured signals and tool-wear was attempted. Power consumption, as depicted from the current draw signal, can be associated with the sustainability evaluation of the milling operation, due to their directly correlation to the tool wear level.

Table 1. Setup Variables

Variables	S=1350	S2700
Cutting Speed	210m/min	420m/min
Feed Rate	1000mm/min	
Depth of cut	0.5mm	
Feed per tooth	0.15	0.5

A 3axis CNC knee mill, operating a spindle of 5Hp is being used for machining and it is capable of reaching approximately 3800 RPM. In order for the workpiece to be securely positioned on the machine table, an adaptor plate has been designed and manufactured, while also allowing the positioning of the acceleration sensor as close to the machining area as possible. Straight cutting passes have been performed, alongside the Y-axis of the machine, to minimize effects of feed direction changes. A cutting depth of 0.5mm has been used along with a feed rate of 1000mm/min. The experiment has been repeated at the spindle speed of 1350rpm and 2700rpm, to investigate the effect of cutting speed on the wear level. Every 15, 5 min the process is paused and the inserts are removed and inspected under an optical microscope for the measurement of the tool wears level.

2.2 Adam Hansela et al, has given idea for improving CNC machine tool geometric precision using manufacturing process analysis techniques. With the ever increasing demands for higher and higher accuracy on modern CNC equipment, the manufacturing processes for machining and assembling the structural components are an increasingly important factor in establishing a geometrically correct machine tool. Specifically, flatness, perpendicularity, parallelism, and straightness of interfacing surfaces determine whether the machine tool's basic accuracy. Exhibiting less geometric error allows other errors such as thermal growth, ball screw pitch error, and control error to be isolated and more easily corrected.

2.3.1 Jig and fixture design Parts of the machine tool are assembled in separate units as much as possible for optimal efficiency. X and Z rails are installed directly onto the bed, but the Y-axis rails are installed to the column in an independent station. For assembly workers to efficiently place and measure the rails during installation and adjustment, the column must be placed in the horizontal orientation on a jig with the rails facing upward. For stability and safety, a four point fixture was originally designed The geometric errors are predominately a factor of the machine tool machining and assembly process. Multiple orientations during fixturing in both assembly and machining result in significant distortions to the final assembled product. These are a result of cutting forces, fixturing deformations, gravity deformations, and bolt force deformation. By analyzing each process in detail using virtual simulation techniques, a high- fidelity model of the corresponding error at each manufacturing step can be achieved that is not physically measurable due to constraints of measurement equipment. Using simulated data as offset data in the machining process as well as in the jig and fixture design ensures a geometrically accurate final product.

2.3 Masakazu Soshia et al, has given the concept of Spindle rotational speed effect on milling process at low cutting speed**.** The spindle rotational speed fluctuates during milling due to intermittent cutting forces applied to the spindle, but the speed effect when machining with a relatively large cutter at low cutting speeds is still not clear. Table 1 shows the basic specifications for the motor. The maximum rotational speed and torque of the servomotor is 5,500 min-1, and 700 Nm respectively. The focus of this paper is to investigate the effect of spindle servomotor dynamic characteristics on milling processes at various rotational speeds. Based on the simulation and experimental studies, it was found that the cutting speed fluctuation is not negligible at low operation speeds and that the spindle servomotor dynamics affect the machining process and tool life. Thus, it was concluded that the spindle dynamics have to be carefully evaluated and chosen when testing machinability of metals, especially low rotational milling applications typically required for machining of difficult-to-cut materials.

A physical cutting test was conducted on a highly rigid 3-axis milling machine equipped with the high performance PMSM. A milling tool with a single insert was used to cut C55 carbon steel, and the results were compared to the simulation in order to verify model. The commanded rotational speed was set to 260 min-1 with required cutting torque of approximately 270 Nm. By adjusting the gain of the servomotor controller the high performance PMSM bandwidth was reduced to 100 Hz. The simulated motor response against the same torque at the same commanded rotational speed of 260 min-1. The predicted reduction in spindle speed and overshoot were relatively accurate, although there are differences while the cutter was engaging the material. This is mainly due to the torque disturbance being molded as a continuous input compared to the more complex physical torque profile, however this detail was not critical for the study.

2.4 Xiaoyan Zuo et al, revealed integrated geometric error compensation of machining processes on CNC machine tool". This paper presents an integrated geometric error model of machining system and compensation method on machine tools. Regarding a machine tool, fixtures, workpiece and tool as an assembly, an integrated geometric error model has been established.

The integrated error is modeled by the propagation and the accumulation of errors based on Jacobian-Torsor theory. It is different with previous model, in this model; all the geometric errors of machining system are converted into the machine tool instead of the workpiece machining surface. As is well known in the machine tool, there are 21 geometric error of a 3 axis milling machine tool, which can be measured by laser interferometer. Based on this integrated model and machine tool error, the combination of geometric errors of machining system reflect on the machine tool can be predicted. Finally, a new compensation method is proposed to realize the error compensation, NC program is corrected corresponding NC codes according to the predicted errors during virtual machining before it is fed to the actual machining.

2.5 B. Denkenaa et al, has suggested adaptive cutting force control on a milling machine with hybrid axis configuration. In the re-contouring process of aircraft engine components, the unknown geometry and inhomogeneous material properties of the workpiece are major challenges. For this reason a new repair process chain is supposed which consists of noncontact geometry identification, process simulation and NC-path planning, followed by a force controlled milling process. A new milling machine prototype is employed to ensure an effective force control loop. By use of a magnetic guided spindle slide, higher dynamics and precise tracking are enabled. Since variation of the process forces result in variable control plant characteristics, an indirect adaptive controller has been designed. Consequently, models of actuator and process are presented and the estimation of the present parameters by a recursive least square algorithm is outlined. Once the parameters are known, the control polynomials are calculated on the basis of a pole placement control approach. First experimental results of a force controlled milling process are put forward.

2.6 Matti Rantatalo et al, has given idea for milling machine spindle analysis using FEM and non-contact spindle excitation and response measurement. In this paper a method for analyzing lateral vibrations in a milling machine spindle is presented including finite-element modeling (FEM), magnetic excitation and inductive displacement measurements of the spindle response. The measurements can be conducted repeatedly without compromising safety procedures regarding human interaction with rotating high speed spindles. The measurements were analyzed and compared with the FEM simulations which incorporated a spindle speed sensitive bearing stiffness, a separate mass and stiffness radius and a stiffness radius sensitive shear deformation factor. The effect of the gyroscopic moment and the speed dependent bearing stiffness on the system dynamics were studied for different spindle speeds. Simulated mode shapes were experimentally verified by a scanning laser Doppler vibrometer. With increased spindle speed, a substantial change of the Eigen frequencies of the bearing-related Eigen modes was detected both in the simulations and in the measurements. The centrifugal force that acted on the bearing balls resulted in a softening of the bearing stiffness. This softening was shown to be more influential on the system dynamics than the gyroscopic moment of the rotor. The study performed indicates that predictions of high speed milling stability based on 0 rpm tap test can be inadequate.

2.7 Mohsen Soori et al, has given concept of virtual machining considering dimensional, geometrical and tool deflection errors in three- axis CNC milling machines. Virtual manufacturing systems can provide useful means for products to be manufactured without the need of physical testing on the shop floor. As a result, the time and cost of part production can be decreased. There are different error sources in machine tools such as tool deflection, geometrical deviations of moving axis and thermal distortions of machine tool structures. Some of these errors can be decreased by controlling the machining process and environmental parameters. However other errors like tool deflection and geometrical errors which have a big portion of the total error, need more attention.

This paper presents a virtual machining system in order to enforce dimensional, geometrical and tool deflection errors in three-axis milling operations. The system receives 21 dimensional and geometrical errors of a machine tool and machining codes of a specific part as input. The output of the system is the modified codes which will produce actual machined part in the virtual environment.

2.8 Chana Raksiri et. al, has revealed geometric and force errors compensation in a 3-axis cnc milling machine. This paper proposes a new off line error compensation model by taking into accounting of geometric and cutting force induced errors in a 3-axis CNC milling machine. Geometric error of a 3-axis milling machine composes of 21 components, which can be measured by laser interferometer within the working volume. Geometric error estimation determined by back-propagation neural network is proposed and used separately in the geometric error compensation model. Likewise, cutting force induced error estimation by back-propagation neural network determined based on a flat end mill behaviour observation is proposed and used separately in the cutting force induced error compensation model. Various experiments over a wide range of cutting conditions are carried out to investigate cutting force and machine error relation. Finally, the combination of geometric and cutting force induced errors is modeled by the combined back- propagation neural network. This unique model is used to compensate both geometric and cutting force induced errors simultaneously by a single model. Experimental tests have been carried out in order to validate the performance of geometric and cutting force induced errors compensation model.

2.9 B. Lauwers, et. al, introduced efficient NC- programming of multi-axes milling machines through the integration of tool path generation and NC-simulation. This paper describes the development of an "extended CAM system" for multi-axes milling, integrating tool path generation, axes transformation (post processing) and NC-simulation. The system performs an immediate verification of each generated cutter location and in case a collision occurs (e.g. between machine and part), it takes the appropriate action by applying a collision avoidance algorithm. Different collision avoidance algorithms have been implemented: change of tool orientation, selection of other machine axes configurations and simple tool retract. The effect of a tool orientation change on the quality of the machined surface has been studied in order to define the range of tool orientations that may be used for collision avoidance.

The off-line generation of collision free NC- programs for multi-axes milling operations mostly proceeds in two sequential steps. In a first step, the CAM module (tool path generation) calculates the trajectory of the milling cutter. Each tool posture is described by its tool tip (x,y,z) and tool orientation (i,j,k), both expressed in a workpiece co-ordinate system. Advanced CAM systems allow checking the tool path for micro (gauging) and macro collisions. Research and development on the avoidance of micro collisions is reported. Collisions between the tool (+ tool holder) and non-cutting areas of the part are classified as macro collisions. Most CAM systems retract the tool in case macro collisions occur, while only a few propose a collision avoidance algorithm by changing the tool orientation. In a second step, the tool path, output as a CLDATA- file, is converted by a NC-postprocessor to a machine specific NC-program.

3. CONCLUSION

This paper provides the details of the research work which has been carried out in the milling operation under various conditions. This milling machine is a very crucial element of any operation. The proposed mechanism uses CAD/CAM software for milling operation.

Traditional CNC milling machine uses manually generated NC part program. This may cause manual error in part program. Thus to avoid this error, new technology is conceptualized. CAD/CAM software makes it easier to generate NC part program directly from given geometry. So it reduces error, increases efficiency and improves accuracy.

Referances

[1] C. Doukas, et al, "On the estimation of tool- wear for milling operations based on multisensory data", *14th CIRP Conference on Modeling of Machining Operations (CIRP CMMO), vol.8, 2013, pg no. 415 - 420.*

[2] Masakazu Soshia, Nicholas Raymonda, Shinji Ishiib, "Spindle rotational speed effect on milling process at low cutting speed", *6th CIRP International Conference on High Performance Cutting, HPC2014, vol.14, 2014, pg. no. 159 - 163*

[3] Adam Hansela, Kazuo Yamasaki, Kyle Konishib, "Improving CNC Machine Tool Geometric Precision Using Manufacturing Process Analysis Techniques", *6th CIRP International Conference on High Performance Cutting, HPC2014, vol.14, 2014, pg. no. 263 - 268.*

[4] Xiaoyan Zuo, et al "Integrated geometric error compensation of machining processes on CNC machine tool", *14th CIRP Conference on Modeling of Machining Operations (CIRP CMMO), vol. 8, 2013, pg. no. 135 - 140.*

[5] B. Denkenaa, F. Floater, "Adaptive Cutting Force Control on a Milling Machine with Hybrid Axis Configuration", *3rd CIRP Conference on Process Machine Interactions (3rd PMI), vol. 4, 2012, pg. no. 109 - 114*

[6] Matti Rantatalo, et al, "Milling machine spindle analysis using FEM and non-contact spindle excitation and response measurement", *International Journal of Machine Tools & Manufacture, vol. 47, 2007, pg. no. 1034-1045*

[7] Mohsen Soori, Behrooz Arezzo, Mohsen Habibi, "Virtual machining considering dimensional, geometrical and tool deflection errors in three-axis CNC milling machines", *Journal of Manufacturing Systems, vol. 10, 2004, pg no. 222-232.*

[8] Chana Raksiri, Manukid Parnichkun, "Geometric and force errors compensation in a 3-axis CNC milling machine", *International Journal of Machine Tools & Manufacture, vol. 44, 2004, pg. no. 1283-1291*

[9] B. Lauwers, et al, "Efficient nc-programming of multi-axes milling machines through the integration of Tool path generation and nc-simulation", *2000.*

STRENGTH EVALUATION IN J-NOSE PANEL OF AN AIRCRAFT WING UNDER STATIC LOAD

Harisha k s[1], Biradar Mallikarjun[2]
[1]Student, IVthSemester M.Tech (Machine Design), [2] Assistant Professor,
[1,2]Mechanical Engineering Department
[1,2]Nagarjuna College of Engineering & Technology, Bengaluru-562110,
Affiliated to VTU, Belgaum, Karnataka, India
Email:[1]harishaks88@gmail.com [2]bmjun_phd@yahoo.co.in

Abstract- The sandwich construction has been recognized as a promising concept for structural design of light weight systems such as wings of aircraft. The strength evaluation J-nose sandwich panel of an aircraft wing under various types of loading. The sandwich composites are multilayered materials made by bonding stiff, high strength skin facings to low density core material. The main benefits of using the sandwich concept in structural components are the high stiffness and low weight ratios. A sandwich construction, which consists of two thin facing layers separated by a thick core, offers various advantages for design of weight critical structure. These structures can carry in-plane and out-of-plane loads and exhibit good stability under compression, keeping excellent strength to weight and stiffness to weight characteristics. Depending on the specific mission requirements of the structures, glass fiber reinforced polymer composites are used as the material of facings skins. The core shape and material may be utilized in the construction of sandwich among them; it has been known that the glass fiber reinforced polymer with honeycomb core has excellent properties with regard to weight savings and fabrication costs. In order to use these materials in different applications, the knowledge of their static behavior is required and detailed design procedures are presented for determining deflections of sandwich beams or panels and buckling of sandwich columns and simply supported panels under edge load.The modes of failure of sandwich under various loadings are illustrated and a better understanding of the various failure mechanisms under static loading condition is necessary and highly desirable.

The objective of this study is to develop a modeling approach to predict response of composite sandwich panels under static bending conditions . The different models including Mono-core and Multi-core were modeled in advanced finite element software. Comparison of mono core and multi core model predictions with experimental data on sandwich panel bending properties helped in establishing appropriate modeling approach. Analytical solutions were also used to verify the some of the mechanical properties such as bending stress and shear stress with the MSC NASTRAN/PATRAN results.

The sandwich panel consists of 2 layers of face sheets (Glass fiber reinforced polymer composites), with ply 1 has 0.3 mm thickness & ply 2 has 0.1 mm thickness and core (Mono and Multi core) is present between top and bottom face sheets which has 19.2 mm (Mono-core) and 9.4 mm (Multi-core) thickness.

Key words-Aircraft ,wing, Multilayer sandwich composite, sandwich panel, FEM, analytical

solution, MSC NASTRAN/PATRAN, glass fiber, Nomax flex core.

1. AIR CRAFT

Aircraft heavier than air flying machine, supported by aero foils, designed to obtain,when driven through the air at an angle inclined to the direction of motion,are action from the air approximately at right angles to their surface, the major parts of an aircraft with different composite materials such as CFRP,GFRP,Hybrid,Glare and majorly honeycomb is used in aircraft to reduce the weight as shown in Fig.1.

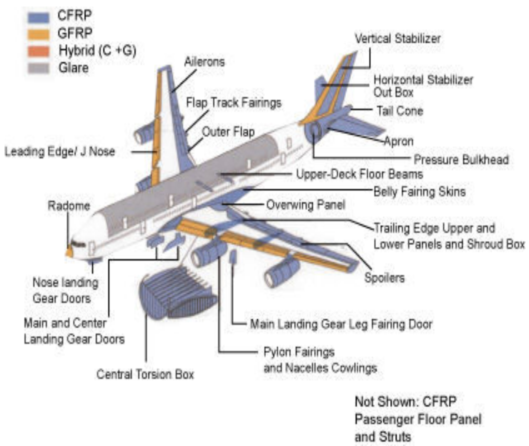

Fig.1 The major parts of an aircraft with different composite materials

II .WINGS

Providing lift is the main function of the wings of an aircraft. The wings consist of two essential parts. The internal wing structure as shown in Fig.2, consisting of spare ribs, stringers, and the external wing, which is the skin. Ribs give the shape to the wing section, support the skin (prevent buckling), Aerodynamic forces not only bend the wing, they also twist it.

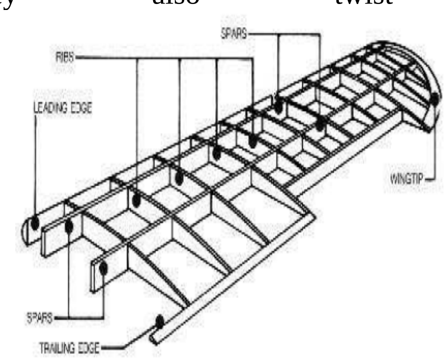

Fig.2 Internal structure of the wing.

The sand wich panels are most commonly used in air craft's to increase the strength. Most of the critical areas in J nose panel of an aircraft wing are lot of skin imperfections and core failure modes, therefore to increase stiffness and core strength in j-nose panel of an aircraft wing, a wing leading edge formed from honeycomb material and glass fiber reinforced polymer composite as shown in Fig.3.

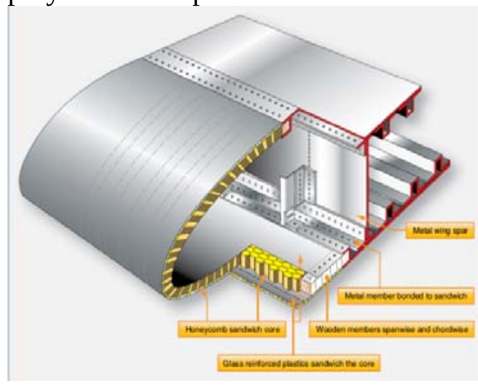

Fig.3 A wing leading edge formed from honeycomb material and glass fiber reinforced polymer composite.

III. INTRODUCTION

Composite sandwich panel have been increasingly used in aerospace industry for various applications such as floor panels, comportment partitions, bulkheads, and even the skin and wings. It is important to design light weight structure for aircraft operations, sandwich panel serves this requirement. The sandwich composites are multilayered materials made by bonding stiff, high strength skin facings to low density core material. The main benefits of using the sandwich concept in structural components are the high stiffness and low characteristics. In order to use these materials in different applications, the knowledge of their static behavior is required and a better weight ratios. These structures can carry in-plane and out-of-plane loads and exhibit good stability under compression, keeping excellent stiffness and strength to weight understanding of the various failure mechanisms under static loading condition is necessary and highly desirable.

M.M. Venugopal and S K Maharana [1]In this paper sandwich composites are multilayered materials made by bonding stiff, high strength skin facings to low density core material. These structures can carry in-plane and out-of-plane loads and exhibit good stability under compression, keeping excellent strength to weight and stiffness to weight characteristics. In order to use these materials in different applications, the knowledge of their static behavior is required and a better understanding of the various failure mechanisms under static loading condition is necessary and highly desirable.Belouettar and Abbadi [2] presented experimental investigation of static behavior of composite honeycomb material made up of aramide fibers and aluminium cores are investigated through four point bending test. The local and global parameters considered to evaluating behavior of sandwich composite, but results are not accurate due to the only experimental study is shown there is no comparison made with any other analytical method. Meyer-Piening [3] suggested that local failures in sandwich structures often occurred because of a lack of awareness of designers of important aspects such as the distribution of displacements through the thickness, axial forces in the face sheets, and the difference between the vertical deflections of upper and lower face sheets. Kemmochi and Uemura [4] investigated the stress distribution in sandwich beams made of three kinds of photo elastic materials under four-point bending. Juli F Davalos and Pizhong qiao [5] studied design modeling and experimental characterization of a FRP honeycomb panel with sinusoidal core geometry in the panel and extending vertically between face laminates. The finite element modeling of test sample is conducted. The result correlates with analytical prediction and experimental values excellent matching is achieved between results.

A.Bezazi and A El Mahi [6] studied analysis of stiffness during static test of sandwich panels and their components. Sandwich panel made of glass fiber and epoxy resin, are subjected to three point bending tests, poly vinyl chloride cores of different densities were investigated in this study, the effect of core densities and its thickness on the behavior is highlighted this paper proves that sandwich structure has better mechanical characteristics compared to its components. Engin M, Reis and Sami.H.Rize kalla [7] presented material characteristics of 3D FRP sandwich panel this paper investigated, flexural, shear, tensile and compressive behavior of sandwich panel face sheet made of FRP and GFRP with foam core the top and bottom face sheets connecter with thick fibers, this paper summarized extensive experimental program discussed many parameters to evaluate sandwich panel behaviors. Jamal Arbaoui, Yves Schmitt and Franc¸ois-Xavier Royer [8] in this paper, an experimental investigation, an analytical analysis and a numerical model of a typical four-point bending test on a polypropylene honeycomb multi-layer sandwich panel are proposed. The polypropylene honeycomb core is modelled as a single solid and multi-layer of equivalent material properties. Analytical and numerical (finite element) homogenization approaches are used to compute the effective properties of the single honeycomb core and analytical homogenization of the multi-layer one. The results obtained by numerical simulation (finite element) of four-point bending are compared with the experimental results of a polypropylene honeycomb core/composite facing multi-layer sandwich structures

IV. DESCRIPTION OF PROBLEM

The four point bending test composite (nomax flex core) sandwich panel of size 700 mm x 75 mm x 20 mm, under uniform static four point bend loading was considered. The sandwich panel consists of 2 layers of face sheets (Glass fiber reinforced polymer composites), with ply 1 has 0.3 mm thickness & ply 2 has 0.1 mm thickness and core (Mono and Multi core) is present between top and bottom face sheets which has 19.2 mm (Mono-core) and 9.4 mm (Multi-core) thickness. The face plate laid stacking sequence is [0/90]. A sandwich panel that consists of GFRP face sheets and Nomax Flex core has been considered for the analysis.

V.FINITE ELEMENT MODELING

The finite element software was used to model the sandwich panel, in this analysis both mono core and multi core models are created by using following element type based on convergence test and it is used throughout the study 2D-non linear layered shell element called shell 91 is used for modeling of thick sandwich structures this has ability to take up to 100 layers. 3D 8 nodded multi layered solid element called as solid46, is used to model for 3D sandwich panel this element takes orthotropic material properties, layered material direction angles and layered thicknesses. The geometry, nodal locations and coordinate system of the elements are shown on the Fig.4, and also the core uses 3D anisotropic structural solid element called solid64. This element has eight nodes having three degree of freedom at each node; translation in x, y, and z directions. The element has stress stiffening and large deflection capabilities and the element has various applications, such as for crystals and composites.

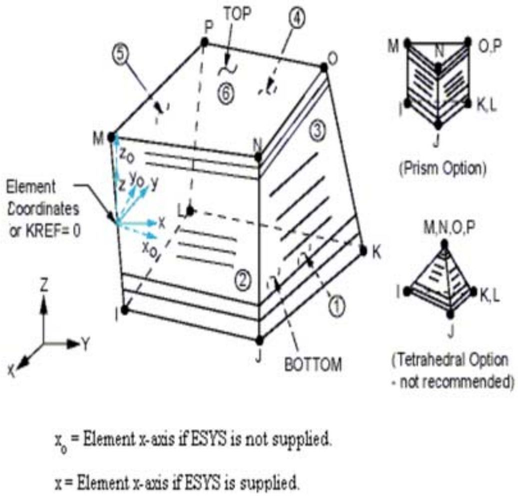

Fig.4 Element geometry of 3D layered solid element.

Fig.5 Finite Element modeling of composite sandwich panel – 3D Mono Core.

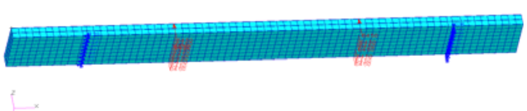

Fig.6 Finite Element modelling of composite sandwich panel – 3D MultiCore.

The solid model accounts for a three dimensional nature uses solid layered element to model the two face sheets and anisotropic solid element used for model core. This 3D sandwich panel model was able to accommodate both orthotropic and anisotropic material properties. Finite Element modeling of composite sandwich panel – 3D Mono Core as shown in Fig.5 & Finite Element modelling of composite sandwich panel – 3D MultiCore as shown in Fig.6.

VI.MATERIAL PROPERTIES OF SANDWICH PANEL

The four point bending test composite sandwich panel of size 700 mm x 75 mm x 20 mm, under uniform static four point bend loading was considered. The sandwich panel consists of 2 layers of face sheets, with ply 1 has 0.3 mm thickness & ply 2 has 0.1 mm thickness and core (Mono and Multi core) is present between top and bottom face sheets which has 19.2 mm (Mono-core) and 9.4 mm (Multi-core) thickness. The material properties of composite sandwich panel are given by Table.1. Material Properties of composite sandwich panel – Mono core as shown in Fig.7 & Material Properties of composite sandwich panel – Multicore as shown in Fig.8.

Material	Ply	Core
E_{11}, Mpa	28800	1
E_{22}, Mpa	28800	1
E_{33}, Mpa	28800	240
G_{12}, Mpa	3000	1
G_{23}, Mpa	337	30
G_{13}, Mpa	3000	48
v_{12}	0.13	0.5
v_{23}	0.01	0.0
v_{13}	0.13	0.0

Table.1 Material properties of composite sandwich panel.

Fig.7 Material Properties of composite sandwich panel –Mono core

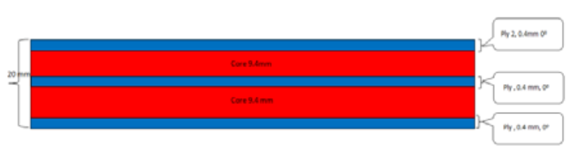

Fig.8 Material Properties of composite sandwich panel – Multi core

VII.BOUNDARY CONDITIONS

The Fig.9 shows the boundary conditions adapted for analyzing sandwich panel. The two supporting points of either end of panel is fixed at translation at Z=0 and static bending load is applied opposite to the supporting point and Below Fig.10 shows four point bending test specimen dimensions. FEA Set-up of Bending Test (Loads and BCs) For Mono-core Sandwich Panel as shown in Fig.11 & FEA Set-up of Bending Test (Loads and BCs) For Multi-core Sandwich Panel as shown Fig.12.

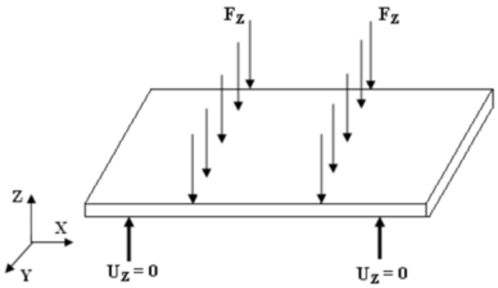

Fig.9 Load applications and boundary condition

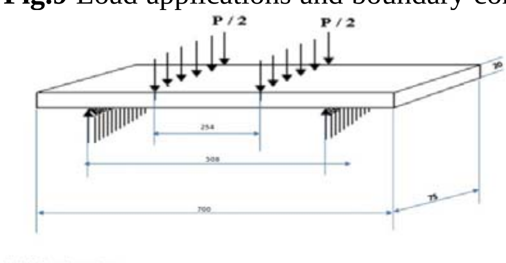

Fig.10 Four Point Bending Test Specimen

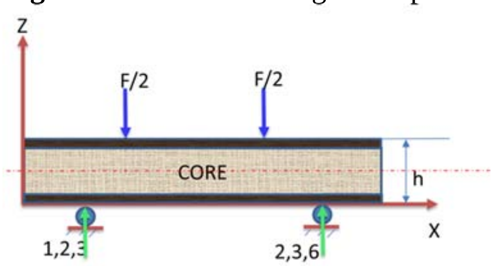

Fig.11 FEA Set-up of Bending Test (Loads and BCs) For Mono-core Sandwich Panel

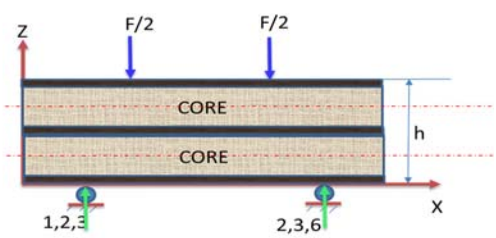

Fig.12 FEA Set-up of Bending Test (Loads and BCs) For Multi-core Sandwich Panel.

VIII.FAILURE MODES

Designers of sandwich panels must ensure that all potential failure modes are considered in their analysis. A summary of the key failure modes is shown below:

FAILURE MODE	DESCRIPTION	FAILURE MITIGATION
• Core Wrinkling *Buckling over many cells* $\sigma < \sigma_{Wr} = 0.82 E_f \left[\frac{E_c t_f}{E_f t_c}\right]^{1/2}$	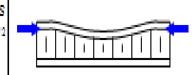	• Choose thin core or thick skin
• Intracell Dimpling *Buckling in single cell* $\sigma < \sigma_{Dimp} = 2\frac{E_f}{\lambda}\left[\frac{t_f}{S}\right]^2$	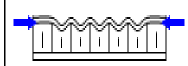	• Choose small cell size
• Core Crimping *Combined skin buckling* $\sigma < \sigma_{Cr} = \frac{t_c G_c}{2t_f}$	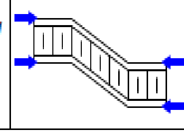	• Choose thick core or stronger core

IX.FEA VALIDATION

FEM validation has been carried-out by considering the composite sandwich panel and the properties that are published in journal paper (Ref. 1).

The validation study of composite sandwich panel of size 800 mm x 300 mm x 17.4 mm, under uniform static four point bend loading was considered. The sandwich panel consists of 8 layers of face sheets, each 0.15 mm thickness and core is present between top and bottom face sheets which has 15 mm thickness. The face plate has the stacking sequence [45/-45/0/90].

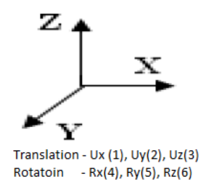

Below Fig.13 shows four point bending test specimen dimensions of a journal paper (Ref. 1)

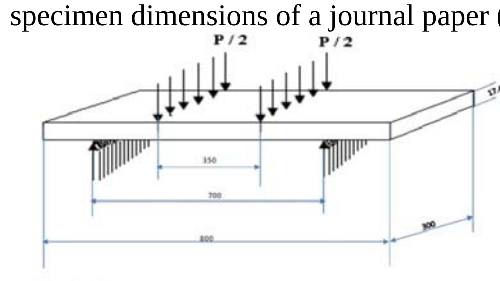

Fig.13 Four Point Bending Test Specimen

X.RESULTS AND DISCUSSION

An application, a full size GFRP honeycomb panel of size 700 mm x 75 mm x 20 mm is tested under static four point bending and also analyzed by FE method. The panel bottom surface is simply supported over a span 700mm and subjected to a pitch load. Four point loading condition are applied at mid span to simulate symmetric condition. FE method is conducted at two modeling condition: (1) Mono core Sandwich panel model, (2) Multi cores Sandwich panel model, for each model condition, the deflections were recorded at mid span with corresponding stresses.

Load (P) Kg	Load (P) N	Deflection, mm			% Comparison		
		Mono Core (LW-dir)	Mono Core (WL-dir)	Multi Core	Result 1Vs2	Result 1Vs3	Result 2Vs3
100	981	11.83	12.34	12.3	-4.31%	-3.97%	0.32%
200	1962	23.66	24.68	24.6	-4.31%	-3.97%	0.32%
300	2943	35.49	37.02	36.9	-4.31%	-3.97%	0.32%
400	3924	47.32	49.36	49.2	-4.31%	-3.97%	0.32%
500	4905	59.15	61.70	61.5	-4.31%	-3.97%	0.32%

A sandwich panel with equivalent 2 layers (top and bottom faces and core) is modeled. For simplicity and verification purposes, the equivalent properties obtained for face laminates and core are used directly in the model. In case of Mono core Sandwich panel model the face laminates and core are each modeled in single layer using 8-noded shall element called SHELL91. The displacement contours obtained from MSC NASTRAN/PATRAN, Deflection plot of composite sandwich panel – Mono core (LW) for Load case 1 are shown in Fig.14. In case of 3D Sandwich panel model the face sheet and core are modeled in three different layers using 8-noded solid elements called SOLID 46 for two face sheets and SOLID 64 for Core. The displacement contours obtained from MSC NASTRAN/PATRAN. Deflection plot of composite sandwich panel – Mono core (WL) for Load case 1, are shown in Fig.15& Deflection plot of composite sandwich panel – Multi core for Load case 1,as shown in Fig.16
Comparison of 3D deflection for all the load cases (Mono & Multi core) as shown in Table 2, the mono core and multi core Sandwich panel FE predictions based on equivalent material properties compare favorably with experimental data.

The 3D-Results comparison– Multicore (2 layers of core,3 layers of core and 5 layers of core). The height of the sandwich remains same i.e. 20 mm for all the cases as shown in Table 3 and deflection plot for Loadcase 1as shown in Fig.17,for every load case deflection of FEM result can be obtaind, those results comparison of deflection for all the load cases (Experimental Vs FEM) as shown in the Table .4,

Table.2 Comparison of 3D deflection for all the load cases (Mono & Multi core)

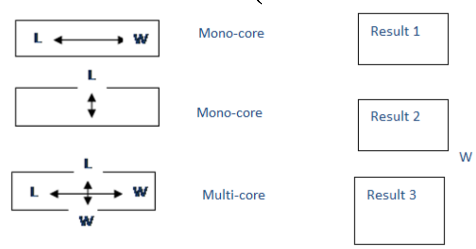

Load (P) Kg	Deflection, mm				
	Mono Core (LW-dir)	Mono Core (WL-dir)	Multi core (2 cores)	Multi Core (3 cores)	Multi Core (5 cores)
	Thickness Core = 19.2 Total Face sheet = 0.8	Thickness Core = 19.2 Total Face sheet = 0.8	Thickness Core = 18.8 Total Face sheet = 1.2	Thickness Core = 18.4 Total Face sheet = 1.6	Thickness Core = 18.0 Total Face sheet = 2.0
100	11.83	12.34	12.3	12.02	9.06
200	23.66	24.68	24.6	24.04	18.12
300	35.49	37.02	36.9	36.06	27.18
400	47.32	49.36	49.2	48.08	36.24
500	59.15	61.70	61.5	60.1	45.3

Table 3. 3D-Results comparison– Multicore (2 layers of core,3 layers of core and 5 layers of core). The height of the sandwhich remains same i.e. 20 mm for all the cases.

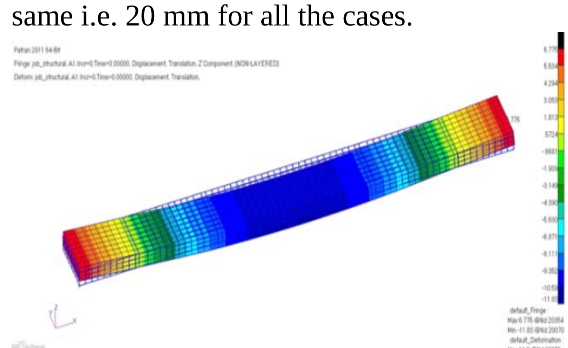

Fig.14 Deflection plot of composite sandwich

panel – Mono core (LW) for Load case 1

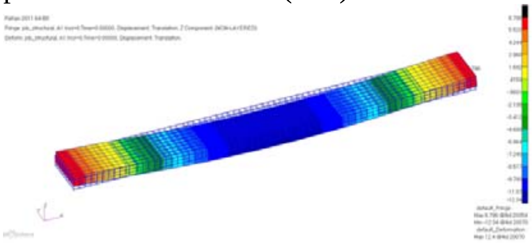

Fig.15 Deflection plot of composite sandwich panel – Mono core (WL) for Load case 1

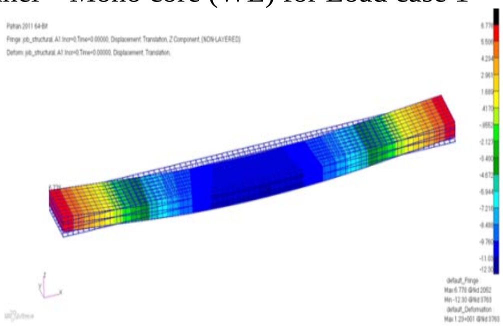

Fig.16 Deflection plot of composite sandwich panel – Multi core for Load case 1

Load Case	Load (P) KN	Experimental, mm	FE Deflection, mm	Deviation
1	2	4.6	4.53	1.52%
2	2.5	5.9	5.85	
3	3	6.9	6.83	
4	3.5	8	7.97	
5	4	9.1	9.05	
6	4.5	10.3	10.26	
7	5	11.5	11.48	
8	5.5	12.7	12.67	
9	6	13.8	13.73	
10	6.5	15.2	15.16	
11	7	16.2	16.18	
12	7.5	17.3	17.26	
13	8	18.4	18.33	0.38%
14	8.5	19.7	19.67	

Table.4 Comparison of deflection for all the load cases (Experimental Vs FEM)

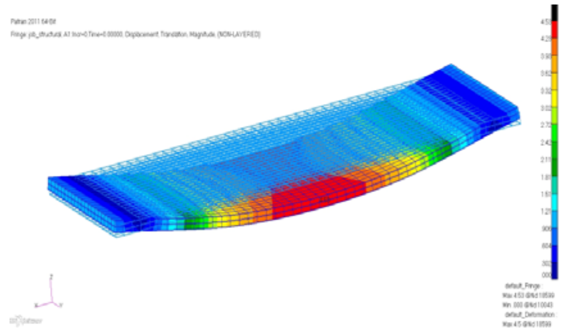

Fig.17 Deflection plot for Loadcase 1

XI.CONCLUSIONS

This paper presents a combined Finite element modeling and experimental analysis of glass fiber composite sandwich panel. The core consists of Nomax honey comb structure presented in between top and bottom face laminate. The emphasis of this study is on evaluation of deflection, under static four point bending condition. The mono core and multi core FE model predictions correlate with experimental results of Sandwich specimen. The predicted deflection in this study is success fully matching the response of glass fiber composite sandwich panels. The multicore FE model under static loading condition is closely matching with experimental deflection. Displacements reduces on increasing the numbers of cores. This may be because increasing the number of ply layers which adds to stiffness.

XII.ACKNOWLEDGEMENT

The author's acknowledged the institute authorities for supporting the present work to be carried out in the institute. I would like to thank my guide Assistant Professor **BiradarMallikarjun** and this part of the work done by **NCET** Bangalore.

REFERENCES

[1] **M.M. Venugopal, S K Maharana, K S Badarinarayan,** "*Finite Element Evaluation of Composite Sandwich Panel Under Static Four Point Bending Load*", JEST-M, Vol. 2, Issue 1, 2013 .

[2] **Belouettar and Abbadi**, "*Experimental investigation of static and fatigue behavior of composites honeycomb materials using four point bending tests*", Composite Science Technology 2003; 70:2556–64.

[3] **Meyer-Piening H-R,** "*Remarks on higher order sandwich stress and deflection analysis*". In: Olsson K-A, Reichard RP, editors. Proceedings of the first international Conf on Sandwich Constructions 1989 P107–27.

[4] **Kemmochi and Uemura,** "*The stress distribution in sandwich beams made of three kinds of photo elastic materials under four-point bending*". Journal of Mechanics, 2356-23; Jun 2000.

[5] **Juli F Davalos, and Pizhong qiao**, "*modeling and characterization of fiber reinforced plastic honeycomb sandwich panel for highway bridge applications*". Mechanics of materials 1998; 5642-13 *material in three point bending Part 1. Static tests*" Journal of composites 2001; 4281-14.

[6] **A Bezazi, and A El Mahi,** "*Experimental analysis of behavior and damage of sandwich composite".*

[7] **Engin M, Reis and Sami.H.Rize kalla** "*Material characteristics of 3D FRP sandwich panel*". 3rd edition oxford press.

[8] **Jamal Arbaoui, Yves Schmitt and Franc¸ois-Xavier Royer,** *"numerical simulation and experimental bending behaviour of multi-layer sandwich structureS"* journal of theoretical and applied mechanics 52, 2, pp. 431-442, warsaw 2014.

BENDING STRESS ANALYSIS ON INCONEL-718 COATING MATERIAL BY EXPERIMENTAL AND FE METHOD

[1]Umesh.G, [2]Biradar Mallikarjun, [3]Dr.C.S.Ramesh
[1]PG Student, Nagarjuna college of engineering and technology, Bangalore
[2]Professor, Nagarjuna college of engineering and technology, Bangalore
[3]Professor, PES Institute of technology, Bangalore
Email: [1]Umesh.g8055@gmail.com, [2]bmjun_phd@yahoo.co.in

Abstract— High Velocity Oxy-Fuel (HVOF) spraying of Inconel-718 powders on mild steel sheets is carried out. Three-point bending tests are carried out to examine the mechanical properties of the coating. Stress fields developed during the tests are simulated using Finite Element Method (FEM). ANSYS package is used to predict the stress field. Three- and two-dimensional modeling of the coating and substrate material are considered and the predictions of load–displacement characteristics are compared with the experimental results. Since two-dimensional predictions agree well with the experimental data, two-dimensional model is employed in the simulations. Consequently, crack initiation and propagation at coating and substrate material interface occurring may be determined, similarly above steps were carried out for different thickness and for different loading conditions of coating materials.

***Index Terms*— Bending Stresses, Inconel-718, Coating materials, Mild Steel Substrate.**

I. INTRODUCTION

High velocity oxy-fuel (HVOF) deposition is widely used in industry as protective coating of various materials. In HVOF coating process, powders are inserted in a gas stream with a high flame temperature; therefore, the particles are heated rapidly and accelerated almost the same speed of gas jet. The velocity of the particle reaches well above the speed of sound before impacting onto the work piece surface. The splats (powder at molten state in the jet) make bonds to the substrate surface through mechanical locking onset of impacting. HVOF spraying can produce high quality and low porosity coatings, which may have good interface properties. Coating is a covering that is applied to an object. The aim of applying coatings is to improve surface properties of a bulk material usually referred to as a substrate. One can improve amongst others appearance, adhesion, wetability, corrosion resistance, wear resistance, scratch resistance, etc. They may be applied as liquids, gases or solids. The thermal spray is to melt material feedstock (wire or powder), to accelerate the melt to impact on a substrate where rapid solidification and deposit buildup occur.

High velocity oxy fuel (HVOF) coating is a thermal spray technique used to deposit protective coatings on a substrate. A blend of fuel (gaseous or liquid) and oxygen is injected into a torch and burned. The combustion products flow through a nozzle, that the stream of hot gas and powder is directed towards the surface to be coated. HVOF thermal spray applications are in the fields of Aerospace, Power generation, Automotive, Transportation

/ Heavy equipment, Printing and paper / pulp equipment, Glass manufacture, Metal processing, Textile machinery, General industry, Petrochemical, etc.

During bending, the cohesion was found to be good enough for the cracks to traverse splats, linking thermal cracks, rather than following the splat boundaries. The absence of any notable, influence of the coating particle size on the critical strain can thus be explained by the large number of thermal cracks that are generated irrespective of the powder size used. Different coating materials, however, resist thermal cracking differently. This is believed to be the main reason for the differences in critical strains.

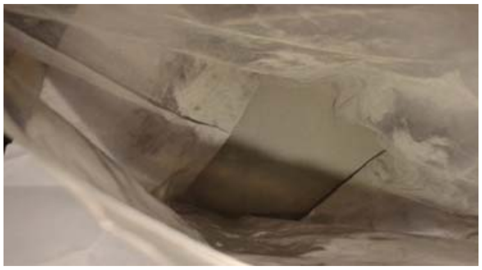

Fig.1 Inconel-718 Powder

Fig.2 Mild Steel substrate

Inconel-718 is a precipitation hardenable nickel-chromium alloy containing significant amounts of iron, niobium, and molybdenum along with lesser amounts of aluminum and titanium. A substrate material of Dimension 100*150*1.75 mm for coatings is manufactured from 12% Cr Mild Steel.

II. Methodology

Grit Blasting Process;

Abrasive grit blasting is the process by which an abrasive media is accelerated through a blasting nozzle by means of compressed air. The grit blasting process is used to prepare all the samples for thermal spraying to achieve good bond between the coating and the substrate. The substrate namely Mild Steel (MS) have been grit blasted using the Alumina abrasives of particle size 80 microns using the grit blasting machine shown in fig.3. Compressed air of pressure 10 bar was used for all the blasting operations to obtain the desired roughness of the surfaces suitable for HVOF process.

Fig.4 Grit blasted sample surface

High velocity oxy-fuel thermal spraying process

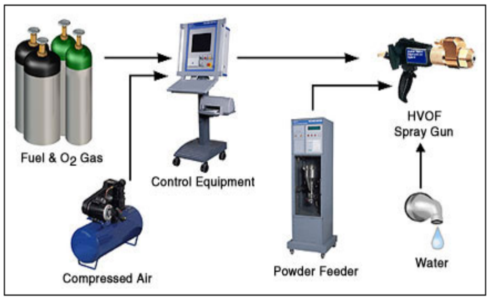

Fig.5 Key components of HVOF spray system

HVOF COATING PROCEDURE;

The HVOF setup installed is shown in fig. The setup consists of gas cylinders, nozzle system, 10HP compressor and control panel. Before the spray process the following safety checks are followed.

- ✓ Check for gas leakages.
- ✓ Check for gas flow through the nozzle using the manual operation mode in the control panel.
- ✓ Ensure no clogging of nozzles.
- ✓ Ensure powder filling before powder carrier gas namely nitrogen is released into the powder unit.

✓ Water levels in the vaporizing unit to be monitored and refilled if necessary before starting the spray processing.

✓ Ensure the temperature of the vaporizing is at 70^0C before starting the spray processing.

✓ Check the levels of oxygen, nitrogen and LPG fuel before starting the spray process.

Inconel-718 powders were sprayed onto the grit blasted MS substrates a standoff distance of 40cm was maintained for all coating trials of samples. All the coating trials have been conducted using the following optimized process parameters. Thermal spraying parameter details as shown in table 1.

Table 1. Thermal spraying parameters

Oxygen Pr. (kPa)	Fuel pr. (kPa)	Air pr. (kPa)	Powder feed rate (m3/h)	Spray rate (kg/h)	Spray distance (m)
1030	600	715	0.78	6.25	0.27

Fig.6 HVOF Spraying Process

Fig.7 HVOF Coated Sample

MODEL PREPARATION;

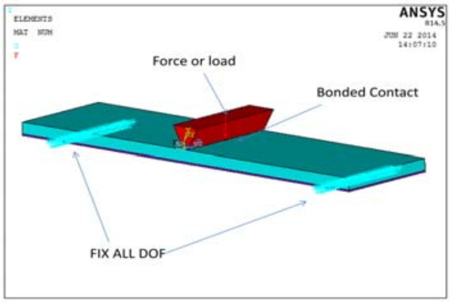

Fig.8 Experimental & Analytical Model

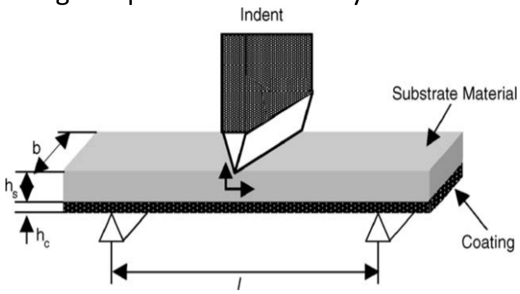

Fig.9 Geometric configuration of the Specimen

Table 2. Geometric configuration values of the Specimen

l (mm)	b (mm)	h_s (mm)	h_c (mm)	P in (N)
44	150	1.75	0.25, 0.5, 1	2000, 3000, 4000

Bend tests were performed according to ASTM Standard Method E 290-77 with a guided-bed jig as described in ASTM Standard Method E 190-64.

III. RESULTS AND DISCUSSION

Below Fig.10 & Fig.11 Shows FEM analysis & XRD of INCONEL-718 powder.

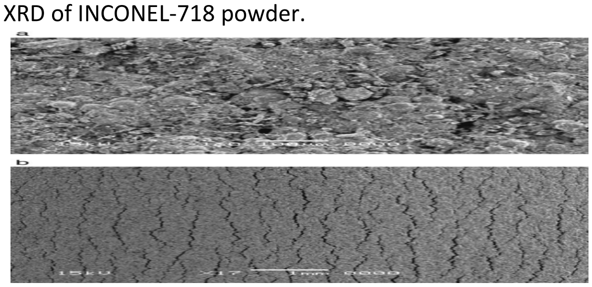

(a) Before Bending (b) After Bending

Fig.10 Sem Images of Inconel-718 powder

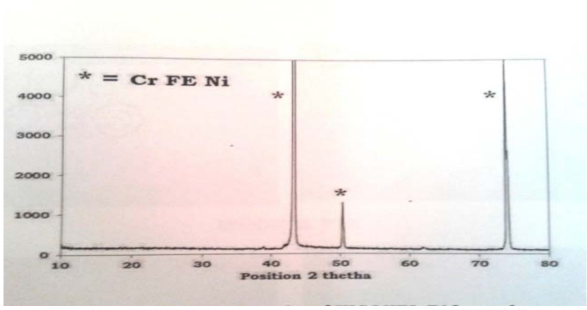

Fig.11 Showing XRD peaks of INCONEL-718

The SEM micro-photographs of the developed Inconel-718 coatings on Mild Steel Substrates are shown in Fig.10. Its confirming the presence of materials such as Ni,Co,Fe,Cr there by confirming Inconel Matrix.

With reference to Fig.11 at about 40-45, 50-53 & 70-73 angle of degrees the Cr, Fe & Ni particles present in Inconel-718 powder rises from the pattern shows maximum height value representing their presence, remaining values shows the presence of other particles of Inconel-718 powder in X-Ray Diffraction patterns.

BENDING STRESS VALUES

Table 3 shows the Experimental and Table 4 shows the Analytical results.

Table 3. EXPERIMENTAL

Coating Thickness	Load	Load	Load
	2000 N	3000 N	4000 N
Without	287.35 Mpa	431.03 Mpa	574.71 Mpa
0.25 mm	221.34 Mpa	334.12 Mpa	445.14 Mpa
0.5 mm	173.83 Mpa	260.74 Mpa	347.66 Mpa
1 mm	116.36 Mpa	174.54 Mpa	232.72 Mpa

Table 4. ANALYTICAL

Coating Thickness	Load	Load	Load
	2000 N	3000 N	4000 N
Without	306.87 Mpa	448.23 Mpa	591.35 Mpa
0.25 mm	238.26 Mpa	357.05 Mpa	475.66 Mpa
0.5 mm	192.56 Mpa	288.59 Mpa	384.50 Mpa
1 mm	133.12 Mpa	199.41 Mpa	265.43 Mpa

Below Fig.12 and Fig.13 gives Crack initiation Crack initiation after bend test Bended samples.

Fig.12 Crack initiation after Bend test

Fig.13 Bended sample

As the coating thickness is increasing its Bend deflection is decreasing and if no coating means its deflection is maximum. Due to bending stress the sample get initiation of crack at the point of contact and if stresses are exceeding means the crack propagates and sample will gets failure in the form of Ductile fracture.

Below Fig.14 Shows Ansys result for 0.25mm thickness at 2000N load condition

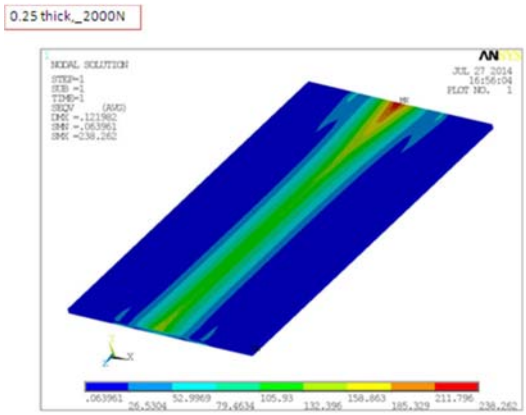

Fig.14 Von-Mises stress distribution

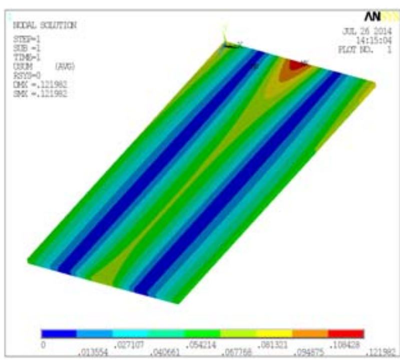

Fig.15 Displacement Plot

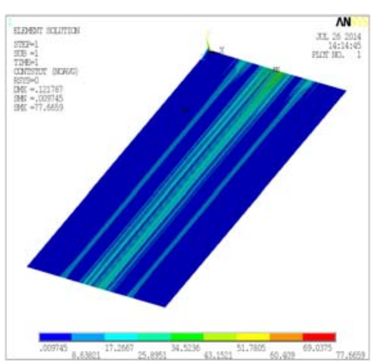

Fig.16 Contour Plot

The below plot shows Bending stress v/s Load for 0.25mm coating thickness as shown in fig.17

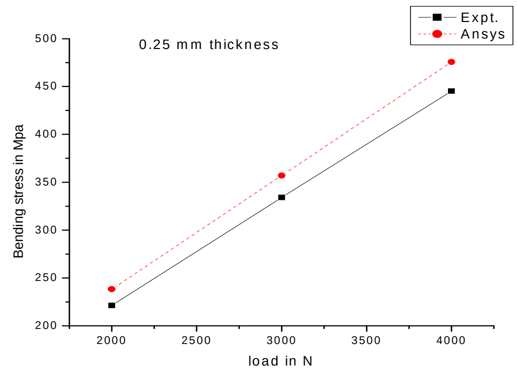

Fig.17 Graph of Bending stress v/s load for 0.25mm coating thickness

As 250 μ thickness of Inconel-718 is coated MS sample its Bending stress value increasing gradually. Experimental and Ansys values approach each other by slight variation of errors.

The below plot Shows graph of Bending stress v/s Thickness for 2000N Load as shown in fig.18

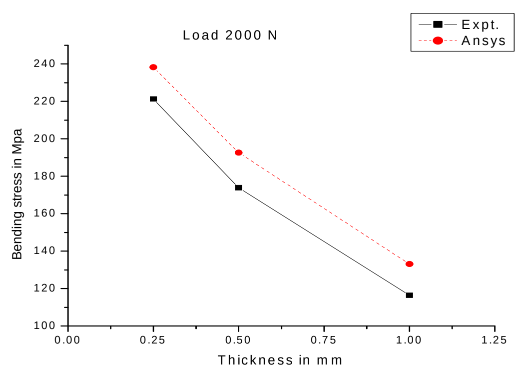

Fig.18 Graph of Bending stress v/s Thickness for 2000N load

As the Thickness is increasing means its Bending stress value is decreasing for the load of 2000 N is applied. Experimental and Ansys values approach each other by slight variation of errors.

IV. CONCLUSION

The following conclusions were arrived from analysis and experimental results for Bending Stresses on coating materials.

- Inconel-718 Powder has been successfully coated on Mild Steel substrate by HVOF process.
- It was found that coated samples gives less bending stress value than that of uncoated sample showing that increasing of its strength to resist to bending load.
- As the coating thickness increases its resistance to Bending increases gradually.
- As the load increases with constant thickness, its Bending stress also increasing significantly.
- As the Thickness of coating increases with constant Loading conditions, its bending stress also decreasing significantly.
- Experimental and analytical values are matching with small variations.

REFERENCES

1. A.F.M. Arif et.al., "Three-point bend testing of HVOF Inconel 625 coating: FEM simulation and experimental investigation" journal of Surface & Coatings Technology, P.no. 1873-1879, (2006).

2. Carolin Pfeiffer et al., "Miniaturized bend tests on partially stabilized EB-PVD ZrO2 thermal barrier coatings" journal of Surface & Coatings Technolog, P.no. 3245–3250, (2010).

3. C.S. Ramesh et al., "Influence of forging on mechanical properties of Ni–P coated Si3N4 reinforced Al6061 composites" journal of Materials Science and Engineering a 551 P.no. 59– 66, (2012).

4. Y.C. Zhou et al., "Fracture characteristics of thermal barrier coatings after tensile and bending tests" journal of Surface and Coatings Technology 157 P. no.118–127, (2002) .

5. Y. Yamazaki et al., "The determination of the delamination resistance in thermal barrier coating system by four-point bending tests" journal of Surface & Coatings Technology 201 P. no.744–754, (2006).

6. Lalitha.R et al., "Interfacial strength of laser surface engineered TiC coating on 6061 Al using four-point bend test" journal of Materials Science and Engineering A289, P. no.34–40, (2000).

7. P. V. Jadhav et al., carried work on "Effect of surface roughness on fatigue life of machined component of Inconel 718", (2003).

8. N. Ahmed et al., " The effects of microstructural features on the performance gap in corrosion resistance between bulk and HVOF sprayed Inconel 625", (2010).

FORMATION OF MECHANICAL AND TRIBOLOGICAL PROPERTIES OF AL-6061 BASED METAL MATRIX COMPOSITES WITH WATER QUENCHING

Mr.Harisha.CV[1] ,Mr.Shenoy .HG[2], Dr.N.G.S Udupa[3]
M.Tech (machine design) student, Nagarjuna College of Engineering and Technology,
Associate Professor, Dept, of Mechanical Engineering,
RLJIT, Doddaballapur, Bangalore ,India,
Vice-Principal and Head of Mechanical(PG)
Nagarjuna College of Engineering and Technology Bangalore ,India.
Email: harisha.cv1989@gmail.com, HGshenoy2005@yahoo.co.in, ngsudupa@gmail.com.

Abstract— Aluminum matrix composites (AMCs) reinforced with AL_2O_3 Powder particles are being used for high performance applications such as automotive, aerospace, military and electrical industries because of their improved physical and mechanical properties. In this research, Al2o3 and E-glass fibers particles are synthesized by Solution Combustion Synthesis process. The Al-6061 Aluminum alloy weight was constant at 1.5kg. Reinforcements are 1.0, 2.0 and 3.0weight percentages of the synthesized particles, through Stir Casting Technique. The composites were then characterized by three tests tensile wear and hardness. The tests were carried out for varying weight percentage ratios of the reinforcement at varying Solution Heat Treatment temperatures of T6 and T86 conditions. The T6 is 480ºC and 3hour heating all specimens. After heating, we quench the specimens for 5sec, using water. The T86 is for ageing of each 10 specimens using woven in that 175 º C heat they left in 6hours.The hardness and tensile were tests carried out for varying weight percentage ratios of the reinforcements with different ageing. Wear tests were carried out for varying weight percentage ratios of the reinforcements with constant Conditions of Speed, Load and Time. The proto type of tensile specimen created with the suitable dimensions using CATIA V5 R17 software. The geometrical of model specimens and its components are converted from physical domain into computational domain using discretizing the model using HYPERMESH 10 software. To create a different cell zones to apply boundary condition. The results reveal that the Hybrid Metal Matrix Composite (HMMC)'s containing 2.0 weight percentage particle reinforcement has improved mechanical properties.

Index Terms— Al-6061, Al2O3, Analysis, E-glass, Hardness, T6, T86 (conditions), Tensile, & wear.

I. INTRODUCTION

Aluminum is a relatively soft, durable, light weight, ductile and malleable metal with appearance ranging from silverative dull gray depending on the surface roughness. It makes up about 8% by weight of the earth's solid surfaces. It is a silvery white member of the boron group of chemical elements. It as the symbol Al and its atomic number is 13. It's not soluble in water under normal circumstances. Aluminium is the third most abundant element in the Earth's crust and constitutes 7.3% by mass. In nature however it only exists in very stable combinations with other materials (Particularly as silicates and oxides) and it was not until1808 that its existence was first established. It took many years of painstaking research to "unlock" the metal from its ore and many more to produce a viable, commercial production process.

Fig 1: Aluminium Metal

Fig 1 shows Pure aluminium is a silvery-white metal with many desirable characteristics. It is light, nontoxic (as the metal), nonmagnetic and no sparking Aluminium is the third most abundant element in the earth's crust, which contains 8% aluminium. It is a constituent of most rocks and in the form of aluminium silicate it is an important source of clays commercially, the most important source of the metal is bauxite which contains 52% Al_2o_3, 27.5% Fe_20_3 and 20.5% H_20. Bauxite is treated with caustic soda and claimed at 1200° produce high purity alumina. The alumina is then smelted electrolytic cell to produce pure aluminium. It is decorative and it is easily formed, machined, and cast. Alloys with small amounts of copper, magnesium, silicon, manganese, and other elements have very useful properties.

2. MATERIAL SELECTION

1.ALUMINUM ALLOY AL-6061, 2.AL_2O_3 POWDER, 3.E-GLASS FIBER

BASE MATRIX MATERIAL (AL6061)

Fig 2: Al-6061 Ingots

Fig 2 shows Base matrix material constitutes major part of the composite material. Matrix phase supports the fibers (reinforcing material) and keep them in their position, transfers the load to strong fibers, protects the fibers from damage and prevents cracks initiated at fiber from propagating. Electrical properties, chemical properties and elevated temp behavior of the composite depend on the matrix material in table 1and table 2.

Table 1: Chemical Composition Of Al-6061

SL	Silicon	Iron	Copper	Manganese	Magnesium	Chromium	Zinc	Titanium
Max	0.8%	0.7%	0.40%	0.15%	1.2%	0.35%	0.25%	0.15%
Mini	0.4%	NO	0.15%	NO	0.8%	0.04%	NO	NO

Table 2: Physical Properties

Density (g/cc)	Poisson's Ratio	Elastic Modulus (GPa)	Tensile Strength (Mpa)	Yield Strength (Mpa)	Elongation	Hardness (HB 500)	Shear Strength (MPa)	Fatigue Strength (MPa)
2.70	0.33	70 – 80	125	55	25-30%	47	125	90

REINFORCEING MATERIAL

The Foreign matter in the form of particulate fiber or ceramids which are introduced into base matrices material, to obtain a new material with improved strength and hardness. These foreign matters are known as Reinforcing Materials. Example: Mica, E-glass, Fly ash, AL_2O_3 ………etc.

AL_2O_3 powder

Fig 3: AL_2O_3 Powder

Fig 3 shows AL_2O_3 is widely distributed and occurs in igneous, metamorphic and sedimentary regimes. Large crystals of AL_2O_3 used for various applications are typically mined from granitic pegmatite's.AL_2O_3 is a clear transparent material (Aluminosilicate) with a high dielectric strength, can withstand a constant temperature of 550°C, and a melting point of approximately 2250°C.

COMPOSITIONS

AL_2O_3 IS the typical nominal composition of Ca -1.6%,Co-0.8%,Fe-0.2%,Na<300&Si-3.5%. the melting points is 2200^0C and density 3.6g/cc . It is soluble at water≤.2%,PH value (10%aqueous suspension) =6.8-7.8.

PROPERTIES AND USES

AL_2O_3 has a high dielectric strength and excellent chemical stability, making it a favored material for manufacturing capacitors for radio frequency applications. It has also been used as an insulator in high voltage electrical equipment. It is also birefringent and is commonly used to make quarter and half wave plates. Because Al_2O_3 is resistant to heat it is used instead of glass in windows for stoves and kerosene heaters. The idea is to keep the metal conductors from fusing in order to prevent a short-circuit so that the cables remain operational during a fire, which can be important for applications such as emergency lighting.

Illites or clay AL_2O_3s have a low caution exchange capacity for 2:1 clays. K+ ions between layers of AL_2O_3 prevent swelling by blocking water molecules. Because AL_2O_3 can be pressed into a thin film, it is often used on Geiger-Müller tubes to detect low penetrating Alpha particles.

E-GLASS

Fig 4: Shows E-Glass Short Fibers

Fig 4 shows E-Glass or electrical grade glass was originally developed for standoff insulators for electrical wiring. It was later found to have excellent fiber forming capabilities and is now used almost exclusively as the reinforcing phase in the material commonly known as fiberglass.

COMPOSITION

E-Glass is a low alkali glass with a typical nominal composition of SiO_2 54wt%, AL_2O_3 14wt%, CaO+MgO 22wt%, B_2O_3 10wt% and Na_2O+K_2O less than 2wt%. Some other materials may also be present at impurity levels.

3. EXPERIMENTAL PROCEDURE

An Electric Arc Furnace is a furnace (fig 5) that heats charged material by means of an electric arc. Arc furnaces range in size from small units of approximately one ton capacity up to about 400 ton units used for secondary steel making. Arc furnaces used in research laboratories and by dentist may have a capacity of only a few dozen grounds. Ingots of Al-6061 are pre-heated so as to remove the oil content and other contents which are slicked to the surface of the ingots. After pre-heating the ingots are added into the furnace for melting. The ingots are heated in the furnace up to their melting point about750 C. Reinforcing materials Al_2O_3 and e-glass of required composition are added to the molten metal to obtain a required composite. Degasser (fig 6) is added at the right time and temperature before reinforcement is added.

Fig 5: Mechanical Stirring

Fig 6: De-Gasser

Two halves of a mold is joined, and liquid metal is poured into the mold through a hole in the top. The metal is allowed to cool, and casting is struck by separating the two halves of the mold. Table 3 shows ratio of reinforcement and matrix material is added in the furnace.

Table 3: Shows Ratio of Reinforcement and Matrix Material (Weight In %)

Sl no	% Al_2O_3	% E-glass	% Al-6061
A0	0(0gms)	0(0gms)	100(1.5kg)
A1	1(15gms)	1(15gms)	98
A2	1(15gms)	2(30gms)	97
A3	1(15gms)	3(45gms)	96
A4	2(30gms)	1(15gms)	97
A5	2(30gms)	2(30gms)	96
A6	2(30gms)	3(45gms)	95
A7	3(45gms)	1(15gms)	96
A8	3(45gms)	2(30gms)	95
A9	3(45gms)	3(45gms)	94

MACHINING

It is process carried out after the casting process is completed; it is used to remove the excess material from the test bar. Machining(fig 7) is the process of removal of excess of material from the work, which is carried out in order to get down the casted specimen to the required specifications by making use of lathe.

Fig 7: Machining process.

HEAT TREATMENT

The procedure for heat treatment involves the following steps

Solutionizing , Quenching and Two-step aging

1. First step at lower temperature
2. Second step at higher temperature

Solution heat treatment

A treatment in which an alloy is heated to a suitable temperature and held at this temperature for a sufficient length of time to allow a desired constituent to enter into solid solution, followed by rapid cooling to hold the constituent in solution. The material is then in a supersaturated, unstable state, and May subsequently exhibit Age Hardening.

Quenching

Rapid cooling of hot metal by sudden dipping of the metal into selected fluid medium is known as quenching.

Aging

It is the change in the mechanical physical and chemical properties of metals and alloys resulting from the lack of thermodynamic equilibrium in the original state and the gradual approach of the structure to the equilibrium state under conditions that permit a sufficient diffusion rate for the atoms.

Fig 8: The Muffle Furnace

Single aging: This step is carried out at a temperature of 480 ±5°C for a period of 3hrs.

After 3hrs quench the specimens in water, dipped in each 5sec is carried out (fig 8) furnace

Double aging: After the first step aging, second step aging is carried out at 175 ±5°C for period of 6 hrs.

4. RESULTS AND DISCUSSION

BRINELL HARDNESS TESTING

Hardness is the measure of the resistance of a metal to permanent (plastic) deformation. The hardness of a metal is measured by forcing an indenter into its surface. The indenter material, it is usually a ball, pyramid, or cone, is made of a material much harder than the material being tested. After the indentation has been made, the indenter is withdrawn from the surface. An empirical hardness number is then calculated or read off a dial (or digital display), which is based on the cross sectional area or depth of impression.

Table 4: Brinell Hardness Values For Different Composition

Samples	Single aged(BHN)	Double aged (BHN)
Plain	87	86
A1	89	88
A2	91	92
A3	94	95
A4	92	93
A5	89	87
A6	87	85
A7	90	79
A8	82	76
A9	78	74

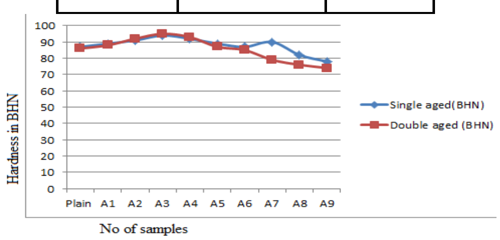

Fig 9: Hardness Number (BHN) V/S Number of Samples Tha table 4 is BHN values fig 9 show that BHN v/s sample numbers for plain (A3) AL-6061 Aluminum alloy is greater value of 95 at double aging. The A4(1% e-glass &2% Al_2O_3) both are the almost same value of 93 single and double ageing at 480^{0}C & 175^{0}C.

WEAR TEST

Wear can also be defined as a process where interaction between two surfaces or bounding faces of solids within the working environment results in dimensional loss of one solid, with or without any actual decoupling and loss of material.

Table 5: Volumetric Wear Rate (µg/m) For Single And Double Ageing

Samples	Single ageing	Double ageing
A0	0.53051	0.59577
A1	0.52046	0.53051
A2	0.51030	0.26525
A3	0.39788	0.25524
A4	0.38781	0.24523
A5	0.26525	0.23521
A6	0.25512	0.22331
A7	0.24509	0.13263
A8	0.23495	0.12252
A9	0.22490	0.11241

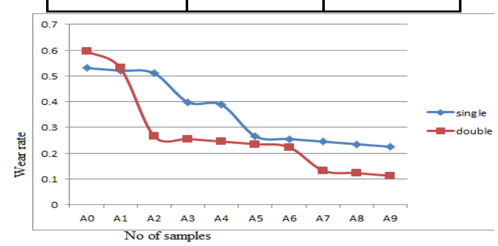

Fig 10: Specific Wear Rate V/S Number of Samples

Table 5 Volumetric Wear Rate, The above fig 10 is clear shows that double aged specimens have lesser wear rate compared to that of single aged specimens. "Composition of, 3%Al_2O_3 and 3% E-glass is better in the lot, gives the minimum volumetric wear rate.

TENSILE TEST

Tensile testing, also known as tension testing is a fundamental materials science test in which a sample is subjected to uniaxial tension until failure. Properties that are directly measured via a tensile test are ultimate tensile strength, maximum elongation and reduction in area.

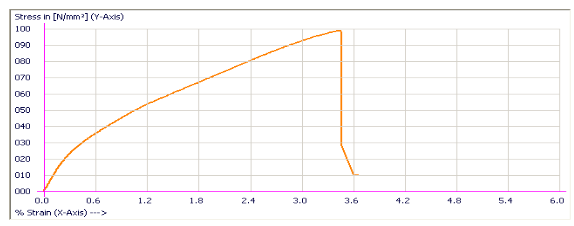

Fig 11: Stress (N/Mm^2) V/S Strain

Fig 11 shows the effect of aging on the ultimate tensile strength of 2% AL2O3 and 1% E-glass fiber metal- matrix composite it has been reported that the addition of reinforcement to aluminium alloys improves the yield strength and the UTS of the composite where as the strain to failure decreases as the weight percentage of reinforcement increase.

Table 6: Ultimate Tensile Strength for Single and Double Ageing

Samples	Single aged(mpa)	Double aged(mpa)
Plain	100.56	95.62
A1	112.87	103.3
A2	133.04	103.72
A3	146.55	121.86
A4	110.78	98.56
A5	106.37	101.61
A6	110.56	103.1
A7	116.29	106.88
A8	126.18	107.58
A9	117.23	105.76

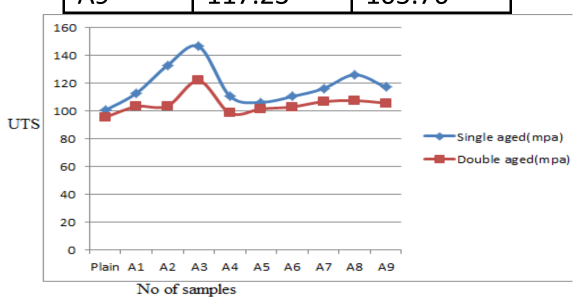

Fig 12: Ultimate Stress V/S Number of Samples

Table 6 is practical results & from the Fig 12.In that increase in percentage of Al_2O_3 composition in aluminum hybrid composite fetches little increase in Ultimate Stress as compared to percentage increase of E-glass composition which gives better Ultimate Stress to the composite.

From the Fig 12 it is very clear shows that single aged specimens have better Ultimate Stress as compared to that of double aged specimens for the A3 composition of single aged specimen gives the maximum value "Composition of 1% Al_2O_3 and 3% E-glass is better in the lot, as it gives the maximum value".

TENSILE ANALYTICAL RESULTS

Table 7: Nodal Solution of Ultimate Tensile Stress for Single and Double Ageing

Samples	Single aged in Mpa	Double aged in Mpa
Plain	102.85	98.14
A1	120.12	100.36
A2	125.12	110.48
A3	139.15	128.34
A4	129.56	117.45
A5	123.57	117.15
A6	123.17	109.19
A7	124.75	114.16
A8	130.73	115.19
A9	119.12	110.42

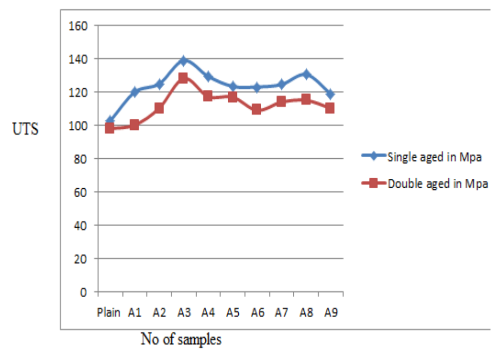

Fig 13: Ultimate Stress V/S Number Of Samples

Table 7 analytical results are plots in Fig 13, initially Ultimate Stress was low for 1% of E-glass composition and as gradually E-glass composition is increased the Ultimate Stress also increased. From the Fig 13 it is very clear that single aged specimens have better Ultimate Stress as compared to that of double aged specimens for the A3 composition of single aged specimen gives the max value

COMPRESSION OF PRACTICAL AND ANALYTICAL RESULTS

Table 8: Nodal Solution of Ultimate Tensile Stresses

Samples	P1 Single aged(mpa)	P2 Double aged(mpa)	a1 Single aged Mpa	a2 Double aged Mpa
Plain	100.56	95.62	102.85	98.14
A1	112.87	103.3	120.12	100.36
A2	133.04	103.72	125.12	110.48
A3	146.55	121.86	139.15	128.34
A4	110.78	98.56	129.56	117.45
A5	106.37	101.61	123.57	117.15
A6	110.56	103.1	123.17	109.19
A7	116.29	106.88	124.75	114.16
A8	126.18	107.58	130.73	115.19
A9	117.23	105.76	119.12	110.42

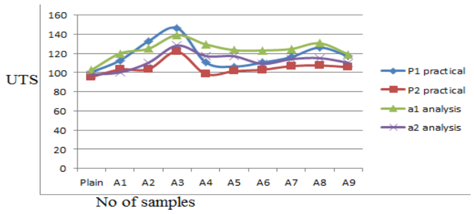

Fig 14: Ultimate Stress V/S Number of Samples

Table 8 is practical and analytical results, & from the Fig 14. It is very clear that analytical results have better Ultimate Stress as compared to that of practical results. Practical results are over laps to the analytical results but analytical results are not over laps. The A3 is the maximum value "Composition of 1% Al_2O_3 and 3% E-glass is better in the lot, as it gives the maximum value".

5. CONCLUSION

- The tests were carried out for varying weight percentage ratios of the reinforcement at varying Solution Heat Treatment temperatures of T6 and T86 conditions. The T6 is 480ºC and 3hour heating all specimens. After heating we quench the specimens each in 5sec, using the water.
- The T86 is ageing of each 10 specimens using woven in that 175 º C heat they left in 6hours.The hardness and tensile tests were carried out for varying weight percentage ratios of the reinforcements with different ageing. Wear tests were carried out for varying weight percentage ratios of the reinforcements with constant Conditions of Speed, Load and Time.
- The harness have concluded that its clear shows double aged specimens have better hardness as compared to that of single aged specimens for the A3 composition of double aged specimen gives the maximum hardness value further addition of reinforcement shows that there is no increase in the hardness and remains stable. "Composition of 1% Al_2O_3 and 3% E-glass is better in the lot, as it gives the maximum hardness value".
- They also tensile results are Ultimate Stress as compared to percentage increase of E-glass composition which gives better Ultimate Stress to the composite. From the Figs it is very clear that single aged specimens have better Ultimate Stress as compared to that of double aged specimens. Same A3 composition of single aged specimen gives the maximum value. And also analytical and practical results are same.
- The Volumetric wear rate of specimens with respect to different E-glass and Al_2O_3 composition in aluminum metal matrix composite, have initially wear rate is high for 1% of E-glass and 1% Al_2O_3 composition and has gradually E-glass composition is increased wear rate also decreases.
- From the Fig it is also clear that double aged specimens have lesser wear rate compared to that of single aged specimens. "Composition of, 3%Al_2O_3 and 3% E-glass is better in the lot, gives the minimum volumetric wear rate.

REFERENCE

1) AGARWAL. B.D AND LAWRENCE J-BBROUTMAN. "Analysis and performance of fiber composite ". Publication by john Wiley and sons, inc vol, 2, PP 223-264 ,2012

2) G.B. Veeresh Kumar "Investigated the experimental results of the studies conducted regarding hardness, tensile strength and wear resistance properties of Al6061-SiC and Al7075-Al2O3 composites".vol,7 PP.221-250, 2011.

3) C.C poe, jr- "simulated impact damage in a thick Figite /epoxy laminate using spherical indenters". Vol,1 PP334-343,.2009

4) Button, S.T."Numerical simulation of hydrodynamic lubrication in cold extrusion", XXII CILAMCE, Anais do Congresso, CDROM, Campinas.vol,9,PP 562-569, 2001

5) Chin R.K. and Steif P.S., 1995, "A computational study of strain in homogeneity in wire drawing", Int. J. of Machine Tools & Manufacture, vol. 35 (8), pp. 1087-1098,2010

6) H.C. Anilkumar "The results of an experimental investigation of the mechanical properties of fly ash reinforced aluminium alloy (Al 6061) composites samples, processed by stir casting". PP.55-66, 2012.

7) Dixit U.S. and Dixit P.M., 1999, "An analysis of the steady-state wire drawing of strain-hardening materials", J. of Mat. Proc. Tech., vol 47 (3-4), pp. 201 – 229.

8) E.M. Rubio, "Analytical methods application to the study of tube drawing processes with fixed conical inner plug" slab and upper bound methods Proc. of the Int. Scientific Conference on CAM'3S, L.A. Dobrzanski, Gliwice-Zakopane (Poland), 2005, pp. 841–850.

9) Arunkumar"Studies on Dry Sliding Wear Behavior of Hybrid Composites" Department of Mechanical Engineering, Sathyabama University, Chennai. Tamilnadu, India. PP.46-49 ,2010

10) Amal NassaR & Amal NassaR "Tensile Behaviors Of Aluminum Matrix CompositesIn Extrusion Simulation Experiments". Department of Mechanical Engineering Higher Technological Institute Tenth of Ramadan City, Egypt.2nd International Conference on Advances in Computational Tools for Engineering Applications (ACTEA) 2012 PP.296-300,

DESIGN AND DEVELOPMENT OF CLAMPING UNIT IN SCREW-LESS ELECTRICAL TERMINAL BLOCKS

[1]Mr.Arjun C A, [2]Dr.N.G.S.Udupa , [3]Dr.Gurumoorthy. B
[1]PG Student, Nagarjuna college of engineering and technology, Bangalore
[2]Professor & HOD, Nagarjuna college of engineering and technology, Bangalore
[3]Professor, Indian institute of Science, Bangalore
Email: [1]arjungowda.ca@gmail.com, [2]ngsudupa@gmail.com, [3]bgm@mecheng.iisc.ernet.in

Abstract— A terminal for detachably connecting an electrical lead connector pin to an electrical circuit is disclosed. The terminal includes an end contact and a movable clamp for movement between first and second positions relative to the end contact. The clamp has a pocket at one end which a relative motion to and fro due to force applied by the tilting action of the screw driver. The pocket receives an electrical lead into the pocket when a force is applied using screw driver, as the screw driver is removed, the clamp moves to its original position which locks the electrical lead to a end contact. As a huge amount of force is required to give a relative motion to the clamp by the screwdriver, the design is bought under modifications.

Index Terms—, Cage Clamp, Clamping force, Screw-less terminal blocks, S-Clamp, Conductor.

I. INTRODUCTION

In today's market, most companies redesign to create new products. Redesign improves product quality and reduces cycle time. However, most techniques limit innovation. They modify a single reference product, which closely matches user needs, and only introduce new products when major conflicts exist between user needs and existing products. This study introduces a new redesign for product innovation approach. The approach combines two or more distinct reference designs into a single new product. The process creates design conflicts. The induced conflicts stimulate innovation. which improves solution quality and reduces cycle time.

After products are on the market for some time, they often need to be redesigned. There are many reasons for redesigning products. First, design faults may be found, or customers may change requirements. Products may also be redesigned to improve quality, reduce costs, extend product life, or reduce environmental impacts. As a result, redesign is an important part of the product development process. In fact, in today's market, most new products are also developed using redesign techniques. New products are generally derived from similar products Therefore; new product design is generally a derivative work, which consists of changing prior designs to make them suitable for new applications.

In fact, more than 75% of all engineering design activity involves reusing prior design knowledge to solve new design problems there are many advantages through using a redesign approach to develop new products. Redesign generally improves the quality and efficiency of the product. Design process Redesign solutions are generally more feasible and reliable, since they have already been used successfully in prior products Reusing prior design information also reduces product costs, required design resources and cycle time.

Therefore, redesign is an important key to business success However; current redesign techniques can also limit product innovation. Redesign generally focuses on resolving conflicts between current product needs and prior design capabilities. Most techniques start by choosing a reference design that reduces conflicts between user needs and product functions, as much as possible. Remaining conflicts, depending upon their degree, are resolved by changing component attributes, replacing components, or changing the structure of the original design.

Fig (1). Shows *Screw-less terminal Blocks* which are constructed employing good engineering practices. As the name suggests this type of terminals blocks does not require a screw for termination of a conductor within the clamping unit. In case of screw clamp connections, it is necessary to ensure proper tightening of screw with a torque screwdriver. In screw-less terminal blocks cage clamp is opened by insertion of a screwdriver. Conductor is inserted into this “opened” clamp and connection is secured as soon as the screwdriver is withdrawn.

The clamping force in cage clamp connection adjusts automatically according to cross-section of the conductor inserted as shown in Fig(2). Larger the conductor, more the force exerted on it. There are no external factors which can change this force.

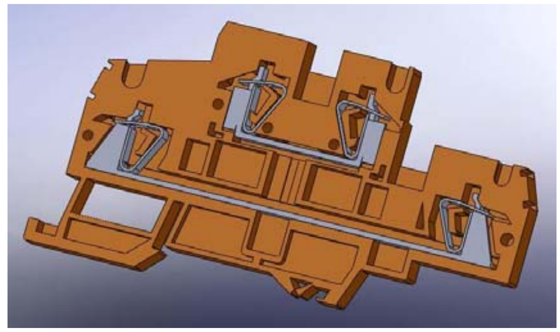

“Fig (1). Screw-less terminal blocks”

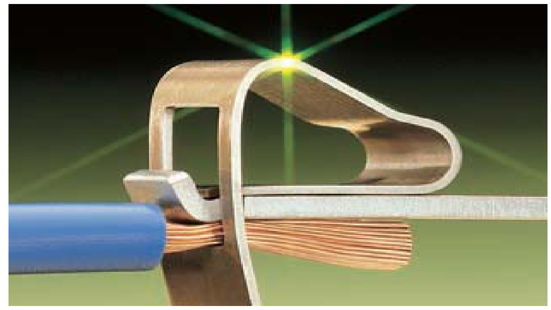

“Fig (2). The cage clamp, end contact & conductor”

This newly developed *cage clamp* system functions in a similar way to the proven clamping yoke. Separation between the mechanical and electrical functions has also been maintained with the tension clamp version. The tension clamp made of high-quality, non-rusting and acid resistant steel draws the conductor towards the electroplated copper current bar. Minimal contact resistance and high corrosion resistance is achieved by the tin-lead surface and permanently maintained by the compensating action of the tension spring. The following Fig (3) show steps to insert the electrical conductor in to the cage clamp.

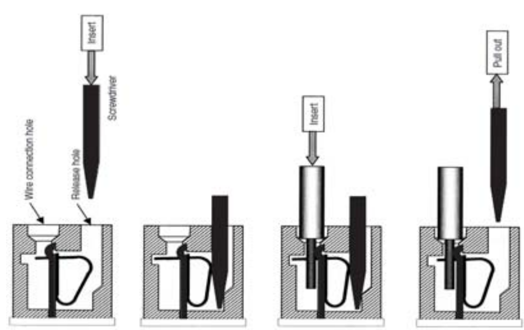

“Fig (3). Steps to insert conductor into cage clamp”

II. PROBLEM DEFINITION

In *Screw-less terminal blocks* cage clamp is opened by insertion and slight tilting action of a screw driver. Conductor is inserted into this "opened" clamp and connection is secured as soon as the screw driver is withdrawn. As the clamp does not open due to the insertion of screw driver, a slight tilting action requires a huge force.

Fig (4). Describes the method to insert the conductor which depends on the tilting action of screwdriver. If lubricating liquid, such as oil, is present on the tip of screwdriver, the screwdriver may fall out resulting in injury to the operator. Insert the screwdriver into the bottom of the hole. It may not be possible to connect cables properly if the screwdriver is inserted incorrectly. Sometimes due to improper insertion, the plastic body, rail supports, supporting walls may get damaged or the clamp insert may come outside from the body as the huge force is applied by the screw driver.

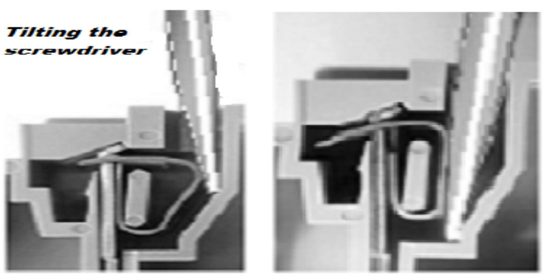

"Fig (4). Tilting action of screwdriver"

III. SCOPE OF PROJECT

The primary objective of the work is to design a new clamp for holding the wire with necessary contact pressure with reduced clamping force. Reducing the cycle time and forces on the operator is also an objective of the project.

The following points briefly discuses the scope of the project.

- ✓ Studies of geometry of the component in order to generate the design concepts to achieve the primary objective.
- ✓ Number of concepts has been generated by considering different reference surfaces in order to design of clamping unit.
- ✓ Modeling of the different concepts using solid works software and selecting the best concept using concept selection process.
- ✓ Detail designing of every component in the part. And finally assembled to check the clearances, mechanical properties.
- ✓ The load required to clamp should be minimum; therefore the analysis of the clamp is required.

III. METHODOLOGY

Methodology is the systematic step-by-step planning approach in designing an clamping unit in screw-less terminal block. It includes the activity of finding solutions to technical problems by applying insights from natural and engineering sciences, at the same time taking into account the conditions and constraints of a given task. It includes the following steps in general which is shown in fig (5).

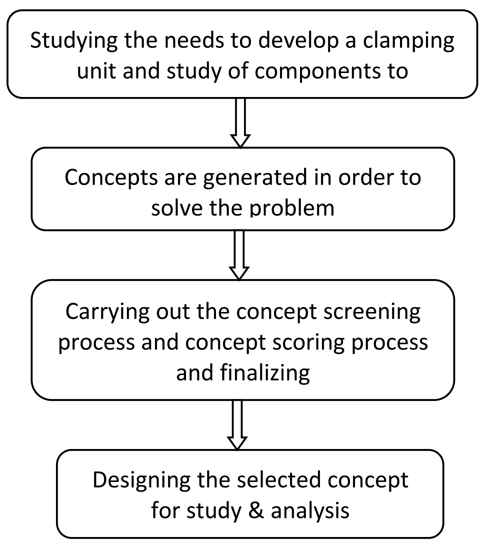

"Fig (5) Flow chart of methodology"

A. Identifying the Requirements to Design

The process of identifying needs and collecting the data is an integral part of the design and product development process and is most closely related to concept generation and concept selection. Needs are largely independent of any particular product we might develop; they are not specific to the concept we eventually choose to pursue. Raw data is collected and interpreted in terms of customer needs. Then the needs are organized into a hierarchy of primary, secondary, and if necessary into tertiary needs. Relative importance of needs is established. The results and the identification process are reviewed.

The need in this project was to find a solution that would effectively hold the conductor firmly with necessary clamping force. In order to achieve these many design concepts are generated. Based on the collected data and needs different types of concepts are generated. Finally the developed concept should be such that it makes use of the selected reference and effectively holds the conductor.

The needs recognized for this project are as listed below:

- ✓ The current bar should come into the open slot provided in the clamping unit towards one end when at rest. When pushed by screw driver the slot should open and conductor will be inserted.
- ✓ A clamping unit has to be conceptualized in order to effectively arrest the conductor firmly. Such that when a weight is attached at the other end of the wire, the contact should not fail.
- ✓ The clamp material should be hard enough to withstand the force applied by the screwdriver without deforming and to transmit that force to move front and back.
- ✓ The clamp material used should be corrosion resistant, good current carrying capacity, fatigue resistance etc.

B. Concept Generation

The concept generation process begins with a set of customer needs and target specification and results in a set of product concepts from which a final selection has to be made. The most common concept generation method is known as brainstorming. The term brainstorming is frequently applied to any idea generation technique

In this study approximate concepts are generated that give a description of the technology, working principles and form of the mechanism that has to be built in order to improve the clamping force.

The concepts are expressed as sketches. Each concept is important for the designer to interpret the needs and clarify the problem. In order to clarify the problem the designer can decompose the problem for easier and better understanding and is followed by a brief textual description. In order to generate concepts the designer has to have a very brief knowledge of what and why he has to design and so it becomes very easy.

a. Push-In Connection

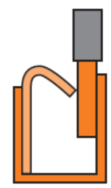

"Fig (6) PUSH-IN connection technology"

Fig (6) shows PUSH-IN connection concept, a stainless steel spring which is fitted in a separate housing, with the top end being folded towards inside slot. The pin being a stainless steel has a high elastic property it always tends to regain its original shape, taking this as a advantage the conductor can be locked firmly in slot to some extent.

In this PUSH IN connection concept only the stripped solid conductor is simply inserted into the clamping point as far as it will go. And that completes the connection. No tools are required. But the flexible conductors with crimped wire end ferrules or ultrasonic-welded conductors is difficult to insert into the slot because of small stripped wires.

b. Leaf Spring Connection

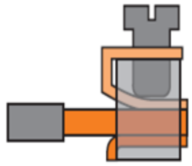

"Fig (7) Leaf spring connection technology"

Fig (7) shows the most commonly used leaf spring is the semi-elliptical leaf spring. The semi-elliptical spring may be considered as two cantilevers and elliptical spring as four cantilevers. The stress induced in a semi-elliptical leaf spring is same as that of full elliptical leaf spring. But the deflection in a semi-elliptical leaf spring is equal to one half of full elliptical leaf spring. The unloaded spring is cambered, the magnitude of the camber being such that the spring is approximately straight under the full static load. Using a screw on the top of the spring, as the screw tightens the straightness under full static load is utilized to hold the conductor firmly.

But in this leaf clamp connection system only large conductor cross-sections can be held firmly, for smallest wire cross-sections the force is insufficient.

c. S-Clip Technique

Conceptualization was carried out for clamping unit and conductor installing mechanism. For this process the input was gained after identification of needs for clamping unit and conductor mounting mechanisms.

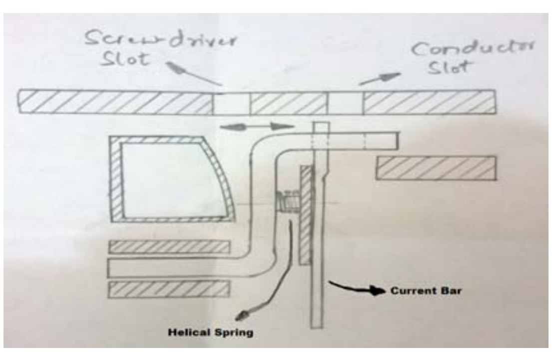

"Fig (7) The concept made by hand sketch"

Keeping all the constraints in mind such as less clamp pushing force, good conductor holding force, vibration resistant, gas-tight connection etc. the concept was developed by considering the different holding mechanisms which is discussed in the design concepts and shown in fig (7), and this design is modeled and analyzed in the later stages.

IV. MODELLING

CAD modeling is used by many designers to create elaborate computerized models of objects before they are physically produced. CAD stands for computer-aided design. Engineers, architects, and even artists utilize computers to assist in their design projects. Computers allow them to visualize their designs and confront problems before they have expended any of the resources necessary to put them into physical form. Many different professions make use of computer-aided design.

It is an important industrial art involved in automotive, aerospace and artistic designs. The use of CAD modeling is massively widespread; anything from chairs to rockets can be designed with the aid of computer programs.

At one time, this step would have involved several drafters making dozens of sketches and diagrams until a perfected model could be devised. Now, a single CAD file can be made, edited, and continually tweaked until the object is ready for production. In this section the concept which is developed with the help of design concepts, literatures, mechanisms etc has been modeled into a two- dimensional, three-dimensional drawings for better interpretation, understanding and to analyze.

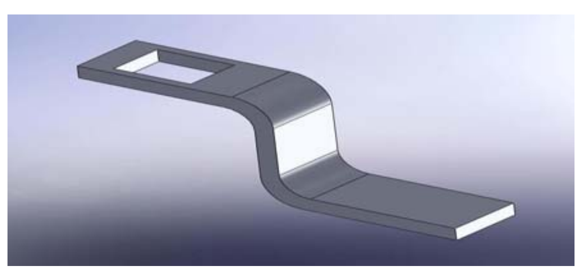

"Fig (8) The S-Clip"

Fig (8) shows the conceptual S-clamp design which has been modeled using a CAD software, Now the wire holding *cage clamp* has to be replaced with the *S-clamp*. Due to unavailability of a old model using a technique called reverse engineering, the model has been developed for the full scale with the help of measuring instruments. Fig (9) shows the electrical terminal block which consists of a plastic body, copper conductor and a cage clamp.

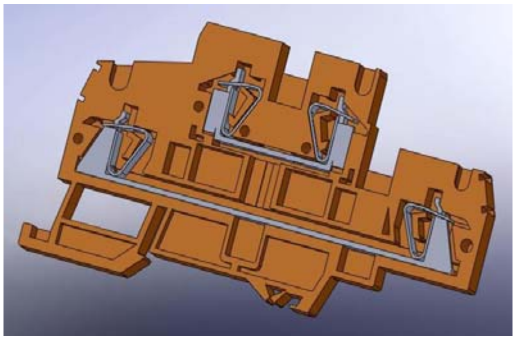

Fig (9) The Assembly view

Now to make feasible for the new design (S-clip) the current terminal block with cage clamp has been modeled. The current assembly has been modified in some specific areas to suit for the new conceptual design (S-clip), a new helical spring has been used to get necessary contact force. Fig (10) & (11)shows the details of the changes made to the current design.

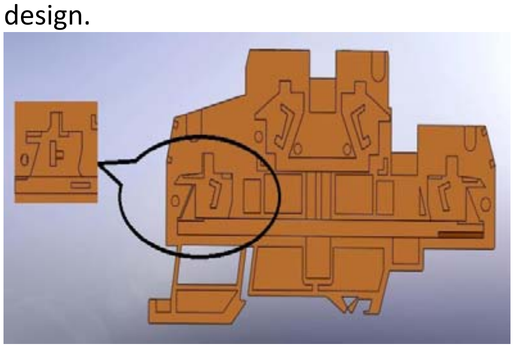

Fig (10) The Modified Area in the body

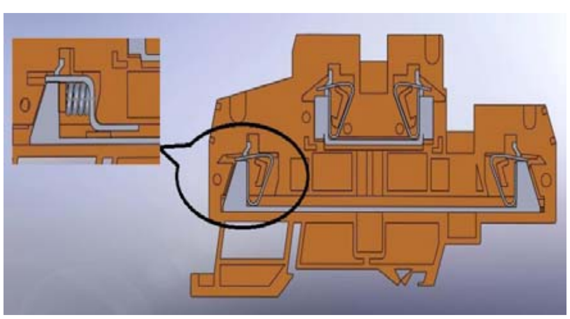

Fig (11) The Modified Clamping Unit in the Terminal Block

The following points explain the modifications made for the screw-less electrical terminal block.

- ✓ Firstly, instead of cage clamp the S-clip has been designed. The body and other parts have been subjected to design change on this basis.
- ✓ The screwdriver entry and conductor entry remains unchanged.
- ✓ The rib inside the cage clamp has been removed. And replaced with a wall towards end contact.
- ✓ This wall has a pin extended which is necessary to hold the spring.
- ✓ The inclined support for the screw driver after insertion has been increased for two degrees.
- ✓ The sharp edges are provided with a fillet to reduce stress concentration factors.
- ✓ Remaining part has been left unchanged.
- ✓ The end contact connecting two ends remains unchanged.

V. ANALYSIS

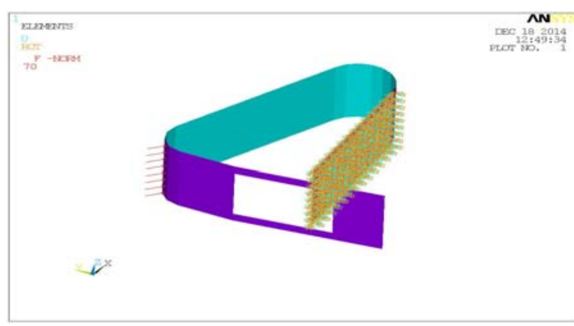

Fig (12) Cage clamp with BC's & force applied

Fig (12) shows the cage clamp, the boundary conditions are fixed at straight wall which is visible in fig by yellow lines, the material properties of stainless steel has been assigned and the force is applied on the spot where actually the screw driver pushes the clamp in the pre-processing stage. Next the problem has been solved in the solution stage.

Fig (13) & (14) shows the results obtained for the solution in the post-processing stage, where the displacement being 3.68689 mm and the von-misses stress being 6491.13MPa for the *cage clamp*.

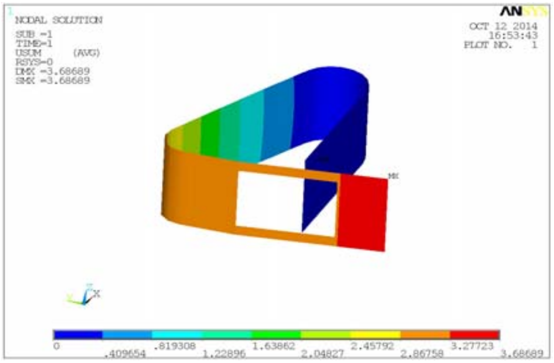

Fig (13) Displacement obtained for the applied load

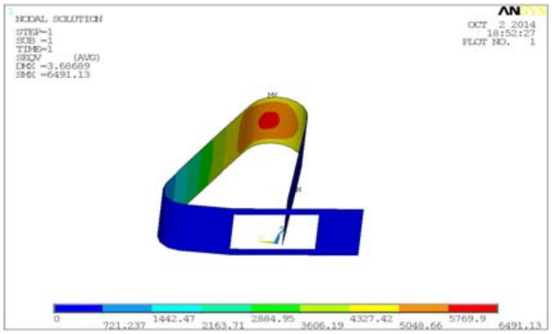

Fig (14) Von-Misses stresses in MPa

The obtained results are now compared with the new design, when the new design has been subjected to a same force of 70MPa with the same material properties, changed boundary conditions. Following fig (15) & (16) shows the results we have got.

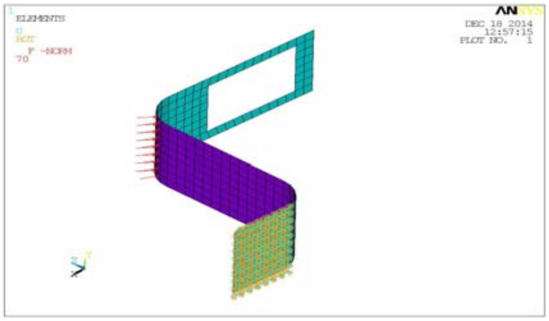

Fig (15) S-clip with BC's & force applied

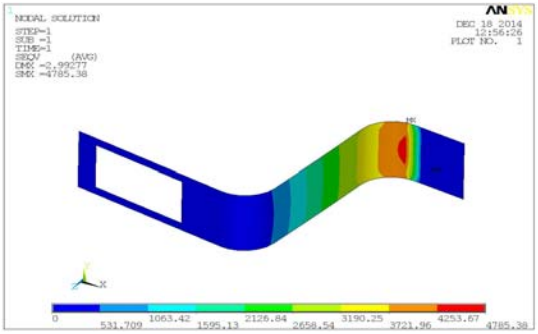

Fig (16) Von-Misses stresses in MPa

VI. CONCLUSION

The following points are the conclusion obtained by modeling, analyzing and testing this clamping unit.

- ✓ The information related to this work has been collected through various journals, existing techniques, problems etc.
- ✓ Based on the above information concept generation technique has been implemented to obtain different concepts.
- ✓ Reverse engineering technique has been used to obtain the dimensions of *cage clamp,* end contact, body. And has been successfully designed according to the requirement.
- ✓ Modeling, assembly, detailing of the *cage clamp* is carried out using solidworks.
- ✓ Different concepts have been designed to check the feasibility of those mechanisms. Based on the clamping force, drawbacks of this design. A new design technique called *S-clip* technique has been developed.
- ✓ Necessary changes have been made in the body, end contact to accommodate this *S-clip* technique.
- ✓ Analysis has been made to compare the displacements, stresses in the material of the techniques.
- ✓ For the same amount of forces the stresses are minimal in *s-clip* technique compared to *cage-clamp* technique.

REFERENCES

[1] Senthil K Chandrasegaran, Karthik Ramania, Ram D Sriram, "The evolution, challenges, and future of knowledge representation in product design systems," Computer-Aided Design 45 (2013) 204–228.

[2] Ming-Chyuan Lin, Lung-An Chen, Ming-Shi Chen, "An integrated component design approach to the development of a design information system for customer-oriented product design," Journal of Manufacturing Processes 10 (2008) 21_27.

[3] Shana Smith, Gregory Smith and Ying-Ting Shen, "Redesign for product innovation," Journal of Manufacturing Processes 10 (2008) 21_27.

[4] D. Villanueva, R.T.Haftka, B.V.Sankar, "Accounting for future redesign to balance performance and development costs," Reliability Engineering and System Safety 124(2014)56–67.

[5] Ahmed Al-Ashaab, M. Molyneaux, A. Doultsinou, "Knowledge-based environment to support product design validation," Knowledge-Based Systems 26 (2012) 48–60.

[6] Minna Parttoa, Pertti Saariluomaa, "Explaining failures in innovative thought processes in engineering design," Procedia - Social and Behavioral Sciences 41 (2012) 442 – 449.

[7] T. Meinders, I.A. Burchitz, M.H.A. Bonte, "Numerical product design: Spring-back prediction, compensation and optimization," International Journal of Machine Tools & Manufacture 48 (2008) 499–514.

[8] Jyhwen Wang, Suhas Verma, Richard Alexander, "Springback control of sheet metal air bending process," Journal of Manufacturing Processes 10 (2008) 21_27.

[9] Ling Sun**,** XiaoMing Liu, "Control Analysis of Production and Apparent Quality of Automobile Large Plastic Parts," Procedia Engineering 16 (2011) 438 – 443.

NUMERICAL SIMULATION OF PULSE LASER ABLATION

[1]Pritamkumar Dake
Mechanical engineering department
SRES College of engineering
Kopargaon, Maharastra, India
Email: [1]Pritam.dake@gmail.com

Abstract — Pulsed laser deposition is a powerful technique for thin film deposition of various materials. Pulsed laser ablation is an important process in the Pulsed laser deposition technique. This paper presents a comprehensive numerical model using finite element method considering temperature dependent material properties, plasma shielding effect and temperature dependent absorptivity and absorption coefficient to predict temperature distribution and ablation depth. The numerical simulation is performed using TiC as target material. The model takes into account the effect of delay between successive pulses during multiple laser pulses to predict temperature distribution and ablation depth.

INTRODUCTION

Pulsed Laser Deposition (PLD) is a simple and highly versatile technique to grow thin films of materials of good quality. It is a simple technique in which laser energy pulses are used to remove material from the surface of a target. High power laser pulses are directed on the target. When the target material is exposed to laser energy, sufficient heating of surface takes place leading to the melting and evaporation of the target material. This process is also called laser ablation. This ablation process produces a plasma plume, which expands rapidly away from the target surface. The ablated material collects on a substrate that is kept some distance away from the target, upon which it condenses leading to the formation of a thin film. There are a large number of variables that affect this process such as laser fluence, background gas pressure and substrate temperature. Depending upon the individual application these variables change. Much of the early research on PLD focused on individual materials and applications, rather than understanding processes occurring during material transportation from target to substrate. Even though the PLD technique is widely used, the fundamental processes occurring during the transfer of material from target to substrate are not fully understood and are subject of current research [1, 2].

The PLD technique has significant benefits compared to other film deposition techniques such as: i) relatively high deposition rates. ii) Stoichiometric transfer of material from target to substrate. iii) Extremely clean process (since an external energy source is used). iv) Housing of a number of target materials is possible by using a carousel, so multilayer films can be deposited without breaking of vacuum when changing between materials [2]. Among the research applications of PLD are: high temperature superconducting thin films, coatings for tribological applications, biomedical applications, manufacturing of micro or nano components [2, 3].

THERMAL MODELLING

Bulgakova and Bulgakov [4] developed a numerical model to evaluate the ablation rate and temperature distribution in the target under near threshold ablation conditions. They considered three mechanisms associated with the ablation process, namely, normal vaporization, normal boiling and explosive boiling (phase explosion). They considered the material removal mechanisms in PLA with infrared nanosecond pulses which are typically used for thin film deposition. Based on the measurements of ablation rate as a function of laser fluence, evidence for the transition from normal vaporization to phase explosion was obtained for a number of materials. They did not consider the non-thermal (electronic) processes induced by infrared laser radiation in the target. The time dependent temperature distribution along the target depth T (z, t) was given by the one dimensional heat flow equation as,

$$C_p\rho\left(\frac{\partial T}{\partial t}-u(t)\frac{\partial T}{\partial z}\right)=\frac{\partial}{\partial z}k\frac{\partial T}{\partial z}+[1-R]BI_s(t)\exp(-Bz) \quad (1)$$

where, C_p, ρ, k, R and B are specific heat, density, thermal conductivity, reflectivity and absorption coefficient of target material and u (t) is the velocity of surface recession. The value of u (t) is calculated considering that vaporized material flow follows the Hertz-Knudsen equation and the vapour pressure above the vaporized surface is given by the Clausius-Clapeyron equation. The laser light intensity reaching the target surface is given by

$$I_s(t)=I_0(t)\exp[-\Lambda(t)]=I_0(t)\exp\left[-\int_0^{\infty}\alpha_p(n,T)dz\right] \quad (2)$$

where, I_0 (t) is incident laser intensity, α_p (n, T) is the plasma absorption coefficient, which depends on the plasma density and temperature. Λ (t) is the total optical thickness of the plasma given by

$$\Lambda(t)=a\Delta z+bE_a$$

(3)

here, Δz is penetration depth per pulse, E_a represents density of absorbed radiation energy, a and b are time independent coefficients given by

$$a=\frac{\rho f(T_v)}{m}, \qquad b=\frac{(\gamma-1)}{k_b}\frac{\partial f}{\partial T}\bigg|_{T_v}$$

(4)

where, T_v is the temperature at which particles vaporize. The experimental evidence for the transition from normal vaporization to phase explosion during PLA of graphite, niobium and YBCO superconductor was obtained and the corresponding values of threshold fluence were determined. The thermal heating process in the irradiated targets was characterized using model calculations.

Fang *et al.* [5] described a model considering both the vaporization effect and the plasma shielding effect for the high power nanosecond PLA of multi-elemental oxide superconductors. They solved the heat conduction equations with initial and boundary conditions to describe the target temperature, taking vaporization and plasma shielding into account. The following balance equation can be written before vaporization sets in

$$C_p\rho\frac{\partial T}{\partial t}=\frac{\partial}{\partial x}k\frac{\partial T}{\partial x}+B\beta I_s(t)\exp(-Bx)$$

$$(0<t\le t_{th})$$

(5)

where C_p, ρ, k, B are as mentioned earlier, β is absorptivity of the target and τ is the width of laser pulse. After considering the vaporization and plasma shielding effects, the temperature of the target in the period from $t=t_{th}$ to $t=\tau$ is given by

$$C_p\rho\left(\frac{\partial T}{\partial t}-u(t)\frac{\partial T}{\partial x}\right)=\frac{\partial}{\partial x}k\frac{\partial T}{\partial x}+B\beta I_s(t)\exp(-\alpha_{IB}H)\exp(-Bx)$$

$$(t_{th}\le t\le\tau)$$

(6)

where, u (t) is as mentioned earlier, α_{IB} is the inverse absorption length and H is plasma length. The incident laser intensity expressed by Gauss function, given by

$$I_0(t) = I_0 \exp\left[\frac{-(t-\tau_m)^2}{\tau^2}\right]$$

(7)

where, I_0 is the maximal laser power density, τ_m is the time at which the power is maximum and τ is the time corresponding to the full width at half maximum pulse width.

FINITE ELEMENT MODELLING

To simulate laser-matter interaction, a finite element numerical model [7] has been developed using the commercial software ANSYS 11 [8]. This time dependent problem was solved sequentially, considering incremental time step of 1ns over a time period of 20 ns. During the simulation, the output of the preceding time step becomes an input to the succeeding time step. The target is represented by a mesh of finite elements. The target initial temperature is 298 K. When the temperature of an element is higher than the melting point temperature (Tm) at the end of a particular step, melting is assumed to have occurred and latent heat of melting (Lm) is taken into account for calculation in the model. The ablation is assumed to occur when the temperature of the surface elements is higher than the boiling point temperature (Tb), in this condition also, the model takes into account the phase change effect by considering the latent heat of vaporization (Lv) into calculation. Material removal in ANSYS is achieved through killing of the elements, which are deactivated by multiplying their stiffness (or conductivity or other analogous quantity) by a severe reduction factor. All the properties associated with the deactivated elements are set to zero, such as elements loads, specific heat, mass and damping.

Target representation

The target geometry used for simulation is given in Fig. 1. To minimise the computer processing time, the target is supposed to be rectangular in shape with dimension of 10µm x 3µm and only half of the target is simulated because of the axial symmetry of the problem. Moreover, only half of the simulated region is irradiated in order to account for the lateral heat losses to the non-irradiated part of the sample. The size of each element is 20nm x 20nm.

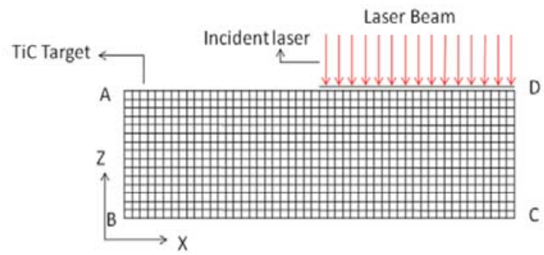

Fig..1. Geometry for laser ablation of target [7]

The element used for the analysis is PLANE 55. PLANE 55 can be used as plane element or as an axi-symmetric ring element with 2D thermal conduction capability. The element has four nodes with single degree of freedom, temperature, at each node. The element can be applied for 2D, axi-symmetric, steady state or transient thermal analysis.

Assumptions

The following assumptions are considered in the model [7]

- A 2D heat conduction equation is assumed.
- Heat source distribution is assumed to be of temporal Gaussian profile.
- Since the molten volume of the target material is very low in PLA process, Convective heat transfer effects are not considered.
- Due to very small interaction time between laser and target surface, Radiation effect has also not been taken into account.

Considerations

The following aspects are considered in the model [7]

- Thermal analysis is transient in nature.
- Temporal Gaussian profile of laser.
- Temperature dependent mechanical and thermal properties of material.

- Dynamic absorptivity and absorption coefficient.
- Absorption of laser in plasma.
- Delay between pulses.

Temperature dependent material properties

Both temperature profile and the ablation depth in PLA process vary with material properties such as thermal conductivity and specific heat, therefore it is necessary to consider the temperature dependent material properties. The model is simulated for titanium carbide (TiC) material. The material properties of TiC [21] are given in Table 1 and Table 2

Table 1. Temperature-dependent properties of TiC [6]

Temperature-dependent properties of TiC									
T (K)	298	400	800	1200	1600	2000	2400	3340	5080
K [W/(m K)]	23	24	31	36	40	43	45	8	4
Cp [J/(kg K)]	550	650	830	890	900	915	930	950	950

Table 2. Material properties of TiC [6]

Material properties of Titanium carbide						
Tm (K)	Tb (K)	ρ (kg/m^3)	Lm (J/kg)	Lv (J/kg)	a (m$^-$	b (m$^-$
3340	5080	4910	10^6	10^7	4 x 10^5	5 x 10^{-4}

BOUNDRY CONDITIONS

Equations (8) and (9) give the heat conduction equations that are solved for entire domain during the analysis within different temperature limits.

$$-k(T)\frac{\delta^2 T}{\delta z^2} = Q(z,t) \quad T<Tm$$

(8)

The above condition implies that incident laser energy onto the surface is conducted into the work piece, when target temperature is less than its melting temperature.

$$-k(T)\frac{\delta^2 T}{\delta z^2} = -L + Q(z,t)$$

T>Tm

(9)

It implies that when the target temperature exceeds its melting point, latent heat (L) comes into picture.

The boundary conditions are given by following equations

$$T(x,t)\big|_{z=0} = T_0$$

$$T(z,t)\big|_{x=0} = T_0$$

The above two conditions are under the assumption that AB and BC are far away and at the same temperature.

$$-k(T)\frac{\delta T}{\delta z}\bigg|_{x=10\mu m} = 0$$

Initial condition

Initially the temperature of the body is equal to ambient temperature

$$T(z,0) = T_0$$

RESULT AND DISCUSSION

Ablation depth per pulse

In the model, the ablation depth per pulse is calculated by killing the elements. When the temperature of the elements is higher than the boiling point temperature, these elements are assumed to be ablated. In this condition too, the model takes into account the phase change effect by considering the latent heat of vaporization in the calculation. The ablation depth is calculated knowing the numbers of elements of the mesh that reach the boiling temperature for TiC (5080 K). The ablation depths and temperature profiles calculated for a single laser pulse of 20 ns on-time for fluence levels of 4, 7, 10 and 15 J/cm^2. Fig 2 shows temperature profile and ablation depth for laser fluence of 15 J/cm^2

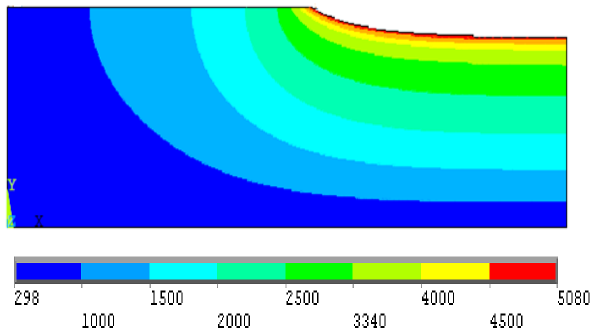

Fig. 2. Temperature distribution profile for laser fluence 15 J/cm^2

Consideration to off-time (Delay between successive pulses)

In this model the off-time is considered after single pulse on-time. The on-time has been taken as 20 ns and off-time has been considered to be 20 ns in the simulation. During the off-time, target is cooled by radiation and conduction heat losses, so the target temperature decreases. During the off-time the heat conduction takes place from high temperature to low temperature of target. The model does not consider the convective heat transfer. The thermal conduction equation is given by

$$Q_{conduction} = -K\frac{\delta T}{\delta Z}$$
(10)

The surface cooling of the target material due to radiation during the off-time has also been considered and is given by

$$Q_{radiation} = \in \sigma(Ti^4 - Tj^4)$$
(11)

It is understand that this effect is negligible for short pulse ablation process because there is very less time available between the two successive pulses for this effect to take place. We consider this effect in order to observe the overall effect of each mechanism governing the ablation process.

Temperature variation with on-time and off-time

Figure 3 shows surface temperature variation during on-time and off-time for the laser fluences in the range of 4 J/cm^2 to 15 J/cm^2 obtained after single pulse.

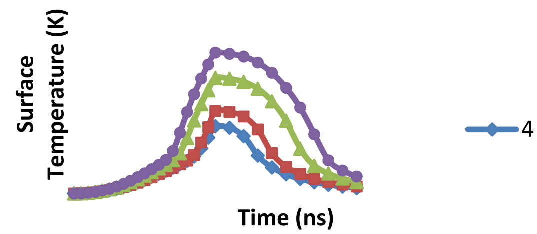

Fig. 3. Surface temperature variation during on-time and off-time after first pulse.

In the Fig. 3, first 20 ns represents on-time. During the on-time, temperature of target increases. Similarly, as the fluence level increases, the target temperature increases. At the end of 20 ns, the maximum surface temperature obtained for the laser fluence of 4, 7, 10 and 15 J/cm^2 is 5172.22 K, 6284.4 K, 8670.72 K and 10507.1 K, respectively. It is observed that, the pattern of increase in temperature with time is similar for all laser fluences (Fig. 3.7).

The next 20 ns is off-time. During the off time temperature of target decreases. The pattern of decrease in temperature is again similar for all the laser fluences. At the end of off- time, at 40 ns, the temperature of target for laser fluence of 4, 7, 10 and 15 J/cm^2 are 693.673 K, 801.867 K, 1135.55 K and 1531.91 K, respectively.

Figure 4 shows the surface temperature variation during on-time and off-time obtained after fifth pulse. Temperature at the end of fifth pulse on-time for laser flunces 4, 7, 10 and 15 J/cm^2 is increased by an ammount of 271.4 K, 305.7 K, 401.53 K, and 486.2 K respectivly compared to the temperature at the end of first pulse on-time. Temperature at the end of off- time after fifth pulse for laser fluence 4, 7, 10 and 15 J/cm^2 is 732.75 K, 839.82 K, 1267.33 K and 1671.45 K, respectivly which is greater than temperature at the end of off-time after the fourth pulse.

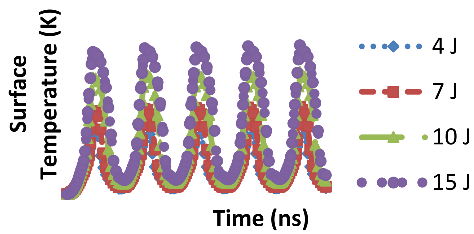

Fig. 4. Surface temperature variation during on-time and off-time after fifth pulse.

we can say that, in the case of multiple laser pulses, the temperature variation in each pulse follows the same pattern during on and off-time. In each successive pulse, temperature of the target increases at the end of on-time and off-time compared to previous pulse.

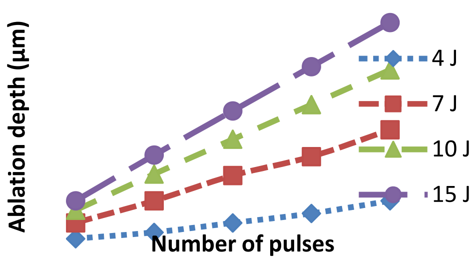

Fig. 5. Ablation depth vs Number of pulses

The ablation depths obtained after a number of pulses for laser fluences of 4, 7, 10 and 15 J/cm^2 are shown in Fig. 6. It is observed that for constant laser fluence, as the number of pulses increase, the ablation depth also increases. At the lower fluence levels, the ablation depth obtained after each successive pulse is more than the ablation depth obtained after previous pulse. Whereas, at the higher fluence levels, the ablation depth obtained during each pulse increases by the same factor. For the same pulse, as the laser fluence increases, the ablation depth also increases.

CONCLUSION

A finite element model of the laser matter interaction to predict ablation depth has been developed. The model takes into consideration temperature dependent material properties, dynamic absorptivity and absorption coefficient of the target material, plasma shielding, time dependent ablation and delay between successive pulses. The model is solved using ANSYS 11 software to determine temperature variation and ablation depth for multiple laser pulses. Major conclusions from this work are summarised below;

- The ablation depth obtained increases with an increase in laser fluence.
- In the model delay between successive pulses is considered. During the delay between pulses (off-time) the target surface is cooled by conduction and radiation.
- Temperature obtained at the end of on-time of successive pulse is greater than temperature at the end of on-time of previous pulse.
- The ablation depth obtained after second pulse is approximately double the ablation depth obtained after first pulse.
- In the multipulse laser ablation, the ablation depth increases approximately by the same factor during each successive pulse.

REFERENCES

1) Eason R., 2007, “Pulsed laser deposition of thin films”, Wiley-Interscience, pp. 3-28.
2) http://www.andor.com/learning/applic ations/Pulsed laser deposition.
3) Krebs H. U., Weisheit M., Faupe J., Suske E., Scharf T., Fuhse C., Stormer M., Sturm K., Seibt M., Kijewski H., Nelke D., Panchenko E. and Buback M., 2003, “Pulsed laser deposition (PLD) – a versatile thin film technique”, Advances in solid state physics, Springer, vol.43, pp.101-107.
4) Bulgakova N. M. and Bulgakov A. V., 2001, “Pulsed laser ablation of solids transition from normal vaporization to phase explosion”, Appl. phys. A73, pp.199-208.

5) Fang R., Zhang D., Li Z., Li L., Tan X. and Yang F., 2007, "Laser-target interaction during high power pulsed laser deposition of superconducting thin films", Phys. stat. sol. (A)204, No.12, pp.4241-4248.
6) Oliveira V. and Vilar R., 2007, "Finite element simulation of pulsed laser ablation of titanium carbide", Applied surface science, vol.253, pp.7810-7814.
7) Vasantgadkar N. A., Bhandarkar U. V., and Joshi S.S., 2010, "A finite element model to predict the ablation depth in pulsed laser ablation", Thin solid films, vol.519, pp.1421-1430
8) ANSYS v11 multiphasic software, Release 11.0SP1 UP20070830.

FEA OF LOW VELOCITY IMPACT ON WOVEN TYPE GFRP COMPOSITE LAMINATES WITH AND WITHOUT DEFECTS

[1]Venkategowda.c , [2]Dr. Rajanna.S ,[3]Dr. N G S Udupa
[1]Ph.D Scholar, Assot Professor Mechanical Engineering,
[2]Nagarjuna College of Engineering and Technology, Bangalore.
[3]Assot Professor, Mechanical Engineering, Govt Engineering college, kushalnagar.
HOD, Mechanical Engineering (PG),Nagarjuna College Of Engineering and Technology, Bangalore.
Email: [1]venkategowdancet@gmail.com, [2]rajanna.cit@gmail.com, [3]ngsudupa@gmail.com

Abstract— Numerical investigation was performed to study the behaviour of a composite plate of both undelaminated and delaminated composite plate having voids under low velocity impact. Finite element simulation has been done to calculate impact energy on the laminated composite plates. Various parametric studies performed includes boundary conditions, thickness of the laminate, lay-up sequence, mass and velocity of the impactor on the composite laminates. Woven type Glass Fibre Reinforced Polymer [GFRP] composite plates having two different thicknesses of 2 mm and 4 mm has been considered and the specimens were subjected to low-velocity impact at different velocities and the impact simulation has been performed on composite plate using explicit finite element analysis software LS-DYNA.

Index Terms— Boundary conditions, Laminate, Mass, Velocity, Impactor, lay-up sequence, LS-DYNA and Impact energy.

I. INTRODUCTION

A composite material is a macroscopic combination of two or more distinct materials, having a recognizable interface between them.

Composite laminate is a combination of fiber and resin mixed in proper form. One of the unique properties of composite laminate is that, it has high specific strength. Composites are being utilized instead of metallic materials in structures where weight is a major consideration, example aerospace structures, high speed boats and trains [1]. The use of composites has evolved commonly to incorporate a structural fiber and plastic, this is known as Fiber Reinforced Plastics (FRP). Fibers provide structure and strength to the composite, while a plastic polymers holds the fiber together, common types of fibers used in FRP composite includes: Glass fiber, Aramid fiber, Carbon fiber, Boron fiber, Basalt fiber, Natural fiber etc., in case of fiber glass, thousands of tiny glass fibers are compiled together and held rigidly in place by plastic polymer resin. Common plastic resins used in composites includes: Epoxy, polyester, vinyl ester, polyurethane and polypropylene etc.

Impact is defined as "the striking of one component against another with force instantly"; it involves the collision of two bodies: the impactor and the target. During collision, an impactor indents the target and makes indentation on the plate. The knowledge of dynamic response of structure and its damage resistance is much needed to optimize the structure requiring high safety like aircraft structural applications. The majority of impact test has been carried out on a flat plate with either simply supported or clamped boundaries. The inability to visualize the internal damage of composites makes the research community to focus on the low-velocity impact phenomena stringently. Impact phenomenon is a very complicated process in which the performance depends on many parameters like duration of the impact, kinetic energy, velocity of the impactor, properties of target and the impactor materials [2].

Defects in composite materials are produced during the manufacturing process. In that most common defects which are voids and delamination, voids can be caused by incorrect curing. Delaminations are a planar defect usually at ply boundaries and are fairly rare during the manufacture of the basic material but may be produced by contamination during lay-up or by machining. These defects will effects on mechanical performances, in general such defects cause a decrease in the static and fatigue strength of the laminate and a greater susceptibility to water penetration and environmental conditions[12].

The experimental analysis is often used to study loading, deformation, and damage of composite plates. However, this method is expensive, time consuming and requires multiple standardized test prototypes, equipment and strongly regulated test settings [3]. A significant advantage of finite element analysis is that an advanced preliminary study can be carried out by using a virtual prototype in a virtual environment which can substantially cut costs, reduce the development time and substantially optimize the overall development process. The main objective of this paper is to investigate the impact behaviour of the composite plate under three different velocities by using finite element analysis software LS-DYNA.

II. NUMERICAL PROCEDURE

A woven fabric composite plate having stacking sequence of 0/90/0/90/0/90/0/90/0/90 with bi-directional configuration, having a ply thickness of 0.2mm is considered for impact analysis using explicit finite element analysis software LS-DYNA [5]. In Figure 1, Let x be the variable that describes the position of the projectile. The impact energy was calculated by using the formula.

$$E = 1/2 m_i v_i^2$$

Where m_i is mass of the impactor, thickness of the composite plate is taken as h and v_i is the impact velocity measured before impact event.

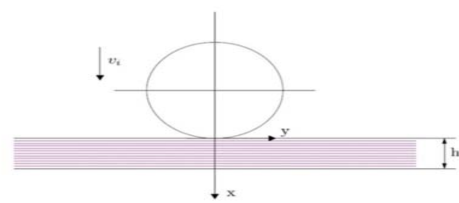

Fig.1:Impactor and target configuration setup

The number of layers on both 2 mm and 4 mm thickness composite plate is shown in table 1. The values were adopted from experimental data as per the work presented in reference [1]. The failure mechanism of the GFRP composite laminates under low velocity impact depends on several factors such as strength of the composite plate, velocity and mass of the impactor, boundary conditions which are applied to the model.

TABLE 1: DIMENSIONS AND NUMBER OF LAYERS

Material	Dimension of the component in mm	No. of Laminates	
		2mm thickness	4mm thickness
GFRP	150×50	10	20

III.FINITE ELEMENT SIMULATION

Finite element simulation was done to analyse the impact energy dissipated on both undelaminated and delaminated composite plates.

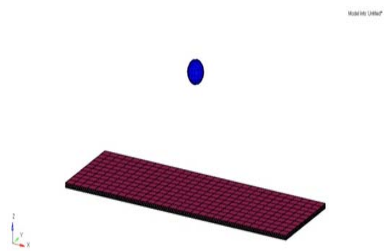

Fig.2: HYPERMESH Model

Glass fiber reinforced polymer composite laminates were modelled using software known as HYPERMESH. All the four sides of the specimen were fixed in x, y and z directions and orthotropic material was selected for modelling the material, the laminates were impacted at the centre of the composite plate by a steel impactor having a spherical tip of 10 mm in diameter and a weight of 15.69 N has been used. The material properties of the impactor and composite plate are as shown in table 2 and 3 respectively.

Table 2: Impactor properties

Young's modulus	Poisson's ratio	Density
210 GPa	0.3	7800 Kg/mm^3

The impactor is allowed to move only in z direction and treated as a rigid body. An automatic surface to surface contact condition is assigned between the composite plate and impactor to accommodate impact initiation and progress. Time step is one of the most important parameter, which normally causes divergence in non-linear finite element analysis. By choosing an adequate time step value simulation has been done [7]. The finite element model of the impactor and composite laminates are shown in Figure 2 and was prepared by using pre-processing finite element analysis software known as HYPERMESH. Here LS-DYNA program manager was used as a processor to solve the problem and LS-PrePost was used as post processing software, where we can see the displacements, stress results and deflection animations [8].

Table 3: Composite plate properties

Young's Modulus in GPA	E_{11}	20.8
	E_{22}	20.8
	E_{33}	8.7
Shear Modulus in GPa	G_{12}	3.92
	G_{23}	4.2
	G_{31}	4.2
Poisson's Ratio	ν_{12}	0.173
	ν_{23}	0.28
	ν_{13}	0.28
Density in Kg/m^3	ρ	1750

Delamination and voids have been created on both 2 mm and 4 mm thickness composite plate having same geometry as that of undelaminated composite plate and impact analysis has been conducted.

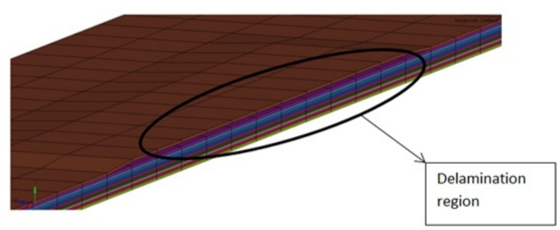

Fig.3: Half sectional view of delaminated composite plate

Delamination of 0.2 mm gap between the top layer and its next layer of the composite plate has been created at the center to an area of 50 mm × 20 mm. Figure 3 shows half sectional view of delaminated composite plate and it has been created using HYPERMESH software.

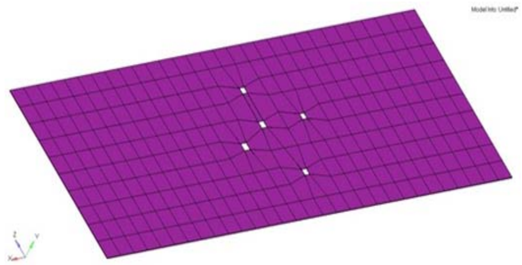

Fig.4: Voids on the composite layer

Figure 4 shows the voids on the composite plate and it has been created at the center of the composite plate on the second layer from the top, where the impactor is going to impact. It was created by using HYPERMESH software, by removing the elements on the composite plate.

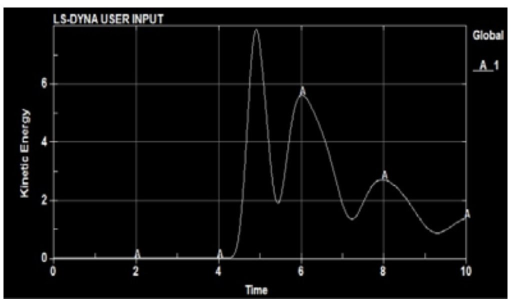

Fig.5: Impact energy result for undelaminated composite plate

Finite element simulation was done by using explicit finite element analysis software LS-DYNA, impact energy results in case of undelaminated composite plate is shown in figure 5. In that graph the point where maximum deviation occurs, that value has been taken as impact energy.

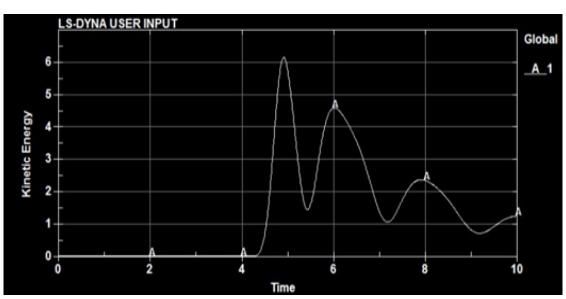

Fig.6: Impact energy result for delaminated composite plate

Figure 6 shows impact energy results for delaminated composite plate. Here impact energy results have been varied because of defects like delamination and voids which is introduced on that plate. These defects will reduce the strength of the composite plate so impact energy results were reduced.

IV. RESULTS AND DISCUSSION

Numerical analysis has been done for both undelaminated and delaminated composite plate having two different thickness of 2 mm and 4 mm were subjected to low velocity impacts at three different velocities (3.132, 4.429 and 5.425 m/s).

Table 4: Impact energy results for undelaminated composite plate

Mass of the impactor in N	Velocity in m/s	Impact Energy in Joules	
		2 mm	4 mm
15.69	3.132	7.9	8.9
15.69	4.429	14.01	16.13
15.69	5.425	21.07	24.94

Impact energy results for undelaminated composite plate are shown in Table 4. For both 2 mm and 4 mm thickness composite plate, impact energy results were increased with increasing the velocity of the impactor [13].

Table 5: Impact energy results for delaminated composite plate with voids

Mass of the impactor in N	Velocity in m/s	Impact Energy in Joules	
		2 mm	4 mm
15.69	3.132	6.23	7.01
15.69	4.429	12.9	14.1
15.69	5.425	20.05	20.90

Impact energy results for delaminated composite plate with voids have been recorded in table 5. Impact analysis has been conducted for the same velocity as that of undelaminated composite plate but here impact energy results are reduced. Reduction of impact energy results due to defects which are introduced on the composite plate.

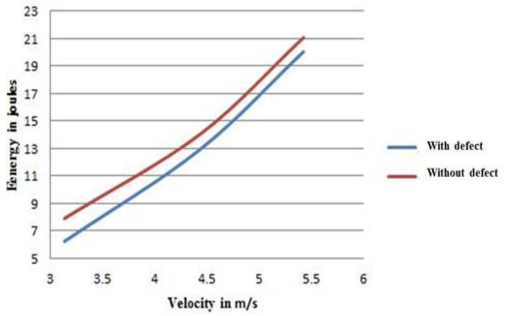

Fig.7: Results comparison for 2mm thickness plate

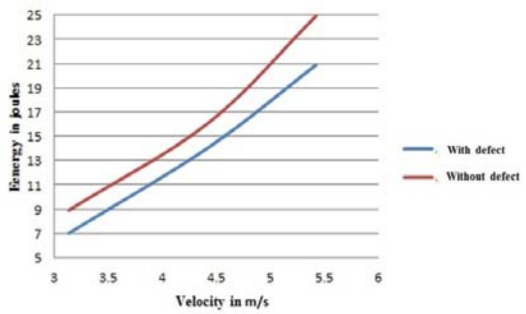

Fig.8: Results comparison for 4mm thickness plate

Comparison of 2mm and 4mm thickness undelaminated composite plate with delaminated composite plate is shown in figure 7 and 8 respectively. In that blue line indicates composite plate with defects and red indicates without defect. Here we can see the variation of the results on defected and un-defected composite plates.

V. CONCLUSION

NUMERICAL ANALYSIS WAS PERFORMED TO STUDY THE BEHAVIOUR OF GLASS FIBRE REINFORCED POLYMER COMPOSITE PLATE UNDER LOW VELOCITY IMPACT USING EXPLICIT FINITE ELEMENT ANALYSIS SOFTWARE LS-DYNA. UNDELAMINATED COMPOSITE PLATE OF BOTH 2 MM AND 4 MM THICKNESS PLATE WAS COMPARED AGAINST DELAMINATED COMPOSITE PLATE WITH VOIDS. IN THAT IMPACT ENERGY RESULTS WERE VARIED BECAUSE OF DEFECTS LIKE DELAMINATION AND VOIDS WHICH ARE INTRODUCED IN COMPOSITE PLATE. THESE DEFECTS WILL REDUCE THE STRENGTH OF THE COMPOSITE PLATE SO IMPACT ENERGY RESULTS WERE REDUCED. IT IS ALSO CONCLUDED THAT IMPACT ENERGY RESULTS ARE MAINLY DEPENDS ON SOME OF THE PARAMETERS LIKE, BOUNDARY CONDITIONS, VELOCITY OF THE IMPACTOR AND PROPERTIES OF TARGET AND THE IMPACTOR MATERIALS.

REFERENCES

[1] ErcanSevkat, Benjamin Liaw, FeridunDelale , Basavaraju B. Raju, “Drop-weight impact of plain-woven hybrid glass–graphite/toughenedepoxy composites”, ElsevierInternational Journal on composites 2009, PP 1090–1110.

[2] B. Kranthi Kumar, LakshmanaKishore.T, “Low Velocity Impact Analysis of Laminated FRP Composites”, International Journal of Engineering Science and Technology (IJEST), 2012, Vol. 4, PP 115-125.

[3] M.A. Hassan, S. Naderi, A.R. Bushroa, “Low-velocity impact damage of woven fabric composites: Finite element simulation and experimental verification”, International Journal on Materials and Design 53 (2014), PP 706–718.

[4] Shreyas.P.S, N. Rajesh Mathivanan, JullyaNaik.L, Harshavardan.S.Shetty, “Prediction of fatigue life for woven GFRP Composite laminates with impact damage”, Department of Mechanical Engg., Nagarjuna College of Engg. & Technology, Bangalore, 2014.

[5] ASM Handbook for Fatigue and Fracture Vol. 19 material and information society.

[6]N. Rajesh Mathivanan, J. Jerald, “Experimental investigation of low-velocity impact characteristics of woven glass fiber epoxy matrix composite laminates of EP3 grade”, Materials and Design 31 (2010), PP 4553–4560.

[7] HyperWorks 12.0user's manual.

[8] LS-DYNA®keyword user's manual, Volume I and II, August 2012, Version 971 R6.1.0, Livermore Software Technology Corporation (LSTC).

[9] J. Lo´pez-Puente, R. Zaera, C. Navarro, "An analytical modelfor high velocity impacts on thin CFRPs woven laminated plates", International Journal of Solids and Structures 44 (2007), PP 2837–2851.

[10] K. Azouaoui, Z. Azari, G. Pluvinage, "Evaluation of impactfatigue damage in glass/epoxy composite laminate", International Journal of Fatigue (2010), PP 443–452.

[11] Gin Boay Chai, PeriyasamyManikandan, "Low velocity impact response of fibre-metal laminates review", International Journal on Composite Structures 107 (2014), PP 363–386.

[12] Nisha A S and Saraswathy B, "Dynamic Analysis of Delaminated Sandwich Composites", International Journal of Modern Engineering Research (IJMER), Vol.3 (2013), PP-172-177.

ANALYSIS OF ANGEL PLY LAMINATED COMPOSITE AND VALIDATION

[1]Manjunatha S C, [2]C Venkate Gowda, [3]Dr. Prashanth Banakar
[1]PG Student, Nagarjuna College of Engineering and Technology, Bangalore
[2]Associate Professor, Nagarjuna College of Engineering and Technology, Bangalore
[3]Professor, Sambram Institute of Technology Bangalore.
Email: [1]Manjunath4reddy90@gmail.com, [2]venkategowdancet@gmail.com,
[3]prashanthbanakar77@gmail.com

Abstract— In this paper, the specimens are fabricated using carbon fiber, E-Glass fiber, epoxy resin and Hardener HY104 with the help of hand lay-up technique. The effect of fiber orientation and thickness of laminates has been investigated and experimentation was performed to determine property data for material specification. Specimens are cut as per ASTM standards. Furthermore, failure mode and strength characteristics of composites specimens with different fiber orientations will be studied. For all geometrics of specimen, the ultimate strength, breaking stress and elongation will be recorded. Analysis was tested by using ANSYS software.

This research indicates that the mechanical properties are mainly dependent on fiber orientation of laminates and thickness of laminated polymer composites.

Index Terms— Composite materials, Carbon fiber, E-Glass fiber, Epoxy resin, Hardener HY104, Fiber orientation and thickness of laminates.

I. INTRODUCTION

Composite materials are manufactured from two or more materials to take advantage of desirable characteristics of the components. A composite material, in mechanics sense, is a structure with the ingredients as element transferring forces to adjacent members. The advance in design and application of composites has accelerated in the past decade especially in the aeronautics, defence, and space industries. Commercial applications are also increasing as products needing challenging materials properties are increasing in demand.

The majority of composite materials use two constituents: a binder or matrix and reinforcement. The reinforcement is stronger and stiffer, forming a sort of backbone, while the matrix keeps the reinforcement in a set place. The binder also protects the reinforcement, which may be brittle or breakable, as in the case of the long glass fibers used in conjunction with plastics to make fibre glass.

Generally, composite materials have excellent compressibility combined with good tensile strength, making them versatile in a wide range of situations. In this project the specimens are fabricated using carbon and glass fibre cloth with epoxy resin and hardener HY 951 with the help of vacuum hand-layup technique. Tensile specimens as per ASTM Standards will be prepared with different hole diameters. Furthermore, failure mode and strength characteristics of composite specimens consisting of central holes of different diameters will be studied. For all geometries of the specimens, the ultimate strength, breaking stress and elongation will be recorded.

A. Carbon Reinforced Fiber

Carbon fiber (carbon fibre), CRF is a material consisting of extremely thin fibers about 0.005–0.010 mm in diameter and composed mostly of carbon atoms. The carbon atoms are bonded together in microscopic crystals that are more or less aligned parallel to the long axis of the fiber. Carbon fiber-reinforced plastic (CFRP or CRP), is a very strong, light, and expensive composite material or fiber-reinforced polymer. Similar to fiberglass (glass reinforced polymer), the composite material is commonly referred to by the name of its reinforcing fibers (carbon fiber). The polymer is most often epoxy, but other polymers, such as polyester, vinyl ester or nylon. The crystal alignment makes the fiber very strong for its size. Several thousand carbon fibers are twisted together to form a yarn, which may be used by itself or woven into a fabric.

Carbon fiber has many different weave patterns and can be combined with a plastic resin and wound or moulded to form composite materials such as carbon fiber reinforced plastic (also referenced as carbon fiber) to provide a high strength-to-weight ratio material. The density of carbon fiber is also considerably lower than the density of steel, making it ideal for applications requiring low weight. The properties of carbon fiber such as high tensile strength, low weight, and low thermal expansion make it very popular in aerospace, civil engineering, military, and motorsports, along with other competition sports.

However, it is relatively expensive when compared to similar materials such as fiberglass or plastic. Carbon fiber is very strong when stretched or bent, but weak when compressed or exposed to high shock (eg. a carbon fiber bar is extremely difficult to bend, but will crack easily if hit with a hammer).It has many applications in aerospace and automotive fields, as well as in sailboats, and notably in modern bicycles and motorcycles, where its high strength-to-weight ratio is of importance. Improved manufacturing techniques are reducing the costs and time to manufacture, making it increasingly common in small consumer goods as well, such as laptops, tripods, fishing rods, paintball equipment, archery equipment, racquet frames, stringed instrument bodies, classical guitar strings, drum shells, golf clubs, and pool/billiards/snooker cues.

B. Glass-Reinforced Plastic

Glass-reinforced plastic or GRP is a composite material made of a plastic matrix reinforced by fine fibers made of glass. It is also known as GFK (for Glass Fiber komposite), or simply by the name of the reinforcing fibers themselves: fiberglass.GRP is a lightweight, strong material with very many uses, including boats, automobiles, water tanks, roofing, pipes and cladding.The plastic matrix may be a thermosetting plastic (most often polyester or vinyl ester), epoxy or thermoplastic.The manufacturing process for GRP fiber glass uses large furnaces to gradually melt the sand/chemical mix to liquid form, and then extrude it through bundles of very small orifices (typically 17-25 micrometers in diameter for E-Glass, 9 micrometers for S-glass).

These filaments are then sized with a chemical solution. The individual filaments are now bundled together in large numbers to provide a roving. The diameter of the filaments, as well as the number of filaments in the roving determines its weight. This is typically expressed in yield-yards per pound (how many yards of fiber in one pound of material, thus a smaller number means a heavier roving, example of standard yields are 225yield, 450yield, 675yield) or in tex-grams per km (how many grams 1 km of roving weighs, this is inverted from yield, thus a smaller number means a lighter roving, examples of standard tex are 750tex, 1100tex, 2200tex).An individual structural glass fiber is both stiff and strong in tension and compression—that is, along its axis. Although it might be assumed that the fiber is weak in compression, it is actually only the long aspect ratio of the fiber which makes it seem so; i.e., because a typical fiber is long and narrow, it buckles easily.

On the other hand, the glass fiber is unstiff and unstrong in shear—that is, across its axis. Therefore if a collection of fibers can be arranged permanently in a preferred direction within a material, and if the fibers can be prevented from buckling in compression, then that material will become preferentially strong in that direction.Furthermore, by laying multiple layers of fiber on top of one another, with each layer oriented in various preferred directions, the stiffness and strength properties of the overall material can be controlled in an efficient manner.

In the case of glass-reinforced plastic, it is the plastic matrix which permanently constrains the structural glass fibers to directions chosen by the designer. With chopped strand mat, this directionality is essentially an entire two dimensional plane; with woven fabrics or unidirectional layers, directionality of stiffness and strength can be more precisely controlled within the plane.A glass-reinforced plastic component is typically of a thin "shell" construction, sometimes filled on the inside with structural foam, as in the case of surfboards. The component may be of nearly arbitrary shape, limited only by the complexity and tolerances of the mold used for manufacturing the shell.

These rovings are then either used directly in a composite application such as pultrusion, filament wounding (pipe), gun roving (automated gun chops the glass into small lengths and drops it into a jet of resin, projected onto the surface of a mold), or used in an intermediary step, to manufacture fabrics such as chopped strand mat (CSM) (made of randomly oriented small cut lengths of fiber all bonded together), woven fabrics, knit fabrics or uni-directional fabrics.

Process: Resin is mixed with a catalyst (e.g. butanox LA) or hardener if working with epoxy, otherwise it will not cure (harden) for days/ weeks. Next, the mould is wetted out with the mixture. The sheets of fiber glass are placed over the mould and rolled down into the mould using steel rollers. The material must be securely attached to the mould; air must not be trapped in between the fiber glass and the mould. Additional resin is applied and possibly additional sheets of fiber glass.

II Methodology For Specimen Preparation

- Fabricate hybrid laminated composite specimens with E-Glass and Carbon fiber combination as per ASTM standards.
- Evaluate the mechanical properties (tension, flexural and compression) of the above composite.
- Determine the mechanical parameters for the specimens under different orientation of the fiber.
- Assess the post static test results and evaluate the extent of damage of hybrid composite specimens with the carbon fiber specimens.
- Discuss the results obtained from the experimentation and analysis by using ANSYS and finally to conclude the performance of composites about its mechanical characteristics for various applications.

A. Preparation of Specimen

- Carbon fiber & Glass fiber material consisting of extremely thin fibers about 0.005–0.010 mm in diameter and composed mostly of carbon atoms.
- The process by which most carbon fiber-reinforced polymer is made varies, depending on the piece being created, the finish (outside gloss) required, and how many of this particular piece are going to be produced.

- Glass-reinforced plastic or GRP is a composite material made of a plastic matrix reinforced by fine fibers made of glass
- The bi-woven clothes are available in the standard form of 0.37mm thickness.
- Bi-Woven cloths are cut to the required size & shape.
- These cloths are stacked layer by layer of about 5 layers to attain the thickness of 2mm as per the ASTM Standard Specimen.
- Bonding agent (epoxy resin and hardener) is applied to create bonding between 5 layers of sheet, in the ratio of 2:1.

The process of polymerization is called "curing", and can be controlled through temperature and choice of resin and hardener compounds; the process can take minutes to hours. Some formulations benefit from heating during the cure period, whereas others simply require time, and ambient temperatures. Process of vacuuming will be done to remove air traps exist between the layers. Vacuuming & Room curing to be done about 3hrs. After curing process the materials cut to the required size & Shape as per ASTM Standard.

Fig-1 Specimens as per ASTM Standards

B. Evaluate the mechanical properties

Tensile test: Consider the typical tensile specimen shown in Fig 2. It has enlarged ends or shoulders for gripping. The important part of the specimen is the gage section.

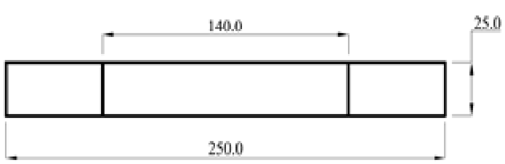

Fig-2 Tensile Specimen Dimensions as per ASTM D-3039

The cross-sectional area of the gage section is reduced relative to that of the remainder of the Specimen so that deformation and failure will be localized in this region. The gauge length is the region over which measurements are made and is centered within the reduced section. The distances between the ends of the gage section and the shoulders should be great enough so that the larger ends do not constrain deformation within the gage section, and the gage length should be great relative to its diameter. Otherwise, the stress state will be more complex than simple tension.

The most important concern in the selection of a gripping method is to ensure that the specimen can be held at the maximum load without slippage or failure in the grip section Bending should be minimized.

Flexural Testing: Flexural strength is the ability of the material to withstand bending forces applied Perpendicular to its longitudinal axis. Sometime it is referred as cross breaking strength where maximum stress developed when a bar-shaped test piece, acting as a simple beam, is subjected to a bending force perpendicular to the bar. There are two methods that cover the determination of flexural properties of material: three-point loading system and four point loading system. As described in ASTM D7264, three-point loading system applied on a supported beam was utilized. Flexural test is important for designer as well as manufacturer in the form of a beam.

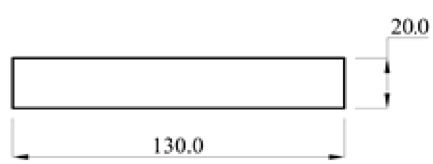

Fig-3 Specimen Dimensions as per ASTM D-3039

Compression test: Compression testing is also a fundamental materials science test in which a sample is subjected to uniaxial compressive load. The results from the test are commonly used to select a material for an application, for quality control and to predict how a material will react under other types of forces.

The most common testing machine used for compression test is a Universal Testing Machine (UTM).

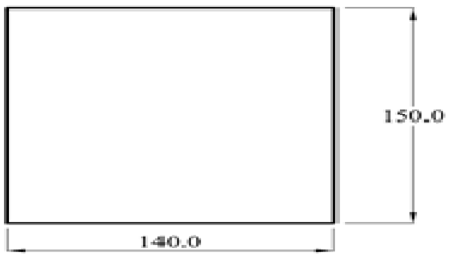

Fig-4 Specimen Dimensions as per ASTM D-3039

III EXPERIMENTAL RESULTS AND FEA RESULTS

A. TENSILE TEST RESULTS

TABLE-1 TENSILE TEST EXPERIMENTAL RESULTS AND FEA RESULTS

Sample Thickness (mm)	Fibre orientation	Experimental Stress (Mpa)	FEA Stress (Mpa)	Experimental displacement (mm)	FEA displacement (mm)
2	90º	219.2	227.03	7.9	9.48
2	60º	53.6	55.51	9.45	11.32
2	45º	43.6	45.14	13.4	13.31

B. FLEXURAL TEST RESULTS

TABLE-2 FLEXURAL TEST EXPERIMENTAL RESULTS AND FEA RESULTS

Sample Thickness (mm)	Fibre orientation	Experimental Stress (Mpa)	FEA Stress (Mpa)	Experimental displacement (mm)	FEA displacement (mm)
2	90º	288.82	325.32	10.7	10.896
2	60º	157.59	158.27	18.2	15.94
2	45º	118.15	123.28	24.1	19.13

C. COMPRESSION TEST *RESULTS*

TABLE-3 COMPRESSION TEST EXPERIMENTAL RESULTS AND FEA RESULTS

Sample Thickness (mm)	Fibre orientation	Experimental Stress (Mpa)	FEA Stress (Mpa)	Experimental displacement (mm)	FEA displacement (mm)
2	90º	2.83	2.344	34	35.78
2	60º	0.50	1.0049	43.8	47.94
2	45º	0.357	0.2989	80.4	79.9

IV CONCLUSION

When composite materials are designed, the reinforcements are always oriented in the load direction. However if the load direction is variable and not parallel to the fibres it becomes more important to investigate the laminate mechanical behaviour. To investigate the effect of fibre orientation, $\pm 45^0$, $\pm 60\ ^0$and $\pm 90^0$ were selected under this study. Specimens with different fibre orientation Were Prepared under the same condition as discussed earlier. The experimental investigations used for the analysis of tensile, flexural and compression behaviour of carbon and E-glass fibre reinforced polymer laminates leads to following conclusion.

The experimental results shows that the tensile, flexural and compression strength is affected by the fibre orientation significantly summarized below;

- The tensile, flexural and compression strength is superior in case of 45^0 orientation.
- More load is required for fracture of laminates in case of 90^0 orientation.
- More elongation is observed in case of 45^0orientation.
- The elongation is minimal in case of 90^0orientation.
- Specimen sustain greater load in 90^0orientation as compared to other orientations.

- Young's modulus is more in case of 90^0orientation.
- Young's modulus of specimens is increases with decreases in thickness of the specimen.

REFERENCES

[1] Prashanth Banakar, H.K. Shivananda and H.B. Niranjan "Influence of Fibre Orientation and Thickness on Tensile Properties of Laminated Polymer Composites" Int. J. Pure Appl. Sci. Technol., 9(1) (2012), pp. 61-68.

[2] Keshavamurthy Y C , Dr. Nanjundaradhya N V , Dr. Ramesh S Sharma, Dr. R S Kulkarni "Investigation of Tensile Properties of Fibre Reinforced Angle Ply laminated composites" ISSN 2250-2459, Volume 2, Issue 4 April 2012.

[3] GuruRaja M. N, A. N. HariRao. "Hybrid Effects on Tensile Properties of Carbon/Glass Angle Ply Composites". Advances in Materials. Vol. 2, No. 3, 2013, pp. 36-41.

[4]. K.Vasantha Kumar1, Dr.P.Ram Reddy , Dr.D.V.Ravi Shankar " Effect of Angle Ply Orientation On Tensile Properties Of Bi Directional Woven Fabric Glass Epoxy Composite Laminate" International Journal of Computational Engineering Research Vol, 03 , Issue 2010.

[5] K. Kishor Kumar, P. Ramesh Babu and K. Raja Narender Reddy "Evaluation of Flexural and Tensile Properties of Short Kenaf Fibre Reinforced Green Composites". International Journal of Advanced Mechanical Engineering. ISSN 2250-3234 Volume 4, Number 4 (2014), pp. 371-380.

[6] Swanson SR. Introduction to design and analysis with advanced composite materials. Englewood Cliffs, NJ: Prentice Hall, 1997

[7] Yong X. Gan Effect of interface on mechanical properties of advanced composite materials J of Mol.sci.2009:5115-5134

[8] Marissen R. Flight simulation behaviour of aramid reinforced aluminium laminates. Eng Fract Mech 1984:19:261-77.

[9] Tensile properties and fatigue characteristics of hybrid composites with non-woven carbon tissue Jl. of fatigue 2007:397-405.

[10] ASM Data hand book: 195

[11] G. Kretsis, a review of the Tensile, Compressive, Flexural and shear properties of hybrid fibre reinforced plastics, Composites, Vol 18:1987

[12] J. Harding and L.M Welsh, A tensile testing technique for fibre-reinforced composites at impact rates of strain, J Master Sci 18:1983.

[13] J.Cho, Mechanical enhancement of carbon fibre/epoxy composites by graphite nanoplatelet reinforcement, S. Direct 2007:685-688

AN SVD-DWT-BASED ULTRASOUND IMAGE WATERMARKING SCHEME.

[1]Mr.V.T.Kamble, [2](Smt.) Dr.R.S.Patil
[1]P.G.Student E&TC Dept D.Y.Patil College Of Engg.&Tech.Kolhapur,India,
[2]Professor E&TC Dept.D.Y.Patil College Of Engg.&Tech.Kolhapur,
Email: [1]vinay_kamble83@yahoo.com, [2]prekha46@yahoo.com

Abstract-In last decade use of advanced electronics and digital equipment's in health care services are increased. In fact in most of the hospitals physicians' diagnosis their patients by relying on the provided electronic and digital data (such as Ultrasound, CT, MRI).This results in generation of large number of electronic digital data (i.e. medical images) continuously act various health care centers and hospitals around the world.

This paper focus on the study of ultrasound images watermarking methods for protecting and authenticating medical data. It consist of watermarking technique on Region of Non-Interest(RONI) of the medical image preserving Region Of Interest(ROI).The medical images can be transferred securely by embedding watermark in RONI allowing verification of the legimate changes at receiver end without affecting ROI.Watermarks conveying patients personal and examination data. In purposed system ROI indicated by physician for correct diagnosis purpose.Orignal image is decomposed into 2-level discrete wavelet transform (DWT) along with singular Value Decomposition (SVD) for watermarks. The experimental result shows the satisfactory performance of the system to authenticate the medical images preserving ROI.

Keywords-Ultrasound image, Wavelet transform, Singular Value Decomposition, Watermark, Region Of Interest (ROI), Region Of Non-Interest (RONI).

I.INTRODUCTION

Now a day's most physicians rely on Computed Tomography (CT), Magnetic Resonance Imaging (MRI),Ultrasonic and the traditional X-Ray images to diagnose their patient accurately, therefore the exchange of medical images between hospitals has become common in order to share the information for diagnostic, on the other hand, this process needs a considerable amount of memory and bandwidth. One way to overcome this problem is to have the complete medical information of a patient available in one entity rather than over several information systems. This exchange of medical images shows three advantages[1]1:Confidentiality means that only entitled persons have access to the information since some patients do not like to expose their information to the public.2:Reliability which includes: Integrity means the information has not been modified by unauthorized users and Authentication, which is a proof that the information belongs to the correct patient and is issued from the right source.3:Availability which means the access to the information for authorized persons. Different kinds of watermarks meet the parameters of imperceptibility, robustness and capacity to different degrees, these parameters usually conflict with each other. Therefore, an application-dependent trade-off between them is necessary. Medical images are usually comprised of region of interest (ROI) and region of non interest (RONI)[2].The portions of an image which include the significant information for diagnosis are called ROI and therefore should be remained intact during the watermarking (embedding) process. The rest of image is called RONI and hence the watermark may be included in such region. It has been shown that employing digital wavelet transform (DWT) in watermarking of image information shows priority over other data hiding algorithms, especially when DWT is combined with other techniques to improve the robustness [3, 4]. Singular value decomposition (SVD) is one of the most convenient tools of linear algebra with several applications in image compression, watermarking and other areas of signal processing. Most SVD- based watermarking schemes modify the singular values of host image by the singular values of watermark.

This paper presents a watermarking algorithm for medical images in which DWT and SVD are exploited to produce a robust watermarking method. Section2 provides a brief review on Watermarking techniques and SVD concept. In section 3, proposed embedding and extracting algorithms are presented. This is followed by experimental results in section 4 and discussion on results and concluding remarks are presented in the last section.

II Watermarking methods

A:- Domain selection

Watermarking method can be distinctly divided into two basic categories [5]: 1: Spatial domain and 2: Frequency domain. Spatial domain schemes embed watermarks in pixels of an image directly. The least significant bit (LSB) scheme is the most common method to embed watermarks in an image [6]. The main advantage of this approach is its simplicity while it presents a low robustness which is its main disadvantage.2: Frequency domain watermarking, for example, using the DFT (Discrete Fourier Transform), DCT
(Discrete Cosine Transform) and DWT (Discrete Wavelet Transform) which are difficult to detect the watermarks. Discrete Wavelet Transform has excellent spatial localization, frequency spread, and multiresolution characteristics similar to the theoretical models of the human visual system (HVS). The HVS splits an image into several frequency channels, which each channel processes the corresponding signals independently, the dyadic wavelet decomposition performs the similar image resolution by dividing the image into different bands with different frequency. 2-D DWT process the image by 2-D filters in each dimension. The filters divide the input image into four non-overlapping multi resolution sub-bands LL, LH,HL and HH. HH, HL and LH contain the diagonal, horizontal and vertical details of the image, respectively while the LL sub-band contains the coarse details of the image. To obtain the next coarser scale of wavelet coefficients, the LL sub-band is further decomposed until L-level wavelet coefficients are produced. Fig. 1illuminates 2-level decomposition.

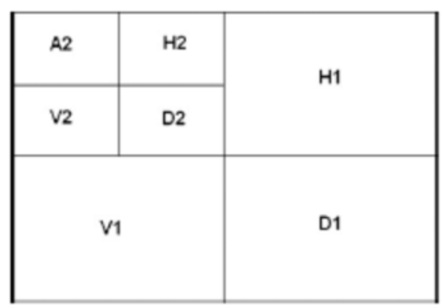

Fig. 1.2- level DWT composition

The approximation sub-band is not selected because manipulation of the low frequency sub-band will impose sever degradations on the reconstructed image as the most of the energy is concentrated in this sub band. The sub-bands which have higher energy are more robust against common attacks. Therefore, in the second level of wavelet transform, the 2 sub-bands with higher energy are selected as the place to embed the watermark bits. These sub-bands are divided to non-overlapping blocks of 8*8 pixels and then the SVD transform is used to these blocks.

B:-Embedding of watermark in Region Of Non-Interest (RONI)

Singular value decomposition (SVD) is one of the most useful tools of linear algebra with several applications in image compression, watermarking and other areas of signal processing [7]. SVD packs maximum signal energy into a few coefficients as possible. Every real matrix A can be decomposed into a product of 3 matrices.

$$A = U\Sigma V^T \quad (1)$$

where U and V are orthogonal matrices.

It is important to note that the singular value decomposition of digital images presents the following properties [8]

1) The singular value of image is stable which means that it does not change much after applying common attacks and so watermarked image quality is not reduced and its changes are not noticeable with human eyes.

2) Each singular value specifies the luminance of an image layer while the corresponding pair of singular vectors specifies the geometry of the image layer. An important property of SVD –base watermarking is that the largest of the modified singular values against signal processing attacks change very little.

3) This Singular value decomposition method is used to embed the watermark in Region of non-interest of the image.

Our approach focuses on embedding watermark in RONI region of medical image by preserving ROI. This approach helps in isolating ROI region i.e. not to distort the critical area of medical image, which will be referred by physician for the diagnosis. The system diagram for this approach is shown in Figure 2:- The system process carried away in three stages:

1. Watermark embedding process
2. Watermark extraction process
3. Watermark authentication process

In first phase of system separating the ROI from the original medical image provides RONI region for embedding watermark. This step isolates ROI from embedding process. In this phase multiple watermarks are embedded into the RONI area of medical image. Embedding multiple watermarks ensure high security of medical image as it carries high payload and it will be more complex to break the system. Here fragile watermarking system is used to get the benefit of identifying whether a medical image is tampered or not? After the completion of embedding process the separated ROI is combined with the produced watermarked medical image. The resultant watermarked medical image is then sent to the receiver.

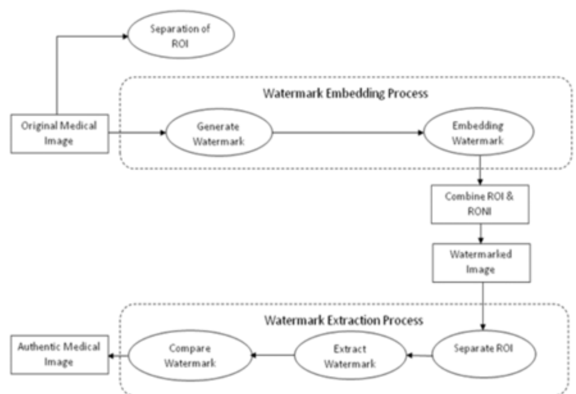

Figure:-2 Medical Image Watermarking Approach Preserving ROI

In watermark extraction phase, first step is separating the ROI from the watermarked medical image. The remaining watermark extraction process is exact reverse of embedding process, where the embedded watermark will be extracted from the watermarked medical image. The watermark authentication is achieved by comparing the extracted watermark with the original watermark. This process helps in identifying if any tampering manipulation to the watermarked medical image over the public network.

III Method

In recent days the wavelet analysis got a good recognition in research and development area due to its characteristic of providing time and frequency information simultaneously. As per research the retina of the eye splits an image in to several frequency channels i.e. approximately one octave. In multi resolution decomposition the image is divided into bands of equal bandwidth on a logarithmic scale. There is lot of similarity between the signal processing of the human visual system

(HVS) and scaling decomposition of the wavelet transform which can be achieved by watermark embedding to the masking property or quantization method [9].

A:-Description

The watermarks used in this approach:

1. Doctor's identication code
2. Indexed watermark
3. Patient's reference identication code
4. Patient's diagnosis information
5. Patient's treatment information

The listed watermarks used in this proposed watermarking scheme helps in addressing different issues and concerns in healthcare management system, Such as confidentiality of medical data, recovering original image without any distortion, data integrity, authentication and efficient data management. Confidentiality of medical data is achieved by embedding watermark using Integer to Integer Discrete Wavelet Transform (IDWT), which confirms the imperceptibility property. This property ensures the embedded watermark will be invisible to the normal human eye and the watermark can be extracted by the

one who knows the embedding and extraction algorithm applied in this system. By applying Inverse IDWT at the receiver end original image can be recovered without any distortion. Also the distortion to the ROI has already been avoided by separating the ROI before embedding the watermark in to the medical image. Medical data integrity is achieved by using fragile watermarking system, so any manipulation on medical image data leads in distortion of embedded watermark. For the authentication purpose the included watermarks such as doctor's identification code, patient's identification code will ensures the entitled users can accessor modify the medical data. To provide efficient data management in this system the indexed watermark is embedded which helps in retrieving the image for the future reference if needed using database query. The watermarks are inserted in different decomposition levels and sub-bands depending on their type. They can be independently embedded and retrieved without any intervention among them. By integrating this idea into different medical acquisition systems like Ultrasound, CT and MRI etc. This system can be applied in different applications such as e-diagnosis or medical image sharing

through picture archiving and communication.

IV Algorithm

In this algorithm the multiple watermarks embedding technique is used. Where depending on the quantization of selected coefficients the multiple watermarks embedding procedure is used. This prevents any modification to the watermark bits by granting integer changes in spatial domain of medical image. This can be achieved by applying 2-levl haar wavelet transform to decompose the host medical image. Moreover it gives the output as coefficients, which are in the form of dyadic rational numbers. These coefficients denominators are in powers of 2. The multiple of 2^l (l is decomposition level) number adding or subtracting

to the produced coefficient value, assures that the inverse DWT provide integer pixel values. Wavelet transform generally provides the coefficients which are real numbers. By applying the quantization function it assigns the binary number to every coefficient. This quantization function is defined as

$$Q(f) = 0, \quad if \left\lfloor \left(\frac{f-s}{\Delta} \right) \right\rfloor \; is\ even$$

$$Q(f) = 1, \quad if \left\lfloor \left(\frac{f-s}{\Delta} \right) \right\rfloor \; is\ odd$$

(2)

Where s is a user defined offset for increased security, f is frequency coefficient produced by haar wavelet transform and , the quantization parameter, is a positive real number. Moreover Δ is defined as $\Delta = 2^l$. The quantization procedure is shown in Figure 3:-

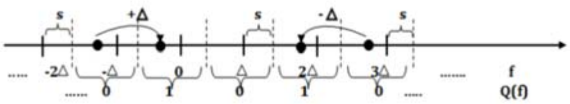

Figure 3:- Quantization Procedure

As explain earlier, addition or subtraction of a multiple of 2^lvalue to the haar wavelet coefficient results in integer pixel values, after applying inverse DWT. During the embedding process the algorithm add or subtract an appropriate constant to the haar coefficient chosen for watermark casting.

A) The algorithm for embedding multiple watermarks is explained below:

Step 1: Indicate the ROI region from the host medical data by physician for proper diagnosis purpose. Which results in image of RONI region.
Step 2: Save the removed ROI from medical image.
Step 3: The multiple watermarks to be embed into a original image is generated by reading the patient's information file from text document.
Step 4: Apply the 2-level Haarwavelet transform to original medical image to obtained a gross image approximation at the lowest resolution level and a sequence of detail images corresponding to the horizontal, vertical, and diagonal details at each of the two decomposition levels.
Step 5: On each decomposition level the watermark bitwise is embedded into the key determined coefficient f, which is obtained by applying wavelet transform according to the following condition:

1. If $Q(f) = w_i$, the coefficient is not modified
2. Otherwise, the coefficient is modified so that $Q(f) = w_i$, using the following equation:

$f = f + \Delta$; if $f \leq 0$
(3)
$f = f - \Delta$; if $f \geq 0$
(4)

Step 6: The pre watermarked image is produced by performing the corresponding two level inverse wavelet transform.

Step 7: The resultant watermarked image is obtained.

B) The watermark extraction process

It is similar to that of embedding one except that at the receiving end extractor should have the knowledge of location of the embedded watermark. This can achieve by the key based embedding and detection. With this type of method access to the watermark by unauthorized users is prevented. The algorithm for extraction process to recover the host medical image is explained below.

Step1: The resultant watermarked image is taken.

Step2:Apply the 2level haar wavelet transform to the image which is created from step 1, which results in a image approximation at level two and sequence of images corresponding to the horizontal, vertical, and diagonal details at each of the two decomposition levels.

Step3: Identify the location of watermark by key based detection.

Step4: Extract the watermarks by applying quantization function defined in equation (2) which recovers the original coefficient. Convert the extracted binary watermark to text watermark.

Step5: The pre output image is obtained by applying inverse 2-level haar wavelet transform.

Step 6: Finally get the original host ultrasound image.

V RESULTS

For testing purpose 50 ultrasound images of size 256x256 pixels; all images were collected by the same physician using the same equipment and ultrasound system settings, in order to avoid deviation in image statistics.

A) Quantitative measures:-

1) Peak signal-to-noise ratio (PSNR):-

The quantitative assessment of the quality of the watermarked images was conducted using both the peak signal-to-noise ratio (PSNR) and the weighted PSNR metrics. The PSNR is not well correlated with perceptual quality, however, it provides an efficient measure of image distortion in terms of numerical values, which convey important information in medical applications, e.g., in the case of diagnosis support systems.

The PSNR is measured in decibels and is defined as follows:-

$$\mathrm{PSNR}(I, \hat{I}) = 10 \log_{10} \left[\frac{\left(\max\limits_{\forall (m,n)} I(m,n) \right)^2}{\frac{1}{N_I} \sum_{\forall (m,n)} (\hat{I}(m,n) - I(m,n))^2} \right] \quad (5)$$

where*I* and *I* are the original and watermarked images, respectively, *N*I is the number of pixels in the image, and max∀ (*m, n*) *I* (*m, n*) is the maximum gray value of the original image. The denominator of the PSNR is the average sample mean squared error.

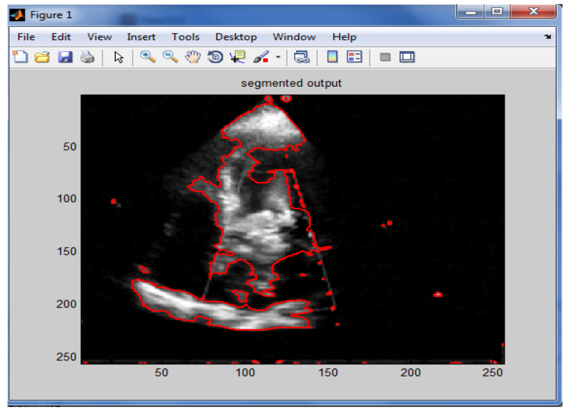

Figure 4:-Segmented output

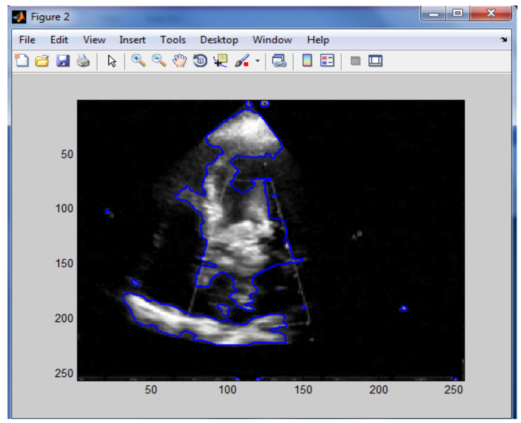

Figure 5:- Segmented output (500 Iteration)

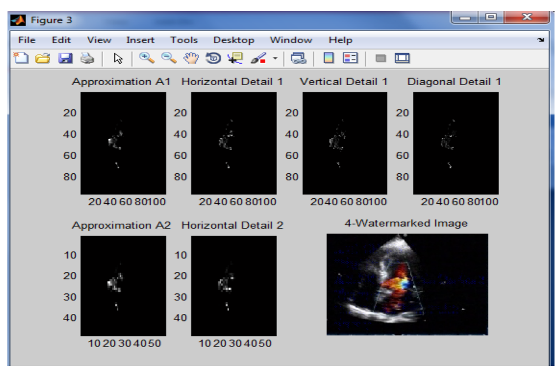

Figure 6:- Tree Structure of 2-level DWT.

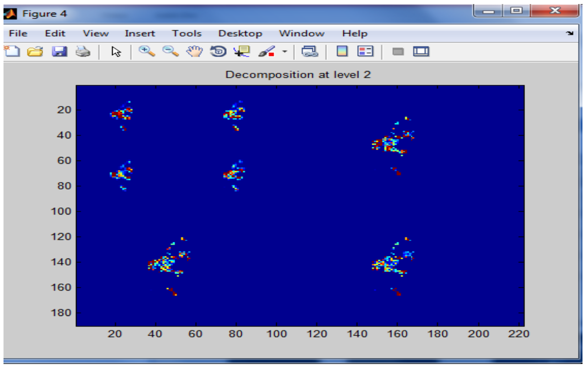

Figure 7:- Two-level Haar DWT Of an ultrasound image.

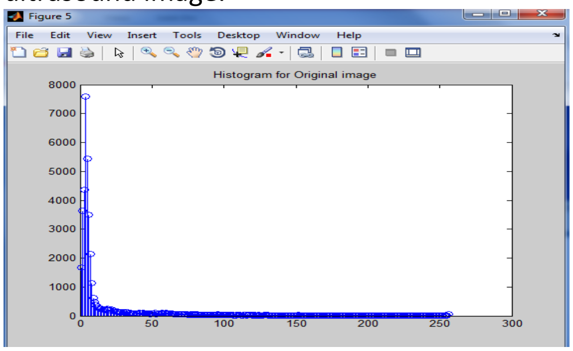

Figure 8:-Histogram For Original image

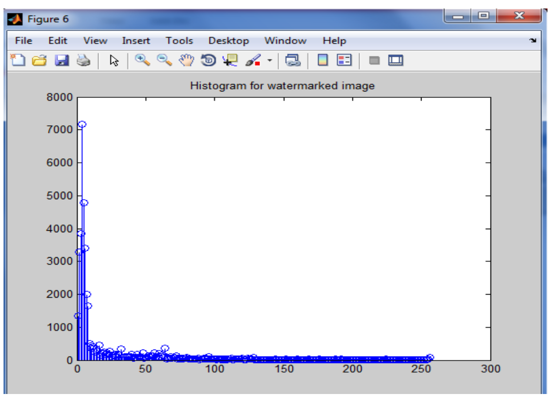

Figure 9:-Histogram Of Watermarked image

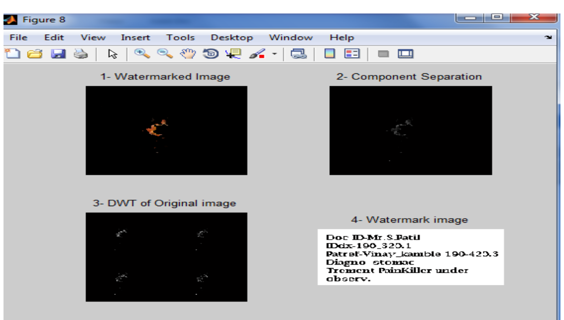

Figure 10:-Retrieved Watermark image

Table I

The corresponding results of PSNR, Image Quality Index and MAE for Ultrasound images.

Sr No.	Ultrasound Images	PSNR(dB)	Image Quality Index	MAE
1	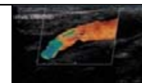	43.8720	0.9647	3.1490
2		43.5463	0.9554	2.9007
3		45.9946	0.9424	2.7712
4		44.1299	0.9618	2.7085
5	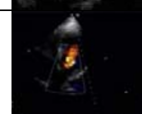	44.9521	0.9248	2.9240
6		46.6103	0.9514	2.4716
7		46.7202	0.9557	2.4218
8		46.3375	0.9171	2.5739
9	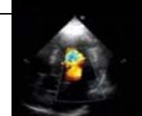	46.2318	0.9625	2.6233
10		46.3672	0.9513	2.5330

VI. Conclusion

There exist various medical image watermarking algorithms which provide the confidentiality of medical data, recovering original image without any distortion, data integrity, authentication and efficient data management. Also the different segmentation algorithms are in place, which vary for the types of medical images such as MRI, CT scan, X-ray and Ultrasounds etc.

Here the proposed system used an algorithm to embed watermark image in Region of Non-interest (RONI) without affecting Region Of Interest (ROI).The ROI region which is considered as a critical data and used as a reference by the physician for the treatment will be safe. Singular value decomposition has become one of the most popular watermarking algorithms. In this Paper we uses the combination of digital wavelet transform and SVD has been presented. Experiments proved that the algorithm can embed the watermarks into images and the detector can retrieve the original image.

References

[1] G. Coatrieux, L. Lecornu, B. Sankur,Ch. Roux, A Review of Image Watermarking Applications inHealthcare,Proceedings of the 28th IEEE 2006 , pp.4691-4694.

[2] K. A. Navas, S. ArchanaThampy, and M. Sasikumar, EPR Hiding in Medical Images for Telemedicine, International Journal of Biological and Life Sciences 3:1 2007, pp. 44-47.

[3] H. Lu and W. Xia, “A Robust Binary Image Watermarking Based on Wavelet Domain and Krawtchouk Moments,” International Conference on Research Challenges in Computer Science, 2009.

[4] M. Amini, H. R. Sadreazami, K. Yaghmaie, “A New Scheme for Dual Watermarking Using DWT-PCATechnique,” IMAGAPP - International Conference on Imaging Theory and Applications, pp: 43-46, May 2010.

[5] H.Lee, H.Jung Kim, K. Kwon and, J.Lee, "ROI Medical Image Watermarking Using DWT and Bit-plane", Asia Pacific Conference IEEE on Communications, Perth, WA, pp. 512-515, 2005.

[6] Yeh, C.H., Kuo, C.J, "Digital watermarking through quasim arrays”, Signal Processing Sys, IEEE Workshop, pp.
456-461999.

(7) H. Zhihua, “Binary Image Watermarking Algorithm Based on SVD,” International Conference on Intelligent Human-Machine Systems and Cybernetics, pp: 400-403, 2009.

(8)R. Liu and T. Tan, “An SVD-Based Watermarking Scheme for Protecting Rightful Ownership,” IEEE Transactions.

(9)F. Hartung, B. Girod, "Watermarking of Uncompressed and Compressed Video", Signal Processing, Vol. 66, No. 3, pp. 283-301, May 1998.

(10)Giakoumaki, Sotiris Pavlopoulos, and Dimitris Koutsouris, (Oct. 2006) “Multiple Image Watermarking Applied to Health Information Management”, IEEE Trans. on information technology in biomedicine, vol.10, no.4.

(11)Wakatani, (Jan 2002) “Digital Watermarking for ROI Medical Images by Using Compressed Signature Image", Proceedings of the 35th International Conference on System Sciences.

(12)Yusuk Lim, Changsheng Xu, and David Dagan Feng, “Web based Image Authentication Using Invisible Fragile Watermark”, Pan-Sydney Area Workshop on Visual Information Processing (VIP2001), Sydney, Australia.

(13)Nisar Ahmed Memon, S.A.M. Gilani, and Shams Qayoom, (2009) “Multiple Watermarking of Medical Images for Content Authentication and Recovery”, IEEE.

(14)H.Lee, H.Jung Kim, K. Kwon and, J.Lee, "ROI Medical Image Watermarking Using DWT and Bit-plane", Asia-Pacific Conference IEEE on Communications, Perth, WA, pp. 512-515, 2005.